Title
Interface Magnetism in Multiferroics

Author
He, Qing

Publication Date
2011

Interface Magnetism in Multiferroics

by

Qing He

A dissertation submitted in partial satisfaction of the
requirements for the degree of
Doctor of Philosophy
in
Physics
in the
Graduate Division
of the
University of California, Berkeley

Committee in charge:

Professor Ramamoorthy Ramesh, Chair
Professor Frances Hellman
Professor Feng Wang
Professor Junqiao Wu

Spring 2011

Interface Magnetism in Multiferroics

Abstract

Interface Magnetism in Multiferroics

by

Qing He

Doctor of Philosophy in Physics

University of California, Berkeley

Professor Ramamoorthy Ramesh, Chair

This dissertation focuses on the thorough characterization of nanoscale interface regions - so-called domain walls - between structurally, electronically and magnetically homogeneous areas or domains in $BiFeO_3$ thin films. These domain walls exhibit intriguing properties not found in the domains themselves and were determined using a combination of nanoscale characterization techniques such as transmission electron microscopy, atomic force microscopy, piezo-response force microscopy, scanning tunneling microscopy, X-ray absorption spectroscopy and photoemission electron microscopy. Enhanced net magnetic moments are observed at certain type of domain walls (109°) in $BiFeO_3$, although the adjacent domain areas are antiferromagnetically ordered with only a very small net magnetic moment. The same type of the domain walls is found to be conducting at a semiconductor level while the domains are insulating and exhibit robust ferroelectricity. 2-D arrays of these domain walls exhibit intriguing magnetotransport behavior: when both current path and magnetic field are oriented parallel to the domain walls, about 60% of negative magnetoresistance is observed at low temperature ($\sim$10 K), which can be well modeled with electron variable hopping. Moreover, in highly strained $BiFeO_3$ thin films electrically controllable magnetic moments are found localized in a highly distorted rhombohedral-like phase confined between the adjacent tetragonal-like phase. Those magnetic moments can be turned on and off by applying an electric field.

For my family and all my friends,
who make the world beautiful around me

Contents

List of Figures

List of Tables

Acknowledgments

The past six years of my life have been spent in the company of some truly amazing people in this wonderful place, and I am honored to recognize their contributions to this thesis here. I will always be indebted to my advisor, R. Ramesh, for introducing me to a fascinating field and your never-ending passion for science that always motivated and encouraged me. I would like to give my special thanks to Ying-Hao Chu – without your encouragement, patience and help, first as a most supportive post-doc, and then as a collaborator and supervisor, I wouldn't have made it this far. I have also been privileged to work with so many delightful people both in Ramesh's group and in collaborations. I am grateful to Elke Arenholz, Andreas Scholl, Micky Holcomb, Tony Young, Andrew Doran, Christoph Quitmann, Arantxa Fraile-Rodriquez, and many other beamline scientists, for your help, support and encourage, which let me find my interests and enthusiasm in soft X-ray based research and lead my career towards this amazing field. I thank Nicola Spaldin, Lane Martin, Pu Yu, Weidong Luo, Jan Seidel, Seul-Yeung Yang, Haimei Zheng, Padraic Shafer, Chan-Ho Yang, Morgan Trassin, Florin Zavaliche, Maria P. Cruz, and Martin Gajek, professionally and personally, for your priceless advices. I thank Nina Balke, John Heron, Jinxing Zhang, Tianliang Qu, Florian Straub, Stefan Abel, and Tommy Conry for sharing your experiences and the same memories during my graduate school.

I, and hundreds of graduate students before me, owe much to Anne Takizawa and Donna Sakima. Especially as an international student, I have got so much help and care from you, Anne, from the most minimal form filling confusions to large decision making for my career.

I would also extend my deepest thanks to my qualifying exam committee Joel Moore, Feng Wang, and Oscar Dubon and to Frances Hellman, Feng Wang, and Junqiao Wu for serving on my dissertation committee.

I must also thank my family: my mother, Minlun Zhao; my father, Xuanming He; my aunt, Minhui Zhao; and my cousin, Kaida Yang, for a lifetime of encouragement and support.

Chapter 1

Introduction

1.1 Introduction to Complex Oxides

Complex oxides show a wide variety of interesting functionalities and intriguing properties while maintaining a simple structure, which attracts great attentions in both basic research and applications. Examples of widely known and studied functionalities in complex oxides include superconductivity in $YBa_2Cu_3O_{7-\delta}$ [14], ferroelectricity in $PbTiO_3$, colossal magnetoresistance (CMR) in (La,Sr)MnO_3 [15] [16], and multiferroic in $BiFeO_3$ [7] [4]. Other categories of complex oxides with useful functionalities include diluted magnetic semiconductors (e.g., (Zn,Mg)As), high ε_r insulators (e.g., $LaAlO_3$ and $SrTiO_3$), conducting oxides (e.g., Sr_2RuO_4), thermoelectrics (e.g., doped $SrTiO_3$), ferromagnets (e.g., $SrRuO_3$), optoelectronics (e.g., ZnO), and transparent conducting oxides.

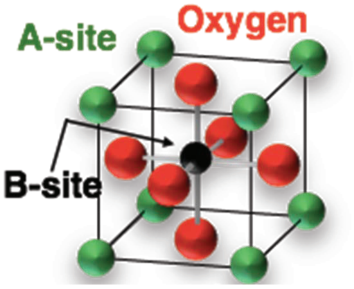

Figure 1.1: Crystal structure of a perovskite unit cell.

There is also a wide range of oxide crystal structures, as in perovskites, pyrochlores, spinels, rock salt, and compounds with layered structures. Perovskite structure (Figure 1.1) is a common ternary oxide structure, which has chemical formula ABO_3 (e.g., $BiFeO_3$, $SrRuO_3$, $SrTiO_3$), and consists B-cation octahedrally coordinated by six oxygen anions in the body center of the unit cell and A-cation coordinated by twelve oxygen anions at the corners. It is noteworthy that in the (001) direction, the perovskite structure can be considered as alternating stacks of AO and BO_2 sheets.

1.2 Order parameters

The order parameters reflecting the ordering of charge, spin, orbital, and lattice degree of freedom play important roles in controlling the properties of the materials. Materials with ferroic order parameters, such as ferromagnetism, ferroelectricity, ferroelasticity, ferrotoroidicity, show spontaneous order and are most interesting in both research as well as for applications. Ferromagnetism and ferroelectricity will be introduced in this section.

1.2.1 Magnetism

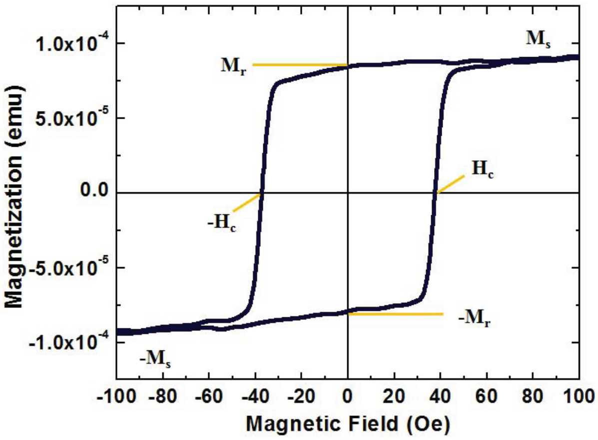

Figure 1.2: Ferromagnetic hysteresis loop of $Co_{0.90}Fe_{0.10}$

The most commonly used and understood magnetic order is ferromagnetism, which can be seen everywhere in our daily lives (e.g., as small or large permanent magnets on refrigerators or in power generators, as switchable electronic ferromagnets in computer memories, etc.). A ferromagnet is a material exhibiting a spontaneous magnetization that can be controlled by an external magnetic field. The signature of ferromagnetic materials is the existence of an M–H or B–H (magnetization vs. magnetic field) loop, an example of which is shown in Figure 1.2. This hysteresis curve shows that some magnetization will remain even if no external magnetic field is applied. This magnetization is called the “remanent magnetization”, B_r. The field required to reduce the magnetization of the sample to zero is called the coercive field H_c, and can be used to define the magnetic hardness of the ferromagnetic material.

The saturation magnetization B_s is the magnetization where all the magnetic moments are aligned parallel to the external field and the system is in a mono-domain state. Many different methods may be used to characterize the ferromagnetic order of a material, for example neutron scattering, X-ray magnetic circular dichroism, or using a vibrating sample magnetometer or superconducting quantum interference device.

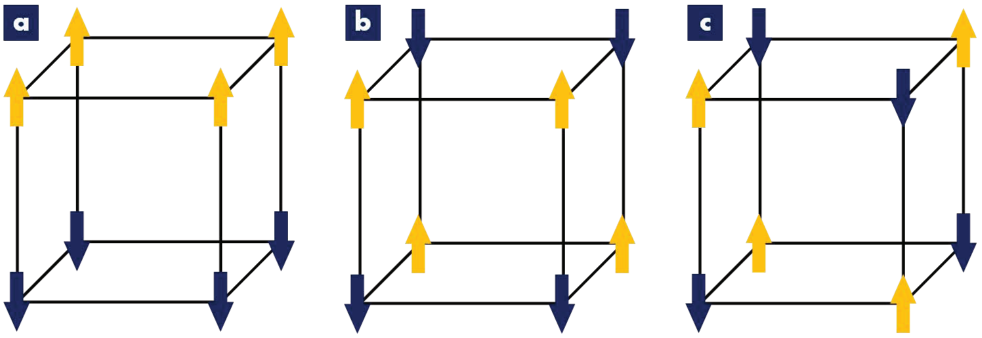

Figure 1.3: Three types of antiferromagentic orders. (a), (b), (c) Schematics of A, C, G-type antiferromagnetism. [1]

In contrast toferromagnets, antiferromagnetically ordered materials show no net magnetic moment, i.e. the neighboring spins are aligned collinearly but point in opposite directions. Antiferromagnetic order occurs when the exchange interaction, $J < 0$, while $J > 0$ indicates a ferromagnetic interaction. Of the many types of antiferromagnetic orders, the most common are named A, C, and G-type antiferromagnetism (Figure 1.3(a), (b), (c), respectively) [1]. In A-type antiferromagnetic materials, the spins in the (001) plane are ferromagnetically coupled, while the spins between adjacent (001) planes are antiferromagnetically aligned. The ferromagnetic plane is the (110) plane in C-type antiferromagnetic materials and the (111) plane in G-type antiferromagnetic materials.

$BiFeO_3$ is an example of a G-type antiferromagnet, although its neighboring Fe spins are not exactly antiparallel to each other. Strong spin-orbital coupling results in Dzyaloshinskii-Moriya interaction in this system, which allows the Fe spins to cant by a small angle ($\sim 1°$) and resulting in a small ferromagnetic moment ($\sim 0.05\mu_B$) along the canting direction. The canted magnetic moment forms a spin cycloidal structure with a long modulation period of $\lambda \approx 620$ Å in the bulk. In $BiFeO_3$ thin films, this spin cycloidal structure is not sustainable and a magnetization of 6-8 emu/cc has been observed.

1.2.2 Ferroelectricity

The prefix "ferro", used in naming the ferroic orders, originates from "iron" or "related to iron" and is taken from " ferromagnetism" indicating a property similar to

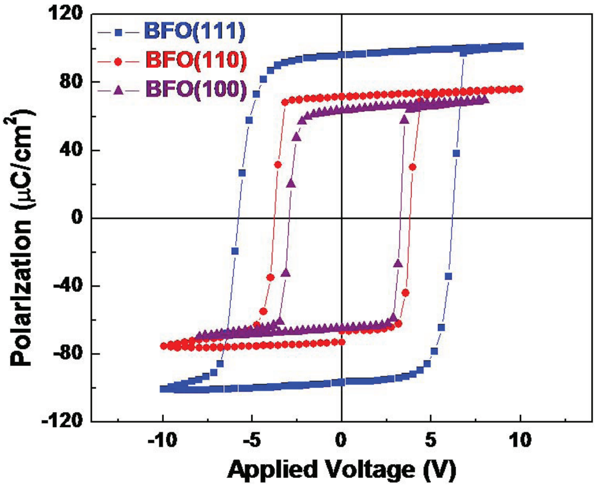

Figure 1.4: Ferroelectric hysteresis loops of $BiFeO_3$ taken at different crystallographic directions.

spontaneous magnetic order. However, in most ferroelectric materials, the ferroelectricity is not attributable to iron. In these materials, the spontaneous order parameter is electric polarization, which can be controlled by the application of an external electric field. Examples of polarization hysteresis loops of a ferroelectric, $BiFeO_3$ are shown in Figure 1.4. The loops are taken in three different crystallographic directions. Ferroelectricity can be studied macroscopically with ferroelectric measurement systems based on the Sawyer Tower circuit or microscopically by piezo-response force microscopy probing the detailed structure of ferroelectric domains.

1.3 Introduction to Multiferroics and Magnetoelectrics

Materials possessing more than one ferroic order parameter are named multiferroics. According to the original definition, a single phase multiferroic is a material that simultaneously possesses two or more of the “ferroic” order parameters - ferromagnetism, ferroelectricity, ferroelasticity and ferrotorroidicity. The simultaneous emergence of several order parameters and their coupling provides the means to influence one order parameter through the control of another (Figure 1.5a).

Among all coupled order parameters, the link between magnetic order and electric polarization has attracted the most interest worldwide to date. Magnetoelectric coupling typically refers to the linear magnetoelectric effect or the control of magnetization by an electrical field or electric polarization by a magnetic field. Magnetoelectricity is an independent phenomenon that can arise in any material with both magnetization and electric polarization. However, not all magnetoelectrics are mul-

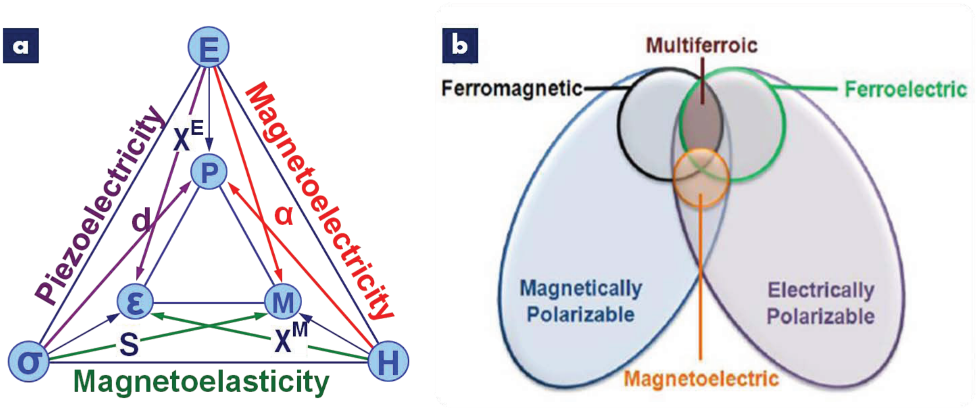

Figure 1.5: Multiferroic and magnetoelectric materials. (a) Schematic illustrating different types of coupling present in materials. These materials are known as magnetoelectric materials exhibit a coupling between magnetic and electric polarization. [2] [3] [4] [5] (b) An illustration representing the relationship between multiferroic and magnetoelectric materials indicating the requirements to produce both multiferroicity and magnetoelectricity in a single material. [6] [7] [8] [9]

tiferroics and not all multiferroics are magnetoelectrics. The overlap between these two classes requires a ferroic order parameter (ferroelectricity and ferromagnetism) as shown in Figure 1.5b. According to the original definition, a magnetoelectric multiferroic [17] must be simultaneously both ferromagnetic and ferroelectric. However, when the definition of multiferroics was expanded to include anti-ferroic properties, magnetoelectric multiferroics were considered to include materials with antiferromagnetism or antiferroelectricity.

As illustrated in Figure 1.3b, magnetoelectric multiferroics constitute only a very small fraction of magnetically and electrically polarizable materials. Its scarcity is easily understood. First, there are only 13 point groups that are compatible with multiferroic behavior. Moreover, ideal ferroelectrics are insulators and typically arise from ions that have a formal d^0 electronic state. In contrast, ferromagnets typically need conduction electrons and require a partially filled d shell. This incompatibility of electronic structure is the reason for the scarcity of ferromagnetic ferroelectric multiferroics.

A mathematical description of magnetoelectric coupling can be obtained by the expansion of the free energy of a material, i.e.

$$\begin{aligned} F(\vec{E},\vec{H}) = {} & F_0 - P_i^S E_i - M_i^S H_i - \frac{1}{2}\varepsilon_0\varepsilon_{ij}E_iE_j - \frac{1}{2}\mu_0\mu_{ij}H_iH_j \\ & - \frac{1}{2}\beta_{ijk}E_iH_jH_k - \frac{1}{2}\gamma_{ijk}H_iE_jE_k - \cdots \end{aligned} \tag{1.1}$$

with $\vec{E}$ and $\vec{H}$ denoting the electric and magnetic field, respectively. Differentiation leads to the order parameters: electric polarization

$$\begin{aligned} P_i =&(\vec{E},\vec{H}) = -\frac{\partial F}{\partial E_i} \\ =&P_i^S + \varepsilon_0\varepsilon_{ij}E_j + \alpha_{ij}H_j + \frac{1}{2}\beta_{ijk}H_jH_k + \gamma_{ijk}H_iE_j + \cdots \end{aligned} \tag{1.2}$$

and magnetization

$$\begin{aligned} M_i =&(\vec{E},\vec{H}) = -\frac{\partial F}{\partial H_i} \\ =&M_i^S + \mu_0\mu_{ij}H_j + \alpha_{ij}E_j + \frac{1}{2}\beta_{ijk}E_iH_j + \gamma_{ijk}E_jE_k + \cdots \end{aligned} \tag{1.3}$$

where ε and μ are the electric and magnetic susceptibilities respectively and α represents the induction of polarization by a magnetic field or magnetization by electric field and represents the linear magnetoelectric effect. Although higher order magnetoelectric effects, represented by β and γ, are possible, they are often much smaller in magnitude than the lower order terms. Furthermore, it can be shown that the magnetoelectric response is limited by the relation $\alpha_{ij}^2 < \varepsilon_{ii}\mu_{jj}$ or more rigorously $\alpha_{ij}^2 < \chi_{ii}^e\chi_{jj}^m$ where χ^e and χ^m are the electric and magnetic susceptibilities. This means that the magnetoelectric effect can only be large in ferroelectric and/or ferromagnetic materials. To date the largest magnetoelectric responses have been observed in composite materials consisting of a magnetostrictive and a piezoelectric material and in multiferroic materials [2].

1.4 Interfaces in Complex Oxides

As discussed in the previous section, complex oxides exhibit many intriguing properties. Competition of charge, spin, orbital and lattice degrees of freedom in these materials leads to new electronic, magnetic and structural phases in strongly correlated electron systems such as high T_C superconductivity in cuprates, colossal magneto-resistance in manganites, and magnetoelectrics or multiferroic phases in other systems. Different from the bulk properties, interfaces in such materials provide a new playground to these degrees of freedom and a powerful approach to couple and manipulate order parameters in order to create materials with novel functionalities. Moreover, novel phases localized only at interfaces between two materials have been observed, e.g. a 2-D electron gas at $LaAlO_3$-$SrTiO_3$ interfaces, ferromagnetic order in a superconducting material at the $YBa_2Cu_3O_{7-x}$-$La_{0.7}Ca_{0.3}MnO_3$ interface, and an induced ferromagnetic state in $BiFeO_3$ at the $BiFeO_3$-$La_{0.7}Sr_{0.3}MnO_3$ interface. Magnetic, ferroelectric as well as structural domain walls emerge as a special kind of interface exhibiting properties distinctly different from the rest of the material. For example, walls in multiferroics can be ferromagnetic even if the domains themselves are antiferromagnetic or paramagnetic. Spin rotations across domain walls in magnetic insulators can induce an electric polarization in the otherwise non-polar materials.

Multiferroic $BiFeO_3$ is a prototypical system for studying the interactions between charge, spin, orbital and lattice degrees of freedom. Its robust ferroelectricity and canted antiferromagnetism provide unique opportunities to create new functionalities at its interfaces. Interfaces between the same structural phase of $BiFeO_3$ but with different ferroelectric polarizations or antiferromagnetic ordering are represented in domain walls. It will be shown in Chapter 3 that the canted magnetic moment found in bulk $BiFeO_3$ can be enhanced at certain domain walls, while the same domain walls also conduct at a semiconductor level (Chapter 4). As a result, a large magnetoresistance behavior ($\sim$60% negative magnetoresistance) is expected and observed (Chapter 5) in 2-D arrays of these domain walls. Moreover, in highly strained $BiFeO_3$ thin films exhibit unique phase boundary between the rhombohedral-like and tetragonal-like phases. Since the adjacent phases have very different crystal structure, ferroelectric polarization and magnetic properties, the discontinuities and constraints at the phase boundaries as well as individual phases will very likely generate novel properties and phenomena, which will be discussed in detail in Chapter 6.

Chapter 2

Domains and Domain Walls in $BiFeO_3$

This chapter focuses on the basic concepts behind the formation of domains and domain walls. The formation of ferroelectric and antiferromagnetic domains and domain walls of $BiFeO_3$ thin films is examined, understood and carefully controlled by the application of piezo-response force microscopy, X-ray spectroscopy and photoemission electron microscopy.

2.1 Origin of Domains and Domain Walls

The domain formation is caused by the energy competitions in order to minimized the total free energy of the materials. In a ferromagnet, for example, a single domain state would minimize the exchange interaction energy. However, other contributions to the total energy need to be considered. The free energy of a ferromagnet can be written as

$$F = E_{ex} + E_D + E_k + E_\lambda + E_H \tag{2.1}$$

where E_{ex} is the exchange energy; E_D is the magnetostatic energy, which represent the energy associated with the magnetic stray field; E_k is the magnetic anisotropy energy; E_λ is the magnetostrictive energy related to the deformation of the system; and E_H is the energy of domains in external field. An example of domain formation is shown in Figure 2.1, where the exchange interaction and magnetostatic energy are considered as the dominate factors in the system. With a single ferromagnetic domain, illustrated as Figure 2.1a, the exchange energy is minimized but the whole material generates a large magnetic field in the space which enhance the magnetostatic energy. When the material break into ferromagnetic domains with magnetization anti-parallel to each other (Figure 2.1b and c), the magnetostatic energy is significantly reduced with some scarification of exchange energy during the formation of the domain wall. Enclosure magnetic domain structure (Figure 2.1d and e) generate negligible stray field, which sacrifices the exchange energy at the domain walls and anisotropy energy for the spins lying away from their magnetic easy axis. This domain configuration is the most common one is magnetic materials.

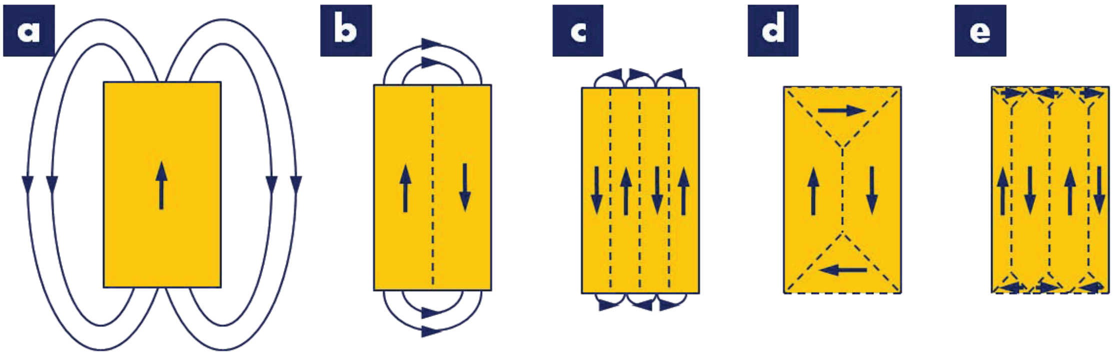

Figure 2.1: Reduction of the magnetostatic energy by domain formation in a ferromagnet.

In the case of ferroelectric materials, we have a similar formula for its free energy,

$$F_1 = F_1^0 + \int \left(\frac{\alpha}{2}D^2 + \frac{\gamma}{4}D^4\right) dV + E_w + E_E \tag{2.2}$$

where E_w is the domain wall energy; and E_E is the depolarization energy. The competition of these energy terms breaks a crystal into domains.

The areas where the transition occurs from one domain to its neighbors are called domain walls. The properties of domain walls are also determined by the competition of different energy terms.

In ferromagnetic domain walls, the energy competition occurs between exchange energy and magnetic anisotropy energies. Then, the energy of a ferromagnetic domain wall can be written as [18] [19]

$$\sigma = \sigma_{ex} + \sigma_{anis} = K_u d + \frac{JS^2\pi^2}{da} \tag{2.3}$$

where a is the lattice constant and d is the width of the ferromagnetic domain wall. The first term in the this expression above represents the anisotropy energy; and the second term is the exchange interaction energy.

Considering the case of forming a 180° ferromagnetic domain wall, to minimize the energy, we find

$$\frac{\partial \sigma}{\partial d} = 0 \tag{2.4}$$

In this case, the domain wall energy can be written as

$$\sigma_w = 2\pi\sqrt{AK_u} \tag{2.5}$$

Therefore, the domain wall width can be calculated as

$$d = \pi\sqrt{\frac{A}{K_u}} \tag{2.6}$$

with exchange stiffness of the domain wall as

$$A = \frac{JS^2}{a} \tag{2.7}$$

Taking the bulk iron as an example, where its $K_u = 0.46 \times 10^5$ J/m^3, the width of the ferromagnetic domain wall can be estimated as $d \sim 50$ nm ($N \sim 200$).

In ferroelectric domain walls, the largest energy contributions are from dipole-dipole interaction and ferroelectric anisotropy, and the energy of a ferroelectric domain wall can be expressed as

$$\sigma_w = \sigma_{dip} + \sigma_{anis} \simeq \frac{10^{-14}}{Na^2} + \frac{1}{2}c_{33}z_z^2 Na \text{ erg/cm}^2 \tag{2.8}$$

where c_{33} is the elastic constant; z_z is the spontaneous strain; and a is the lattice constant. Similar as ferromagnetic domain walls, by minimizing σ_w, the width of the domain wall can be calculated as [20]

$$N \simeq \sqrt{\frac{2 \times 10^{-14}}{c_{33}z_z^2 a^3}} \tag{2.9}$$

Let's take room temperature ferroelectric $BaTiO_3$ as an example. $BaTiO_3$ has the following characteristics: $c_{33} = 2.0 \times 10^{12}$ dynes/cm^2, $z_z = 7 \times 10^{-3}$, $a = 4.0 \times 10^{-8}$cm. The width of the domain wall can be estimated as

$$N \sim 1 - 10 \text{ unit cells, or } d \sim 2 - 3 \text{ nm} \tag{2.10}$$

The estimates above show that the width of the ferroelectric domain walls is usually two orders of magnitude smaller than the ferromagnetic domain walls. This suggests that in ferroelectric materials the dominate energy term is the anisotropy and in ferromagnetic materials the dominate energy is exchange interaction.

2.2 Ferroic Orders and the formation of domains in $BiFeO_3$

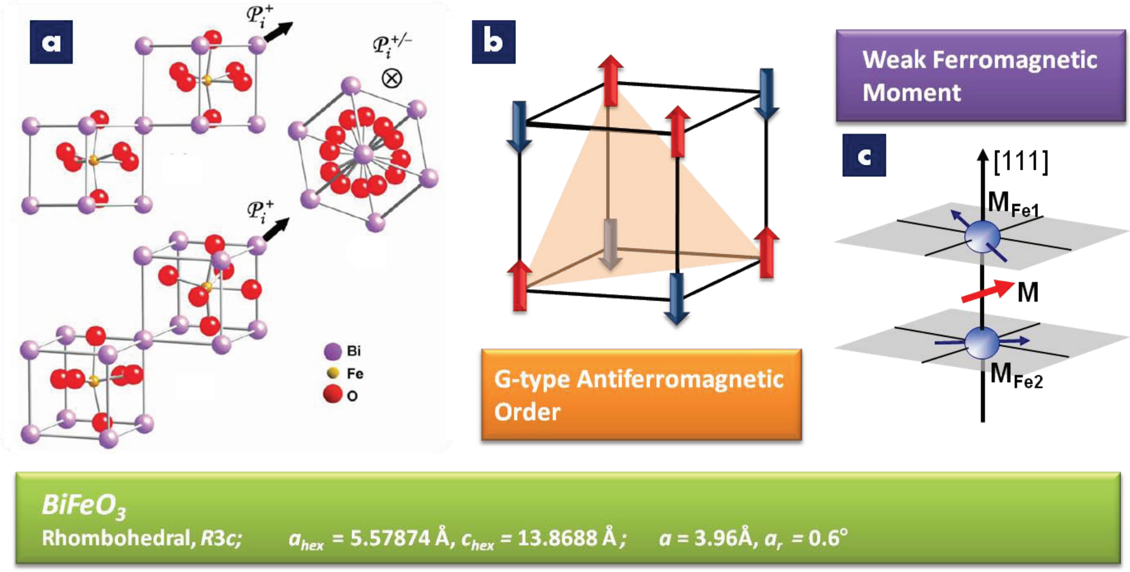

Figure 2.2: Ferroic orders in $BiFeO_3$. (a)Rhombohedral $BiFeO_3$ with ferroelectric polarization along $\langle 111 \rangle$ type directions. Each rhombohedral unit cell can be decomposed into two pseudo-cubic lattices offset along this $\langle 111 \rangle$ direction. Oxygen octahedra are rotated in opposite directions along this $\langle 111 \rangle$ axis within these two pseudo-cubic cells. (b) G-type antiferromagnetism in $BiFeO_3$. The antiferromagnetic easy plane is the (111) plane, which is perpendicular to the local ferroelectric polarization. (c) Weak ferromagnetic moment in $BiFeO_3$ thin films from the cantings of Fe spins.

The perovskite $BiFeO_3$(BFO) was first synthesized in the late 1950s, and as early as the 1960s BFO was suspected to be an antiferromagnetic, ferroelectric multiferroic.

Recent studies of BFO thin films have shown the existence of a weak ferromagnetic response, resulting from a small canting of the antiferromagnetic moments (Figure 2.2c) due to the Dzyaloshinskii-Moriya interaction of the antiferromagnetic sublattice. The atomic structure of BFO is characterized by two distorted perovskite blocks connected along the body diagonal (pseudocubic $\langle 111 \rangle$)building a rhombohedral unit cell (Figure 2.2a). As a consequence, the ferroelectric polarization can be orientated along the four pseudo-cubic diagonals. In bulk, BFO is a G-type antiferromagnet (Figure 2.2b) and its easy plane is lying perpendicular to the ferroelectric polarization.

2.2.1 Ferroelectric domains

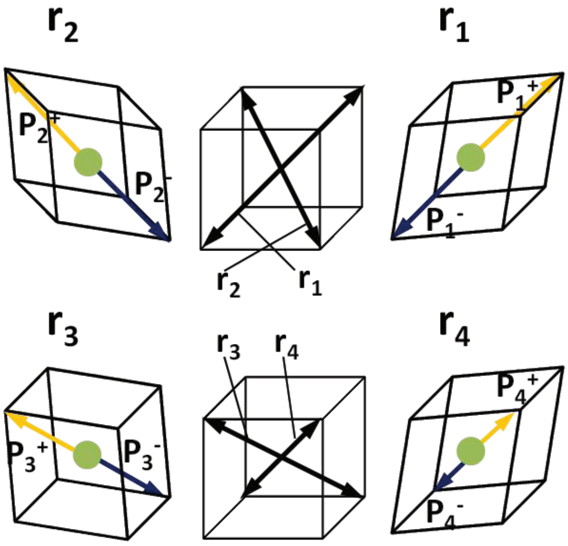

Figure 2.3: Four rhombohedral structural variants and eight possible ferroelectric polarization directions in $BiFeO_3$.

In the rhombohedral phase, BFO has four structural variants, r_1, r_2, r_3, and r_4 (Figure 2.3) with rhombohedral distortions along the four body diagonals of the pseudocubic lattices. [21] Consequently, the ferroelectric polarization of BFO can point in eight possible directions, illustrated as $P_i^{+/-}$ in Figure 2.3. In order to study the ferroelectricity of BFO films, a thin layer of bottom electrode is usually inserted between BFO film and the substrates. This conducting layer defines an electrostatic boundary condition to the BFO film on top and eliminates one possible out-of-plane (OOP) component of ferroelectric polarization. In the case of a $SrRuO_3$ (SRO) bottom electrode on (001) $SrTiO_3$ (STO) substrates, this electron-rich conducting layer only allows P_i^- ferroelectric polarizations to exist limiting the system to four polarization directions.

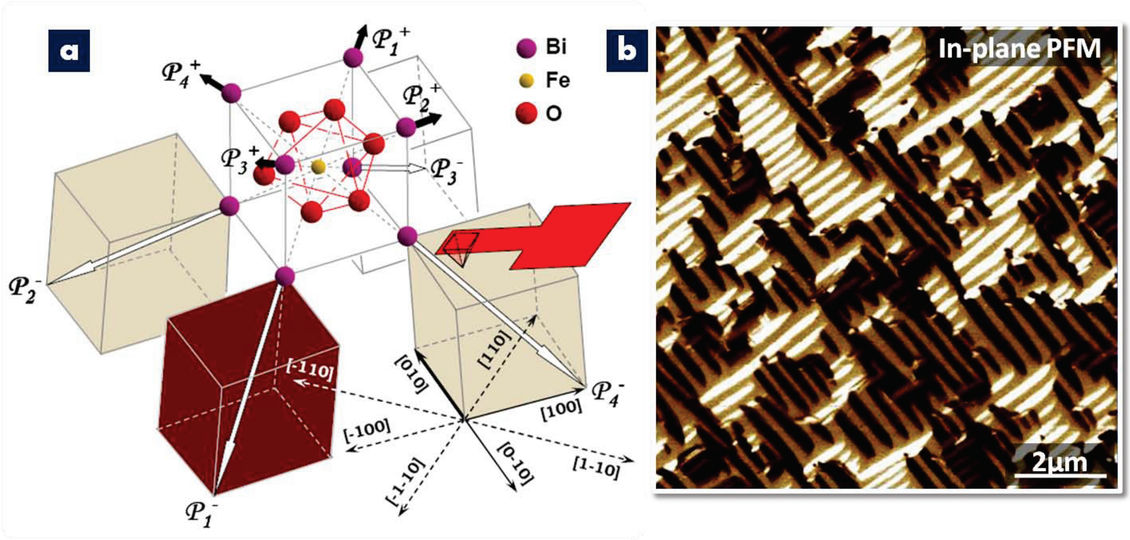

Figure 2.4: Piezo-response force microscopy study of ferroelectric domains in $BiFeO_3$. (a) Correlation of IP-PFM contrast to four ferroelectric polarization variants with down OOP component. PFM cantilever is scanning along $[1\bar{1}0]$ direction. (b) IP-PFM image of ferroelectric domain patterns in $BiFeO_3$.

An in-plane (IP) piezo-response force microscopy (PFM) image is shown in Figure 2.4b, which presents beautiful stripe-like ferroelectric domain patterns. Here, the PFM cantilever is scanning along $[1\bar{1}0]$ direction, and is only sensitive to the IP component of a ferroelectric polarization in $[110]$ and $[\overline{11}0]$ directions. The white regions in this image indicate a ferroelectric polarization along $[11\bar{1}]$ (P_3^- in Figure 2.4a); the dark areas indicate a polarization along $[\overline{111}]$ (P_1^-); the neutral brown part corresponds to IP component of ferroelectric polarization along the scanning direction. The correlations between the ferroelectric polarization variants and PFM contrasts are summarized in Table 2.1.

The direction of the ferroelectric polarization can be altered or "switched" by an external electric field. In BFO, there are three types of possible switching events, 180°, 109°, and 71°, as schematically illustrated in Figure 2.5a. The angles refer to the change in orientation between the initial ferroelectric polarization (P_1^+) and the polarization direction after electrical switching (P_1^-, P_4^-, and P_3^-, respectively). Ferroelectric switching events can be easily induced by applying an external electric field on a PFM tip while scanning close to the film surface. Figure 2.5b and c are the corresponding OOP/IP-PFM images of BFO film after applying an electric field. The dark area in Figure 2.5b indicates the OP polarization reversal from down to up; and combined with the change of domain patterns in the IP-PFM image, we can conclude that the ferroelectric switching events on the four edges of the switched area are 180° and 109° types, and inside the area is 71° type.

Table 2.1: Correspondence of the ferroelectric polarization variants to IP and OOP PFM contrasts with cantilever scanning along $\langle 110 \rangle$.

OP contrast	IP contrast	Possible orientations
Dark (up)	Dark (left)	$[\bar{1}\bar{1}1]$
Dark (up)	Light (right)	$[111]$
Dark (up)	Brown (no torque)	$[\bar{1}11]$, $[1\bar{1}1]$
Light (down)	Dark (left)	$[\bar{1}\bar{1}\bar{1}]$
Light (down)	Light (right)	$[11\bar{1}]$
Light (down)	Brown (no torque)	$[\bar{1}1\bar{1}]$, $[1\bar{1}\bar{1}]$

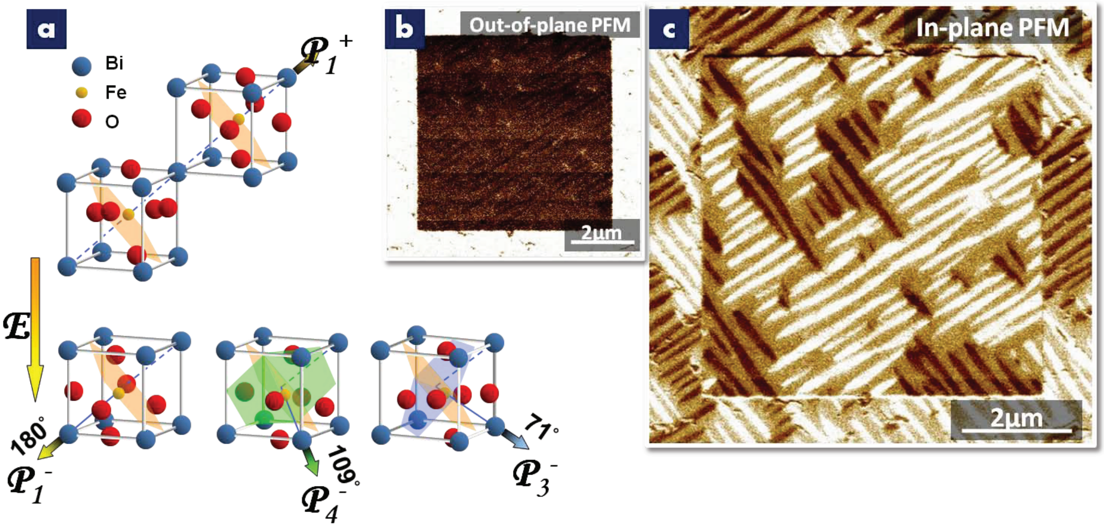

Figure 2.5: Three types of ferroelectric switchings in BiFeO$_3$ films. (a) Schematic of 180°, 109°, and 71° switchings from an P_1^+ initial polarization state in a downward external electric field. (b) OOP-PFM image of a BiFeO$_3$ film on STO(001) substrate with a middle boxed switched by a PFM tip at -8V DC bias. (c) Corresponding IP-PFM image of the same area shown in (b).

The correlation between different types of ferroelectric switching events and the change in IP- and OOP-PFM images is as well summarized in Table 2.2.

Table 2.2: Correlation between ferroelectric switching mechanism and change in IP- and OOP-PFM images.

Switching mechanism	PFM with cantilever along ⟨110⟩	
	In-plane	Out-of-plane
71°	Unchanged light Unchanged dark/white	White↔Dark
109°	Light↔White Light↔Dark	
180°	Unchanged light Dark↔White	

2.2.2 Antiferromagnetic domains and the coupling between antiferromagnetism and ferroelectricity

In antiferromagnets, the net magnetization is zero, i.e. in contrast to ferromagnetic systems there is no macroscopic stray field and therefore no energetic benefit in the formation of enclosure domain structures. However, in multiferroic BFO, ferroelectric as well as antiferromagnetic order are present simultaneously. Both order parameters are coupled through crystal lattice as both are reflected and influenced by the rhombohedral distortion of the lattice. From first principle calculation [22], it is known that the magnetic energy is minimized when the spins are lying in the plane perpendicular to the rhombohedral distortion axis. The ferroelectric polarization is also aligned along this axis. As a consequence a one to one correlation between ferroelectric domain pattern and antiferromagnetic domains is expected.

Antiferromagnetic domains can be observed by PEEM with linearly polarized incident X-rays. The PEEM image in Figure 2.5a is essentially a 2-D map of X-ray magnetic linear dichroism signal, which is sensitive to the orientations of the antiferromagnetic easy axis. The dark and light areas in these images indicate that the antiferromagnetic easy axes of these areas are aligned along different directions, i.e. antiferromagnetic domains are present.

Since the antiferromagnetic easy plane is always perpendicular to the ferroelectric polarization, certain types of ferroelectric switching should be able to influence the antiferromagnetic easy planes. 180° ferroelectric switching only rotates the polarization to be antiparallel to its initial state, which remains the rhombohedral distortion axis of the crystal in the same direction. The antiferromagnetic easy plane is not affected by this ferroelectric switching event. However, both 71° and 109° ferroelectric switching alter the rhombohedral distortion axis, which in turn is expected to lead to the rotation of the antiferromagnetic easy plane (Figure 2.6c). In order to observe this type of electrical control of antiferromagnetic order, we electrically switched ferro-

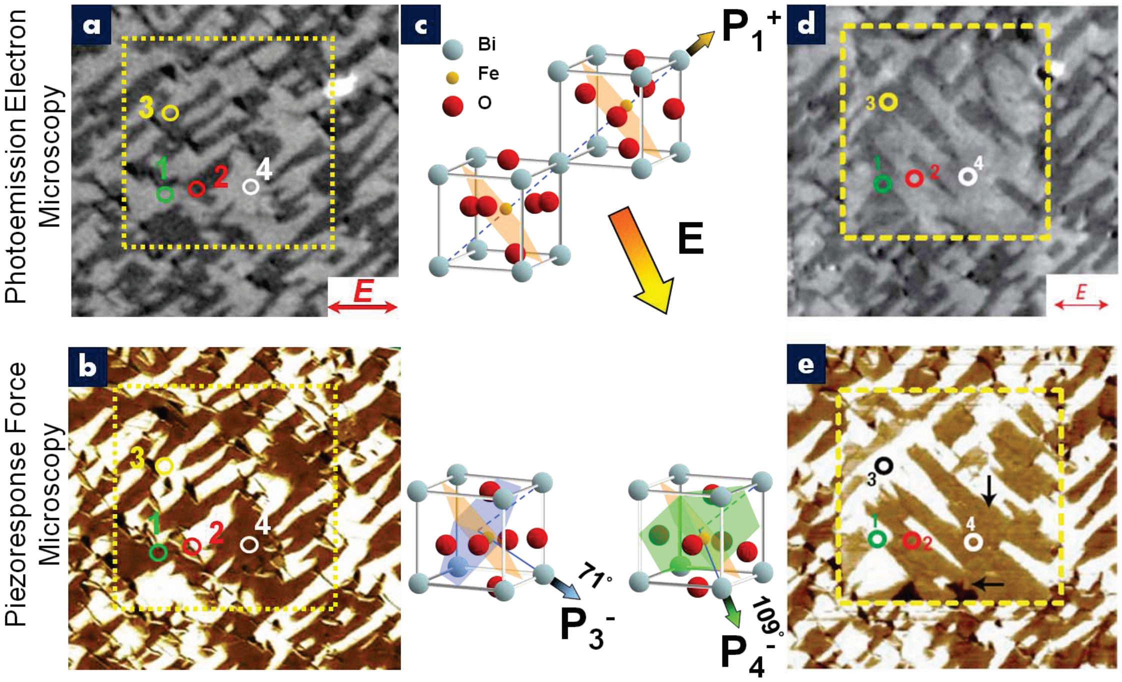

Figure 2.6: Antiferromagnetic domains in $BiFeO_3$ and the coupling between antiferromagnetic and ferroelectric domains. (a) Photoemission electron microscopy (PEEM) image showing antiferromagnetic domain patterns of BFO film on STO(001) substrate. (b) The corresponding IP-PFM image of the same area showing the ferroelectric domain patterns. (c) A schematic illustrating the coupling between the rotation of the antiferromagnetic easy plane and the 71° and 109° ferroelectric switching. (d) Antiferromagnetic domains of an electrically switched area (yellow box). (e) The corresponding IP-PFM image of the same area with the switched box.

electric domains (yellow rectangular area in Figure 2.6d and e), and then determined the antiferromagnetic response using PEEM. By comparing the IP-PFM images before and after the ferroelectric switching, different magnetic reversal types of the four areas indicated in Figure 2.6a, b, d, and e can be identified. The results are summarized in Table 2.3. Both area 1 and 2 experience 109° switching; area 3 exhibits 71° switching; and area 4 shows 180° switching. Comparing the PEEM images for before and after the electrical switching, it is clear that area 1,2, and 3 change their contrast between dark and light; however, circle 4 remains in the same contrast. This experiment proves the coupling between ferroelectricity and antiferromagnetism as well as the control of antiferromagnetic domains with certain types of ferroelectric switching.

Table 2.3: Relation between different types of ferroelectric switching and the rotation of antiferromagnetic easy plane.

Location	Initial polarization direction	Polarization direction after switch	Switching type	Change of antiferromagnetic oder
1	$[10\bar{1}]$	$[0\bar{1}1]$	109°	Yes
2	$[0\bar{1}\bar{1}]$	$[\bar{1}01]$	109°	Yes
3	$[0\bar{1}\bar{1}]$	$[0\bar{1}1]$	71°	Yes
4	$[10\bar{1}]$	$[\bar{1}01]$	180°	No

2.3 Domain walls in $BiFeO_3$

As a ferroelectric as well as antiferromagnetic multiferroic material, BFO is expected to contain both ferroelectric and antiferromagnetic domain walls. With a weak ferromagnetic moment in thin films, BFO thin films should also have ferromagnetic domain walls. Because of the coupling between the order parameters through the crystal lattice, different types of domain walls are also very likely to be coupled. This section focuses on coupled ferroelectric and antiferromagnetic domain walls. In the following, the domain walls will be labeled by the angle difference between the ferroelectric polarization on either side of the domain walls.

2.3.1 Three types of ferroelectric domain walls in $BiFeO_3$

As described in last section, with the ferroelectric polarization along {111}-type directions, three kinds of ferroelectric switching occur in BFO, which correspond to three types of ferroelectric domain walls, 71°, 109° and 180°. In order to satisfy the electrostatic and elastic conditions across the domain walls, these domain walls form in specific crystallographic planes, i.e. the bi-sector plane of the ferroelectric polarizations on either side of the domain walls, that keep the electric displacement vector $\boldsymbol{D}$ across the domain walls continuous. For example, 71° domain walls form in {110}-type planes; 109° domain walls exist in {100}-type planes; since the ferroelectric polarization on the two sides of 180° domain walls are antiparallel, this kind of domain walls can be formed in any crystallographic plane (Figure 2.7).

Ferroelasticity causes the crystal to deform along the polarization direction. Therefore, 71° and 109° domain walls must also be ferroelasitic domain walls and both electrostatic and elastic energies need to be considered for domain wall formation.

In the last section, we have shown that 71° and 109° ferroelectric switching events are associated with the rotation of antiferromagnetic easy planes. As a consequence, 71° and 109° ferroelectric domain walls must also be antiferromagnetic domain walls,

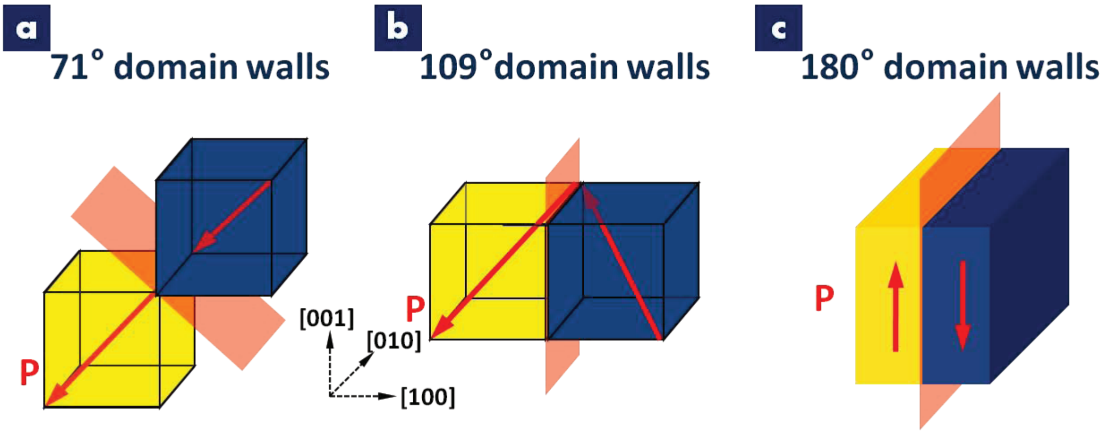

Figure 2.7: Schematics of three types ferroelectric domain walls in $BiFeO_3$. (a) 71° domain wall forms in {110}-type planes (red plane). Ferroelectric polarization changes from $[\bar{1}1\bar{1}]$ (blue cube) to $[\bar{1}\bar{1}\bar{1}]$ (yellow cube). (b) 109° domain wall forms in 100-type planes (red plane). Ferroelectric polarization changes from $[\bar{1}11]$ (blue cube) to $[\bar{1}\bar{1}\bar{1}]$ (yellow cube). (c) 180° domain wall can form in any crystallographic planes. Ferroelectric polarizations are antiparallel on the two sides of 180° domain walls.

separating regions with the antiferromagnetic spin axis oriented along different directions in the crystal lattice. This coupling at the domain walls leads to very intriguing magnetic properties, which will be discussed in Chapter 3 and 5.

2.3.2 Engineering 2-D arrays of 71° and 109° domain walls

Achieving the control of domain patterns and domain walls during the synthesis of thin films is not trivial. This section will summarize a unique approach for engineering domain/domain wall architectures providing model systems for both microscopic and macroscopic measurements. The studies on these samples will be discussed in the following Chapters.

As discussed in the previous section, in case of the $(001)_C$ perovskite surface, there are eight possible ferroelectric polarization directions, corresponding to four structural variants of the rhombohedral ferroelectric thin film. [21] (For simplicity, the subscripts "C" and "O" refer to the pseudo-cubic structures for BFO and orthorhombic structures of $SrRuO_3$ (SRO) and $DyScO_3$ (DSO), respectively.) Domain patterns can develop with either 100_C or 101_C boundaries, which correspond to 109° and 71° domain walls, respectively, for $(001)_C$-oriented rhombohedral films. Figures 2.8a and b show schematics for the two types of predicted periodic domain walls, in which the domains are indicated with the contrast level in their IP-PFM images (Figure 2.9c and f). In both cases, the individual domains in the patterns are energetically degenerate, and thus, equal-width stripe patterns are theoretically predicted.

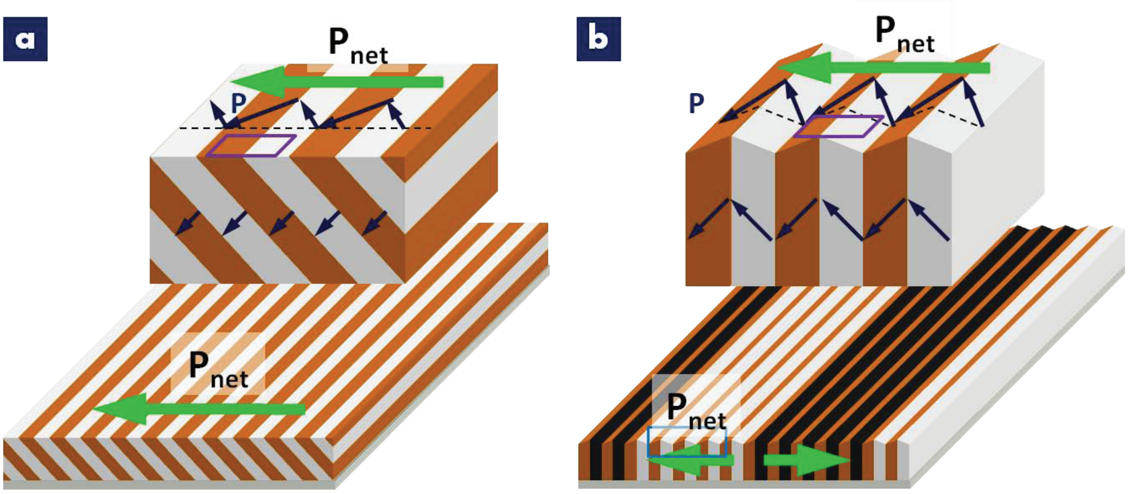

Figure 2.8: Schematics 2-D arrays of as-grown 71° and 109° domain walls. (a) Predicted 71° domain patterns on $DyScO_3$ substrates with 71° domain walls forming in $(101)_C$ plane. (b) predicted 109° domain patterns on $DyScO_3$ substrates with 109° domain walls forming in $(100)_C$ planes.

To control the domain structure, we first tuned the ferroelectric transition temperature (T_c) by isovalent substitution at the Bi site with La (typically 10% La), which has the effect of lowering the T_c value to $\sim 600 - 650$°C (which is below the growth temperature). This concomitantly reduces the lattice parameter of BFO, such that the lattice mismatch with DSO is further reduced. [23] Upon cooling, the phase transformation from the high-temperature cubic phase to the low-temperature rhombohedral phase is assisted by the structural anisotropy induced by the DSO substrate, leading to the preference of two of the four possible structural variants. [24] Previous work has shown that the substrate vicinality [25] can significantly influence the domain evolution. In this work, we have tried to minimized the role of vicinality by using substrates with a miscut angle of <0.3°. Finally, the selection of 71° or 109° domain patterns is dependent on the electrostatic boundary conditions, i.e., the presence of a SRO conducting layer (and its thickness). Qualitatively, in the absence of the conducting SRO layer, the electrostatic boundary conditions at the substrate/film interface favor the formation of 109° domain patterns. If a thick (~50 nm) SRO layer is introduced, the electrostatic boundary condition favors the formation of 71° domain patterns.

La-doped BFO (LBFO) layers (100 nm thick) were deposited on SRO electrodes via pulsed laser deposition at 700°C and in an O_2 pressure of 100 mTorr, with the SRO thicknesses varying from 0 nm to 50 nm. Figure 2.9a shows the topography of such LBFO films grown on a SRO layer. Because of the coherent growth, the film

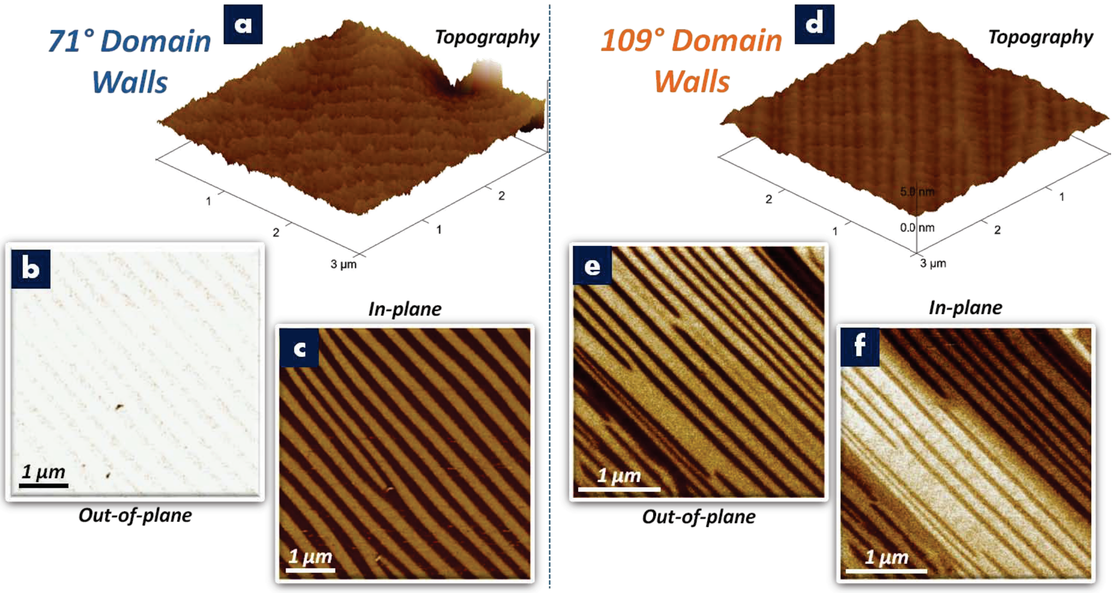

Figure 2.9: AFM and PFM characterization of LBFO films on DSO with and without SRO conducting layer. (a) Surface topography, measured by AFM, of a LBFO film grown on a SRO layer (71° domain pattern). (b) OOP-PFM and (c) IP-PFM images of a LBFO film showing 71° domain walls in the area of (a). (d) Surface topography of a LBFO film grown without a SRO layer (109° domain pattern). (e) OOP-PFM and (f) IP-PFM images of a LBFO film showing 109° domain walls in the area of (d).

surface shows large terraces (∼200 nm wide) that are atomically flat and separated by small steps varying between one-half and one unit cell in height. However, the LBFO films without a SRO layer show a rough or "puckered" surface, [21] as shown in Figure 2.9d. The tilt angle of the surface features (δ in Figure 2.8b) can be estimated from such an analysis to be ∼0.34°, which also corresponds to structural distortion angle, as determined via X-ray diffraction (XRD) analyses. As a consequence, we expect the LBFO films with a sufficiently thick SRO conducting layer should exhibit a 71° domain structure and the LBFO film with only a very thin SRO layer (0-5 nm) should correspond to the 109° domain structure, as shown in Figure 2.8a and b, respectively.

The ferroelectric domain patterns of the areas shown in Figure 2.9a and d were characterized using atomic force microscopy (AFM). [26] PFM images confirm the differences in domain structure shown for 71° and 109° domain walls in LBFO. For the 71° domain wall LBFO samples, OOP-PFM images show uniform contrast (Figure 2.9b), suggesting that all polarization variants are pointing downward, toward the thick SRO layer. IP-PFM images (Figure 2.9c), taken with the cantilever along $\langle 110 \rangle_C$, show a stripe-like image contrast essentially throughout the entire film. In contrast, for the samples corresponding to Figure 2.9d, both OOP (Figure 2.9e) and IP (Figure 2.9f) PFM images, taken with the cantilever along $\langle 110\rangle_C$, show stripe-like contrast over large areas. The key difference is the alternating bright and dark contrast in the OOP image (Figure 2.9e). The change in the OOP contrast signifies a corresponding change in the OOP component of the polarization vector, which is consistent with the interpretation of a 109° rotation of the $\overrightarrow{P}$-vector across the wall. We also note that the observed domain walls in Figure 2.9e and f correspond to both the peaks and troughs of the washboard-like schematic in Figure 2.8b and the surface topography observed in Figure 2.9d. This result is consistent with the stable configuration predicted for a $(001)_C$-oriented rhombohedral ferroelectric film. [21]

While the uniform OOP-PFM contrast of 71° samples indicates a downward ferroelectric polarization component through the whole film, the IP-PFM image (Figure 2.9c) shows a stripe pattern with dark (black) and neutral (brown) contrast, corresponding to domains with the IP components of the polarization directed along $[\bar{1}10]_C$ and $[\bar{1}\bar{1}0]_C$. As a consequence of such a domain structure, the net IP component of the polarization of the whole sample points along $[\bar{1}00]_C$ (green arrow, Figure 2.8a). For 109° domain wall samples, the OOP-PFM image shows two contrast levels, dark (black) and bright (white) (Figure 2.9e), corresponding to the OOP component of the polarization pointing down and up, while the IP-PFM image (Figure 2.9f) has three contrast levels - dark (black), neutral (brown), and bright (white). Dark and bright contrast correspond to the IP component of the ferroelectric polarization pointing along $[1\bar{1}0]_C$ and $[\bar{1}10]_C$ in different ferroelectric domains as shown in Figure 2.8b, while neutral contrast corresponds to the IP component of the ferroelectric polarization pointing either along $[\bar{1}\bar{1}0]_C$ or $[110]_C$. It is noteworthy that bright and neutral (or dark and neutral) domains are usually grouped together to form bright (dark) “domain bands” that are typically a few microns in width, in which the net ferroelectric polarization is directed in opposite IP directions.

Chapter 3

Magnetism of domain walls in $BiFeO_3$

Interfaces have emerged as key focal points of current condensed matter science. In complex, correlated oxides, heterointerfaces provide a powerful route to create and manipulate the charge, spin, orbital, and lattice degrees of freedom. In artificially constructed heterointerfaces, the interaction of such degrees of freedom has resulted in a number exciting discoveries including the observation of a 2-D electron gas-like behavior at $LaAlO_3$-$SrTiO_3$ interfaces [?] [27]; the emergence of the ferromagnetism in a superconducting material at a $YBa_2Cu_3O_{7-x}$-$La_{0.7}Ca_{0.3}MnO_3$ interface [28] and more recently in the discovery of a ferromagnetic state induced in a BFO layer at a heterointerface with $La_{0.7}Sr_{0.3}MnO_3$. [29] In ferroic oxides, such as ferroelectrics, domain walls form natural interfaces as a consequence of the minimization of electrostatic and/or elastic energies. Pioneering theoretical work by Janovec and coworkers used symmetry analyses to predict that domain walls in multiferroics can be ferromagnetic even if the domains themselves are antiferromagnetic or paramagnetic. [30] [31] Spin rotation across domain walls in magnetic insulators can induce a polarization in the walls of otherwise non-polarmaterials [32] [33]. Similarly, coupled behavior at domain walls has been shown in classic antiferromagnets such as $GdFeO_3$. [34] The work of Lajzerowicz and Niez [35] identified the possibility of phase transitions at domain walls in ferroic systems, an aspect that was illustrated in the seminal work of Aird *et al.* [36]. They showed the possibility of superconductivity at twin boundaries in WO_3. A recent study of $YMnO_3$ by T. Choi *et al.* has addressed the formation of interesting insulating, paraelectric states at domain walls. [37]

Among the large number of materials systems currently being explored, the model ferroelectric, antiferromagnet BFO has captured a significant amount of research attention, primarily as a consequence of the fact that the two primary order parameters are robust with respect to room temperature ($T_C \sim 820°C$, $T_N \sim 350°C$) [38] [39]. In the case of BFO, several studies [40] [41] suggested the importance of certain types of domain walls (i.e., 109° walls) in BFO in determining the exchange bias coupling to ferromagnetic layers. Daraktchiev *et al.* obtained a quantitative estimate of the magnetization profile across a domain wall in BFO, [42] suggesting the possibility of enhanced moments at domain walls of between 20-130 emu/cc. Additionally it has been observed that piezomagnetic coupling between ferroelectric and antiferromagnetic domain walls could lead to local moments centered at domain walls [43] and that antiferromagnetic domain wall widths can be significantly larger than ferroelectric domain walls, [43] [44] thereby increasing the net volume of affected material.

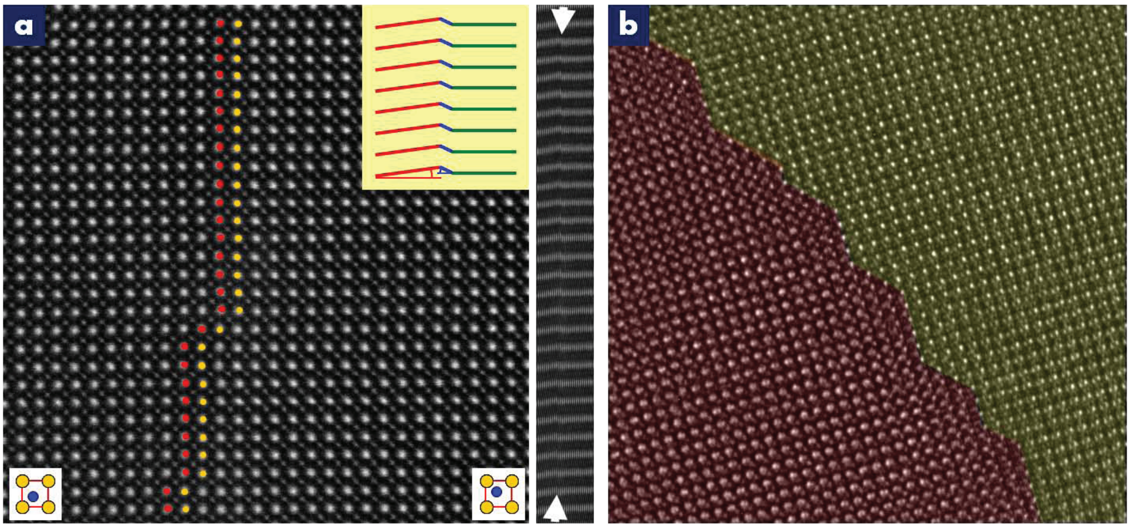

Figure 3.1: Transmission electron microscopy images of 109° and 71° domain walls. (a) High resolution TEM cross-section image of a 109° domain wall clearly illustrating the domain wall plane to be the {100}-type plane. (b) High resolution TEM cross-section image of a 71° domain wall that shows the domain wall plane to be {101}-type. This difference in wall surface palne has critical implications for the presence of an enhanced moment at the wall. The {100}-type planes are not a sysmmetry plane for the rhombohedral structure while the {101}-type planes are.

With this as the background, we set out to explore the role of ferroelectric domain formation on the magnetic properties of BFO thin films. As discussed in previous chapter, rhombohedral ferroelectrics (such as BFO) exhibit three types of domain walls, 71°, 109° and 180° walls. The first two are both ferroelectric as well as ferroelastic and 71° walls are known to form in {101}-type planes while 109° walls are known to form on {100}-type planes. The orientation of the polarization vector changes abruptly (within ~2-3 nm) at the domain walls as imaged by transmission electron microscopy (Figure 3.1). This can result in a symmetry difference between inside the domain walls and in the domain area, then, in turn, the properties at the walls can also be different.

3.1 Exchange coupling between a ferromagnetic layer and $BiFeO_3$ film with 190° or 71° domain walls

The first indication of significant differences in magnetic behavior between these two types of model ferroelectric domain structures comes from exchange coupling experiments. Heterostructures of Pt (2 nm)/$Co_{0.9}Fe_{0.1}$ (CoFe) were grown at room temperature on BFO/DSO samples with either 71° or 109° domain wall arrays in an ion beam sputtering system with a base pressure of $\sim 5 \times 10^{-10}$ Torr. The CoFe films were grown in an applied field of 200 Oe, so as to induce a uniaxial anisotropy. [41] Magnetic measurements were done by surface magneto-optical Kerr effect (SMOKE). An incident beam was focused onto the sample surface by an optical lens and polarized in the plane of incidence (p polarization). The angle of the incidence of the light was 45° from the sample normal. Upon reflection from the sample surface, the light passed through an analyzing polarizer set at 1° from extinction. The Kerr intensity is then detected by a photodiode and recorded as a function of the in-plane applied magnetic field H to generate the hysteresis loop. Heterostructures created on BFO films with 71° domain wall arrays exhibit no exchange bias (Figure 3.2a) with any configuration of applied growth and measurement field. On the other hand, samples created from BFO films with 109° domain wall arrays exhibited strong exchange bias.

In order to fully understand the details of the origins of this exchange bias, the CoFe layer was grown in applied fields direction both parallel and perpendicular to the 109° domain wall surfaces and, in both cases, negative exchange bias was observed (Figure 3.2b and c, respectively). For samples with the growth field applied along the domain wall direction (Figure 3.2b), a *negative* shift of the magnetic hysteresis loop (typical exchange bias field ~40 Oe) is observed while applying the measurement field *antiparallel* to the growth field of the CoFe (red curve, Figure 3.2b). When the measurement field is applied perpendicular to the growth field of CoFe layer, the magnetic response exhibited a hard axis behavior with negligible shift of the hysteresis loop (blue curve, Figure 3.2b). Similar effects were observed in samples where the growth field was applied perpendicular to the domain wall direction (Figure 3.2c). Most importantly, the magnitude of the exchange bias is observed to scale directly with the density of 109° domain walls in the BFO film (Figure 3.2d).

These exchange bias studies suggest some intriguing differences in the magnetic behavior of these two types of domain structures. To better understand this it is important to understand the nature of coupling in these heterostructures. Exchange bias arises from an interaction of the ferromagnet layer with pinned, uncompensated spins in the antiferromagnet that can arise from a multitude of sources, such as the surface termination of crystallographic planes in the antiferromagnet, roughness of the interface between the ferromagnet and antiferromagnet, structural defects, and grain boundaries or domain structures in the antiferromagnet. A perfectly ordered,

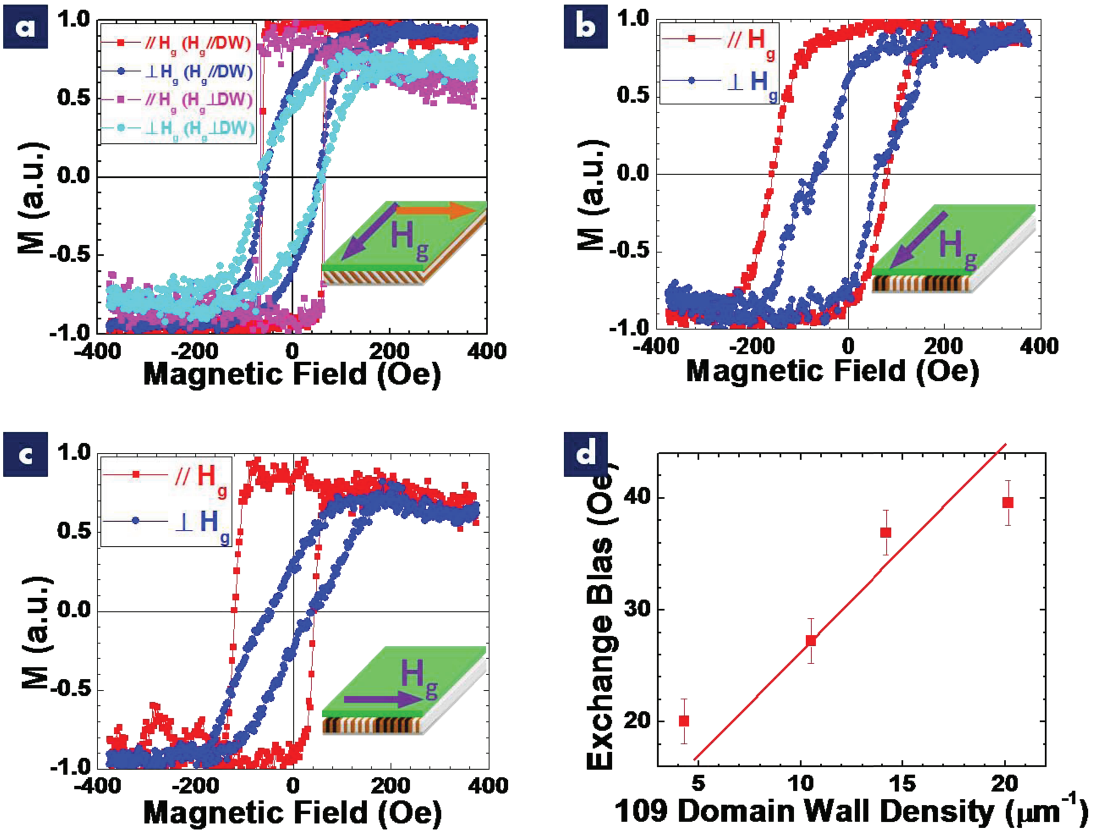

Figure 3.2: Exchange bias on 109° and 71° domain wall BFO films. (a) Hysteresis loops of CoFe on 71° domain wall sample. Red (blue) curve corresponds to the applied magnetic field antiparallel (perpendicular) to the growth magnetic field of CoFe. (b) Hysteresis loops of CoFe on 109° domain wall sample with growth field along the direction of 109° domain walls (c) Hysteresis loops of CoFe on 109° domain wall sample with growth field perpendicular to the direction of 109° domain walls. (d) Dependence of exchange bias field on density of 109° domain walls for CoFe/BFO heterostructures grown on 109° domain wall samples.

atomically-abrupt (001) surface for a single domain of a G-type antiferromagnet such as BFO is a fully compensated surface (i.e., possessing equal number of antiparallel spins). Thus such a surface is not expected to give rise to an exchange bias effect; therefore, to first order, we can eliminate the domain surface as the source of uncompensated spins. It is also possible that differences in surface morphology between the 109° domain wall samples (which have a twinned surface with alternating tilts arising from the structural distortion of the rhombohedral structure, Figure 2.8b and Figure 2.9d) and the 71° domain wall samples (which have flat surfaces with roughness on the order of atomic steps, Figure 2.9a) could play a role in the different exchange bias properties, but this is likely not the dominant factor. From X-ray diffraction and HRTEM studies, the surface planes on the two sides of a 109° domain wall are tilted by an angle of *only* 0.3°. However, the domain surface itself is still a fully compensated surface and as such is not expected to give rise to uncompensated spins or exchange bias. We therefore focus on the magnetic structure of the domain walls (i.e., at the ridges or troughs of the corrugated surfaces).

In the following sections, we are going to focus on investigating the magnetic nature of 109° domain walls, which shows more interesting magnetic behavior than 71° domain walls in exchange bias study.

3.2 X-ray spectromicroscopy study of 109° domain walls in $BiFeO_3$ films

In order to obtain insight into the local magnetic properties, we used element-specific X-ray spectromicroscopy techniques with a strong focus on samples with 109° domain wall arrays. We obtained X-ray absorption spectra (XAS) at the Fe *L*-edge using circularly polarized soft X-rays, at a grazing incidence ($\theta = 16°$), while rotating the sample about the surface normal (here we show data for two angles, $\phi = 0°$, 180°) of a sample possessing only 109° domain walls (Figure 3.3a). Spatially resolved photoemission electron microscopy (PEEM) images were obtained using both left- and right-circularly polarized (LCP and RCP, respectively) X-rays at both the Swiss Light Source (Beamline X11MA) and the Advanced Light Source, Berkeley, CA (PEEM3). In order to enhance the difference in the image contrast between LCP and RCP light, we have taken the ratio of the two images and report that data here. [45] The image contrast is an effective map of the local magnetization vector; regions that have their magnetic moment aligned parallel to the light wave-vector show bright contrast, while those that are antiparallel appear in dark contrast; and this technique is not sensitive to the magnetic moment perpendicular to the wave-vector of the incident X-rays.

X-ray magnetic circular dichroism (XMCD) PEEM images with the wave-vector parallel and antiparallel to the domain walls are shown in Figure 3.3b and c, respectively. For reference, the corresponding IP-PFM image of the same region (Figure 3.3d). It is important to note that each area with a single contrast (i.e., white or brown bands) doesn't correspond to one domain region. Instead, every band with a single contrast level is a bunch of 109° domain walls with the same net polarization in the walls (described at the end of last chapter). For example, brown band corresponds to the black-brown domain wall cluster shown in the schematic in Figure 3.3a; white band corresponds to the white-brown domain wall cluster in the same schematic. Therefore, the contrast in this IP-PFM image essentially shows two types of 109° domain walls in this sample with net ferroelectric polarizations pointing in opposite directions.

We begin by discussing the PEEM images taken 180° from one another (Figure

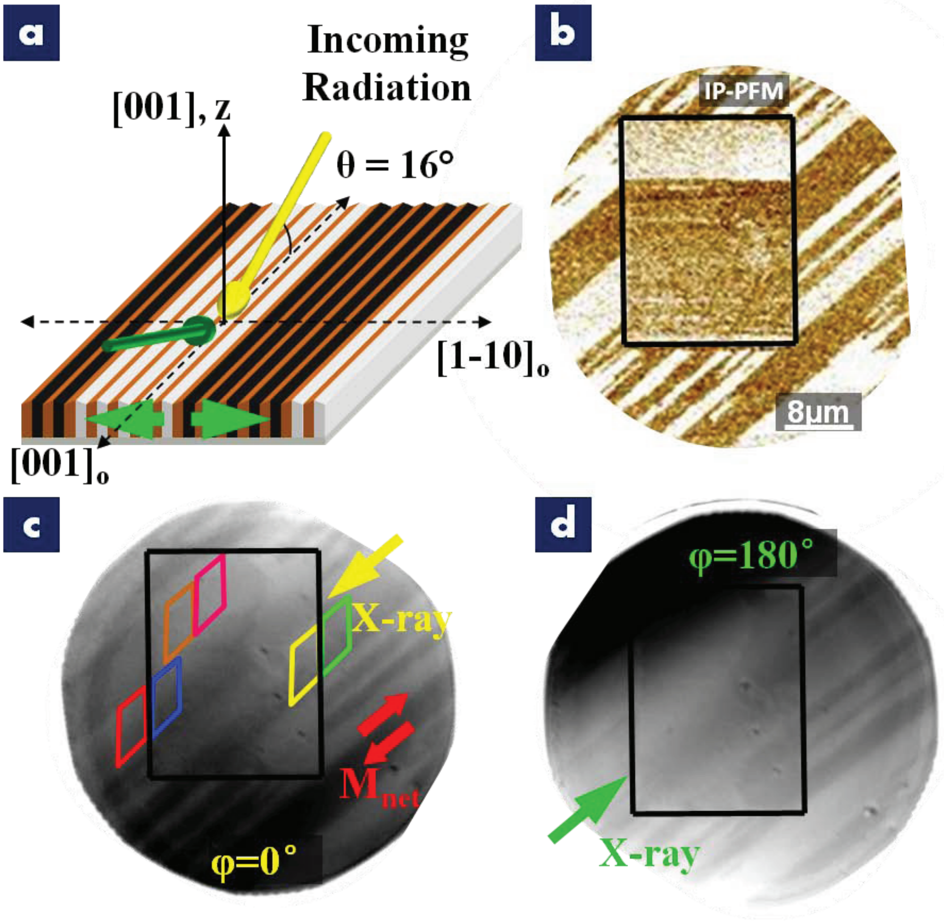

Figure 3.3: Photoemission electron microscopy studies of 109° domain walls. (a) Schematic illustrating the experimental geometries used to take PEEM images of 109° domain walls with circularly polarized X-rays. (b) IP-PFM image of the area that imaged by PEEM, where the 109° domain walls are electrically erased within the black box. (c) PEEM image obtained from the ratio of LCP and RCP images at the first incident angle (ϕ) of the X-rays (shown as yellow arrow in (a)). (d) PEEM image at the second incident angle of the X-rays, 180° away from the first angle respect to the sample normal (shown as green arrow in (a)).

3.3c and d). The most striking feature is the observation of dark and bright "bands" of contrast in the image in Figure 3.3c; the same features reverse their contrast upon rotation of the sample by 180° (Figure 3.3d), identifying the magnetic origin of the contrast. Results of an independent set of measurements carried out on a different sample, this time using the PEEM3 microscope at the Advanced Light Source, Lawrence Berkeley National Laboratory are summarized in Figure 3.4 and are in complete agreement with that presented in Figure 3.3.

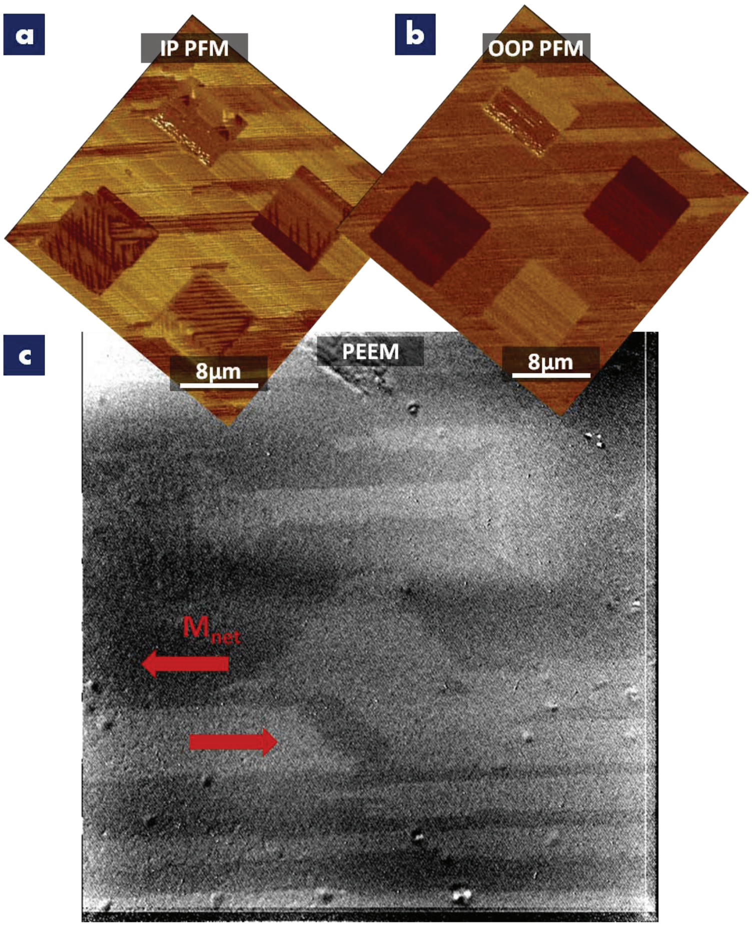

Figure 3.4: Photoemission electron microscopy studies with PEEM3. (a) IP-PFM image of 109° domain wall sample with electrically switched boxes within which the 109° domain walls are erased. (b) Corresponding OOP-PFM image of the same area. (c) Corresponding PEEM image of the same area as shown in (a) and (b).

Due to the resolution limits of the PEEM technique (PEEM at the SLS has a spatial resolution of ∼100 nm under ideal conditions, while PEEM3 has a resolution of ∼30-50 nm), we do not resolve the magnetic information from each of the domain walls individually. What is noteworthy, however, is the fact that bands of 109° domains consisting of an aggregate of individual 109° domain walls, all with the *same* net in-plane component of ferroelectric polarization (demonstrated in Figure 2.8b) also have the same net magnetization direction, as evidenced purely from the image contrast. Within this frame work, rotating the sample by 180° should reverse the image contrast. Indeed, this does happen, as shown in Figure 3.3c and d.

By applying a DC voltage to our scanning probe tip, we can effectively "erase" areas of 109° domain walls. These switching events results in single domain states or in some cases, 71° domain wall ensembles. One such electrically switched region is outlined with a black box in Figure 3.3c and is also evident in Figure 3.4. The final ferroelectric domain configuration has been imaged via PFM (Figure 3.3b) and is shown to consist of a single ferroelectric domain. If the magnetic contrast arises from the presence of 109° domain walls, electrical switching and erasure of the 109° domain walls should also be accompanied by a corresponding change in the magnetic state of that region. Careful comparison of the image contrast in Figure 3.3c and d, and Figure 3.4, clearly shows the relative change in contrast from outside the switched box to that inside.

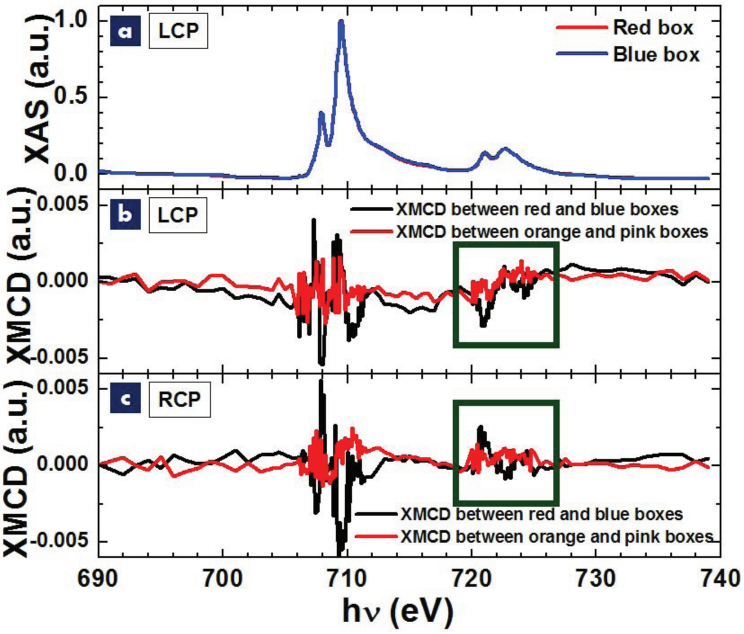

Figure 3.5: XMCD between the selected pair of boxed areas in PEEM image. XAS curves are obtained with LCP incident X-rays. XMCD spectrum is calculated from the asymmetry of XAS curves between each pair of boxed areas. (a) A typical X-ray absorption spectrum showing the L_2,$_3$ edges of Fe. Black curves show the asymmetry difference between locations inside and outside the switched box and red curves show the asymmetry difference between locations inside the switched box for measurements done with (b) RCP and (c) LCP. Note the reversal of the XMCD signal (shown within the dark green boxes) as the light polarity is reversed.

To further validate the conclusions from the PEEM images in Figure 3.3, we carried out detailed spectroscopic measurements at different points throughout the imaged area. Using circularly polarized light, X-ray absorption spectra (XAS) were obtained from within the switched area as well as from outside; a typical absorption spectrum is shown in Figure 3.5. The normalized difference spectra or the asymmetry between the XAS spectra in the switched and unswitched regions gives us a qualitative measure of the difference in ferromagnetic moment between these two areas. The difference spectrum between an area inside (blue box, Figure 3.3c) and outside (red box, Figure 3.3c) the switched box (plotted in black in Figure 3.5) shows an asymmetry of $\sim 1\%$ at the Fe-edge. When the polarization of the incident X-ray is changed from RCP to LCP, the shape of XMCD curve obtained from these red and blue boxed areas is reversed (see boxed areas in Figure 3.5b and c). We note that samples with an as-grown 71° domain structure consistently show no measurable asymmetry in the spectra, i.e., no measurable XMCD signal. Furthermore, we have also examined single domain [111], [110] and [100] oriented films and have observed no measurable XMCD signal. Thus, our X-ray spectromicroscopy experiments strongly suggest the existence of an enhanced magnetic moment in the samples with 109° domain walls, likely emanating at the walls themselves.

Chapter 4

Conduction at domain walls in rhombohedral $BiFeO_3$

This chapter focuses on discussing another merit property of the domain walls in BFO, conduction. Being a robust ferroelectric, BFO is a good insulator with resistivity in the order of 10^7 Ω·m in bulk materials. However, domain walls in rhombohedral BFO show a significantly lower resistivity of 1-10 Ω·m. Here, the conduction at the domain walls will be first discussed as electrically "written" ones, whose location, crystallographic orientation, and type can be precisely controlled by applying an electric field through local scanning probe instruments. Then, the physics of the domain wall conduction is investigated at as-grown domain walls that are better structurally organized. Microscopic measurements were done with high-resolution conductive atomic force microscopy (c-AFM), scanning tunneling microscopy (STM); and macroscopically, devices with in-plane electrodes were also developed to investigate the electronic properties at the domain walls.

4.1 Conduction at written domain walls

Epitaxial BFO films (~100 nm thick) were grown using laser molecular-beam epitaxy (laser-MBE) in (111), (110) and (001) orientations, using carefully controlled single-crystal $SrTiO_3$ (STO) substrates. A thin 50 nm layer of epitaxial $SrRuO_3$ (SRO) was used as bottom electrode for electrical-contact purposes. Ferroelectric domains were imaged using PFM as described in previous chapters. Controlled ferroelectric domain patterns were written using PFM by applying a DC voltage to the probe tip. Local electrical conductivity was measured using high-resolution c-AFM by applying a bias voltage (below the polarization switching voltage) between the conductive AFM tip and the bottom electrode of the sample.

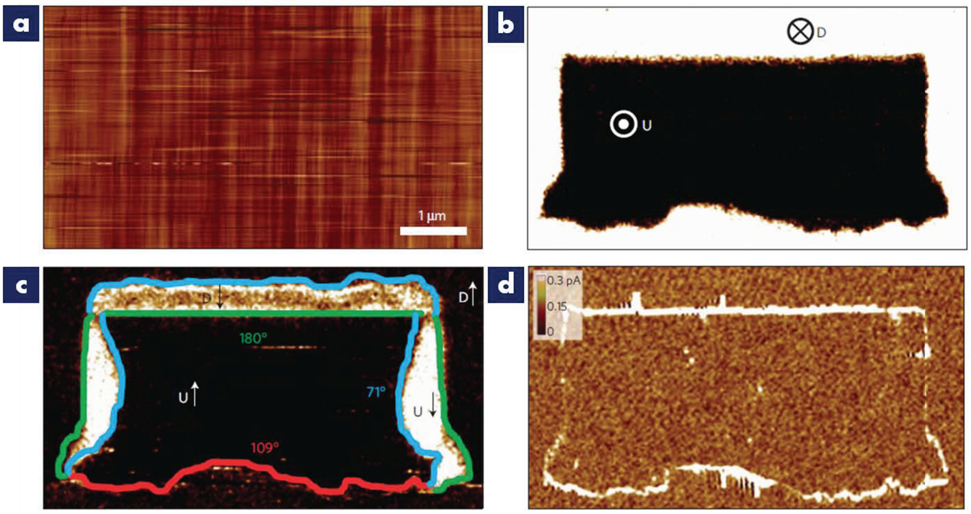

Figure 4.1: Conductivity at different domain wall types. (a) Topography of a BFO (110) thin film, r.m.s. roughness of 0.5 nm. (b) OOP-PFM image of a written domain pattern in a monodomain BFO (110) film showing the OOP polarization component of the domain s to be either down, labelled as "D" (white), or up, labelled as "U" (black). (c) IP-PFM image of a written domain pattern in a monodomain BFO (110) film showing all three thypes of domain wall, that is, 71° (blue), 109° (red) and 180° (green), as inferred from the combination of both OOP and IP-PFM iamges. In these images both the OOP (U or D) component and the IP projection of the polarization direction (shown as an arrow) are also labelled. (d) Corresponding c-AFM image showing conduction at both 109° and 180° domain walls; note the absence of conduction at the 71° domain walls.

100-nm-thick epitaxial films grown on (110) surfaces usually show a two-variant ferroelectric domain structure in the as-grown states with average domain sizes between 5 and 10 μm. Here we used the vicinity of the substrate to get rid of ferroelectric variant and grown the BFO with single ferroelectric domain in (110) orientation. On electrical switching at high fields, all three variations of domain walls can be created [46]; therefore, we begin our study on these (110)-orientated films. The creation of 71° and 109° domain walls can be controlled by different polarity of electric fields. For example, with a as-grown down polarized film, a negative DC bias at the PFM cantilever will produce 109° switching and then generate 109° domain walls in consequence; while a positive DC bias at the PFM cantilever will produce 71° switching and then result in 71° domain walls. However, 180° domain walls are not so trivial to create on (110) oriented films. It has to be created with 71° and 109° switchings on its two sides, thus sandwiched between 71° and 109° domain walls. The created domain walls are imaged with IP and OOP PFM in Figure 4.1b and c. With a careful analysis of PFM contrast (Chapter 2), we identified all the domain walls in this switched pattern. As shown in Figure 4.1c, 71° domain walls are illustrated in light blue; 109° domain walls are illustrated in red; and 180° domain walls are illustrated in green. The corresponding morphology is shown in Figure 4.1a. We measured the RMS roughness of the film to be ∼0.5 nm and there are no observable surface features, either before or after switching.

Then c-AFM measurements were applied at the same area with these written domain walls. The set-up of c-AFM experiment is schematically illustrated as inset in Figure 4.2a. The conducting tip is always grounded, while the bottom electrode of the film (SRO in our case) is applied at a certain DC bias. The spatial resolution of this technique is limited by the tip radius of ∼ 30 nm. Scanning at a DC bias of -1.8V, we got a conduction current map of this area shown in Figure 4.1d. The brightness of the contrast in this map is proportional to the local current level. Compare this current map to Figure 4.1c, it is clear that both 109° and 180° domain walls show significant conduction at this DC bias. However, 71° domain walls do not show a higher conductivity than the domain area within the resolution of our measurements.

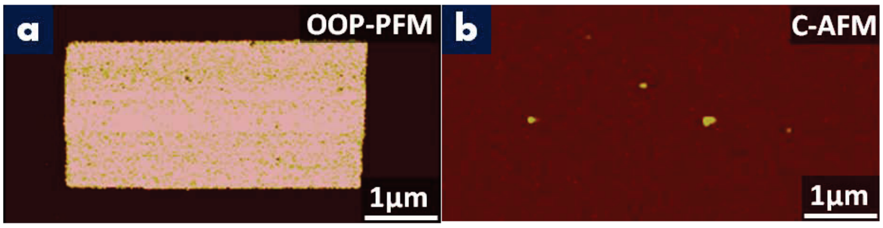

Figure 4.2: Control experiments of conducting-AFM study on $Pb(Zr_xTi_{1-x})O_3$ (PZT) film. (a) OOP-PFM image showing a electrically switched box with 180° domain walls. (b) Corresponding C-AFM image of the same location, where no enhanced conduction at domain walls is observed at any sample bias below the switching threshold (∼4 V).

For comparison, a control experiment has been done with domain walls created in $Pb(Zr_xTi_{1-x})O_3$ (PZT) films (Figure 4.2), which has a band-gap of 3-4.5 eV in bulk. The OOP-PFM image (Figure 4.2a) shows an electrically switched box with

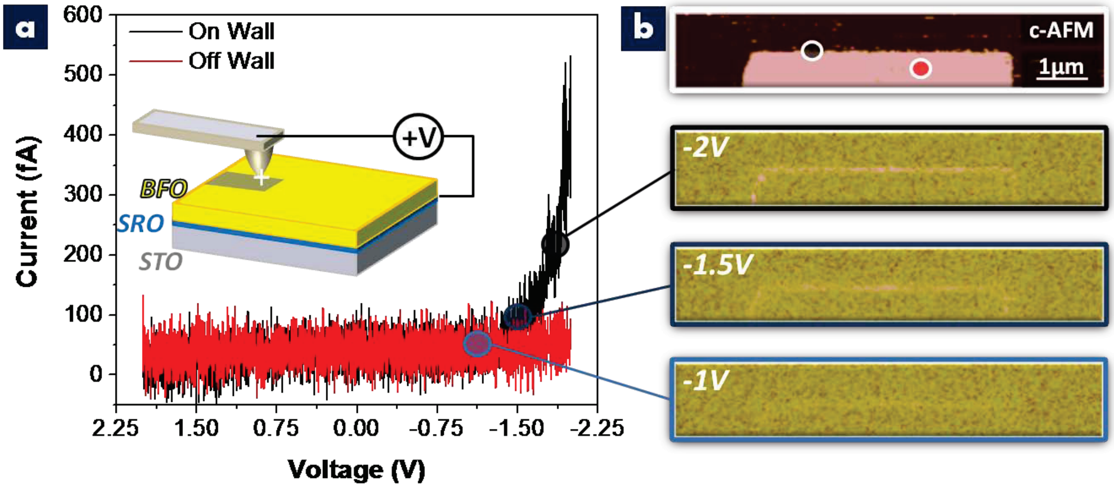

Figure 4.3: Local conduction at domain walls. (a) I-V curves taken both on the 180° domain wall (black) and off the wall (red) reveal Schottky-like behavior. (a)-Inset schematically illustrates the set-up of c-AFM experiments. (b) (Top) OOP-PFM image of a written 180° domain wall in a mono-domain BFO (110) film and (lower) corresponding c-AFM current maps with -1, -1.5 and -2V sample bias made with a Pt-coated tip.

180° domain walls on its edges. Then, C-AFM has been applied at the same area. However, with any sample bias below the domain switching threshold (∼4 V), no current can be observed through the either the domain area or the domain walls (Figure 4.2b). Also, higher sample bias only results in domain switching but still no transport current through the domain walls.

Next we discuss in detail our c-AFM measurements on the (111)-oriented BFO films. Figure 4.3b (top panel) shows a OOP-PFM image of two domain separated by a 180° domain wall. The corresponding c-AFM images (lower panels) show enhanced conduction at the domain wall for applied bias voltages of -1 to -2V. Current-voltage (I-V) curves (Figure 4.3a) show resistive behavior within the domain (red data) and Schottky-like behavior suggesting activated conduction at the domain wall (black data). We repeated our I-V measurements with a number of different c-AFM tip materials – including Pt and N-doped diamond – and found similar Schottky-like behavior with slightly shifted conduction onsets.

Although the current is measured at an applied bias (-2V) that is significantly lower than the switching voltage (typically ±6V), there is a possibility that the current is generated from the local movement of the domain wall, which requires a much lower energy input. In order to prove that the current we observed is not a transient signal, time dependent transport measurement has been employed. As shown in Figure 4.4 (top panel), the c-AFM tip was located at certain spots (colored circles) either on

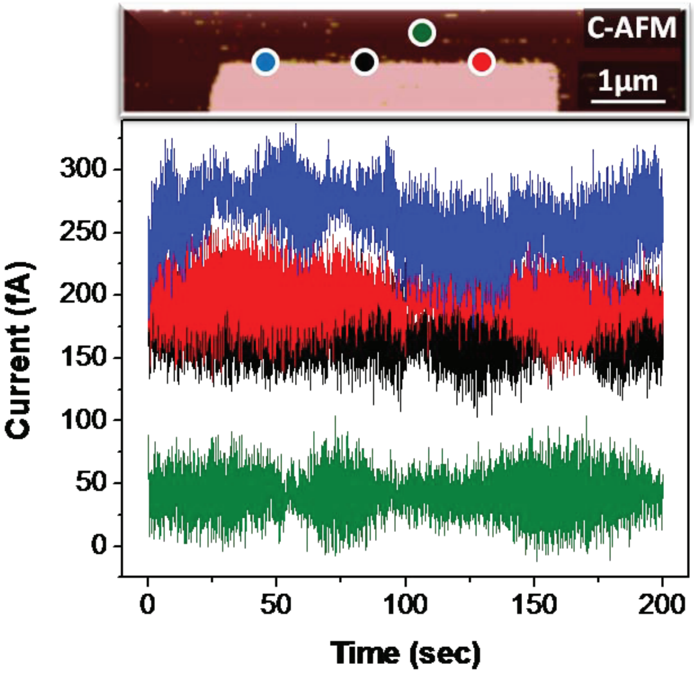

Figure 4.4: Time dependence of the current both on the wall (in black, red, and blue) and off the wall (in green) at an applied sample bias of -2V. Current was measured at locations marked with colored circles in OOP-PFM image (top panel).

or off the domain walls. Then, -2V bias was applied to the bottom electrode of the sample, and the measured current curves are shown in corresponding colors in the lower panel. Within the noise level (∼70 fA), the current measured at all these locations is persistent over a timescale of at least 3 min suggesting a non-transient transport behavior. These time-dependent data indicate that the origin of this current is not displacement of domain walls. However, the fluctuation of the current curves measured on the domain walls in caused by the contact difference between the tip and different locations on the film. In order to get rid of most of the impurities on the sample surface and make a better contact between the tip and the film, we then applied c-AFM measurements in ultra-high vacuum (UHV).

In UHV, the contact between the tip and sample surface is largely improved by getting rid of most of the impurities (Figure 4.5a). 180° domain walls are created in the same way as in air (Figure 4.4). Then, when the tip is located on the 180° domain wall, a Shcottky-like I-V response (red curve in Figure 4.5b) is observed with sample bias ramping from -1 V to -3 V (black curve in Figure 4.5b); while, when the tip is located off the wall, there is no measurable change of the transport current (blue in Figure 4.5b). It is also worth to note that the current level at the domain walls measured in UHV (1-10 nA) is much higher than in air (100-500 fA), which shows a

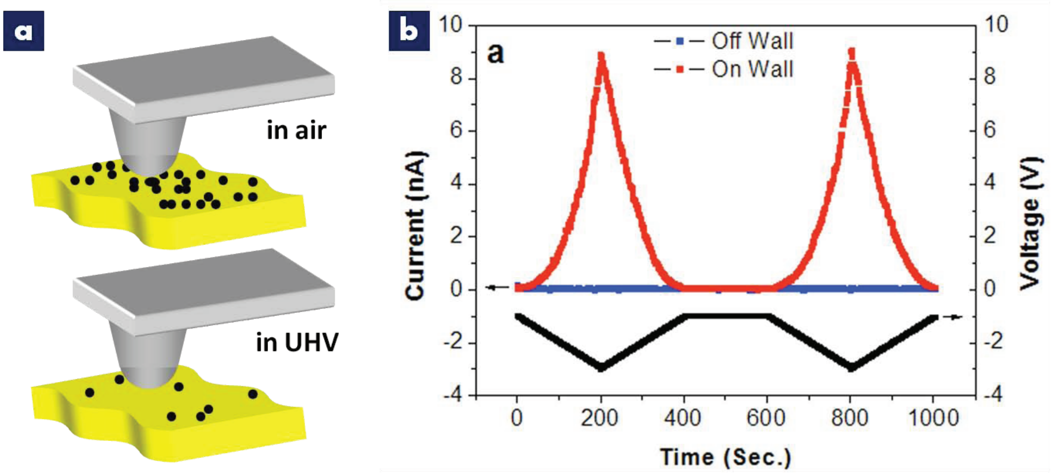

Figure 4.5: C-AFM measurements on domain walls in ultra-high vacuum (UHV). (a) Schematics illustrating the contact difference between measurements done in air and in UHV. Black particles are impurities of the surface of the films. (b) Current measured on (in red) and off (in blue) the domain walls with voltage ramping from -1V to -3 V (in black).

behavior that is closer to the intrinsic properties of domain walls.

The enhanced conductivity at the domain walls gives us a potential possibility of device applications illustrated in Figure 4.6. By creating a simple device structure consisting of in-plane electrodes of SRO separated by a 6 μm spacing (Figure 4.5a), we can measure the I-V characteristics of BFO films and domain walls macroscopically. Additionally, the SRO provides nearly Ohmic contacts with the BFO films and thus we can gain further insight into the conduction of the walls in the gap, without any interference from the AFM tip during the measurement process. Mono-domain (110)-oriented BFO films were grown on top of the SRO in-plane electrode device structures on STO (110) substrates. Conducting domain wall features (here are shown 180° domain walls, Figure 4.6a, right) that connect the two in-plane electrodes were written using PFM. Again, no morphological surface features were observed that correspond to the written domain pattern. I-V measurements (Figure 4.6b) reveal a step-like increase in the measured current between the two in-plane electrodes on addition of a controlled number of conducting domain walls. The steps in conduction are essentially equidistant, increase proportionally to the total number of domain walls written and show completely reversible behavior on erasing a given feature. I-V curves for zero, one, two and three domain features are shown in Figure 4.6b. I-V characteristics of domain walls written with different domain width is also studied, in which it is shown that the conduction is only related to the number of the domain walls, but not the size of the switched domain area. Such material functionality has potential application in both logic and memory applications, as the wall location (and hence electronic conduction) can be precisely controlled on the

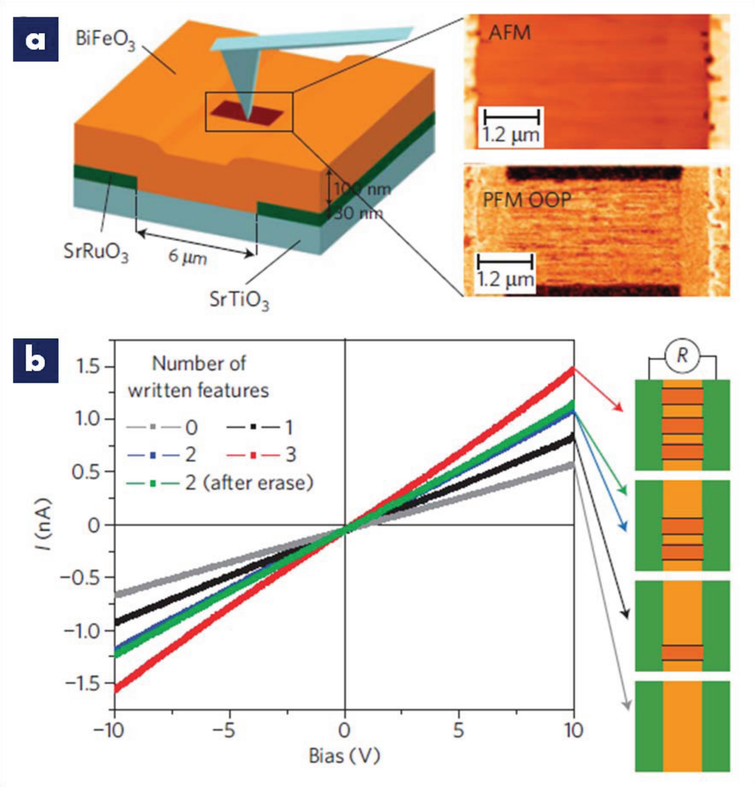

Figure 4.6: Proof of concept for device application. (a) Schematic illustration (left) of in-plane electrode structure (green) and how scanning probe tips can be used to controllably create conductive domain wall features between electrodes. The images on the right show AFM (top) and OOP-PFM (bottom) contrast for this written domain area on a BFO (110) sample. (b) I-V characteristics of the devices measured between the two in-plane electrodes show that the current can be incrementally controlled through creating or erasing the conducting domain walls.

nanoscale. This demonstrates a possible rewritable multiconfiguration device set-up that uses nanoscale conductive channels. (that is, conducting domain walls). Finally, on the basis of a simple sheet-resistance model, we can estimate the resistivity of a single domain wall in BFO to be of the order of 1-10 Ω·m, which is between five and six orders of magnitude lower than for bulk BFO.

Here I am also showing a fun application of the conduction at written domain walls. Figure 4.7 shows two domain patterns of “CAL” and “DOE” with on a (110) oriented BFO/SRO/STO film. As shown in the IP-PFM and OOP-PFM images (top and middle panel in Figure 4.7a and b), the switched domains are created with a 109° switching and have 109° domain walls at all edges. With a C-AFM scan afterwards, both of these patterns show beautiful edge-highlighted letters.

Figure 4.7: “CAL” and “DOE” switched pattern showing conduction at written domain walls. (a), (b) From top to bottom are IP-PFM, OOP-PFM, and C-AFM images of the switched area, respectively

4.2 Structure at domain walls in $BiFeO_3$

To understand the observed electrical conductivity, we performed a combined transmission electron microscopy (TEM) and density functional theory (DFT) study of the domain wall sructure, electronic structure and properties. The structure of domain walls in ferroelectric perovskites and related materials has been the focus of several recent DFT [21] [47] and TEM [48] [49] [50] studies, and the structural distortions associated with ferroelectric domain walls are now reasonably well characterized. However, studies of the associated electronic and magnetic properties are in their infancy. [51] We chose the 109° domain wall (shown schematically in Figure 4.6a) for our study because we do not obtain significant conduction enhancement at 71° domain walls and because imaging of 180° domain walls with high-resolution TEM (HRTEM) present practical problems in terms of locating the wall. We use (001)-oriented samples for the TEM analysis, because we can easily control the density of 109° domain walls during growth for this orientation. TEM images were acquired using the exit-wave reconstruction approach to eliminate the effects of objective-lens spherical aberrations; such images can be directly interpreted in terms of the projection of the atomic columns. [52] A representative image for such a 109° domain wall taken along the [010] zone axis of a cross-sectioned BFO/SRO/STO (001) film in shown in Figure 4.6a. Analysis of this image enables us to determine the lattice parameter in the plane of the film (a) ([100]) and the lattice parameter out of the

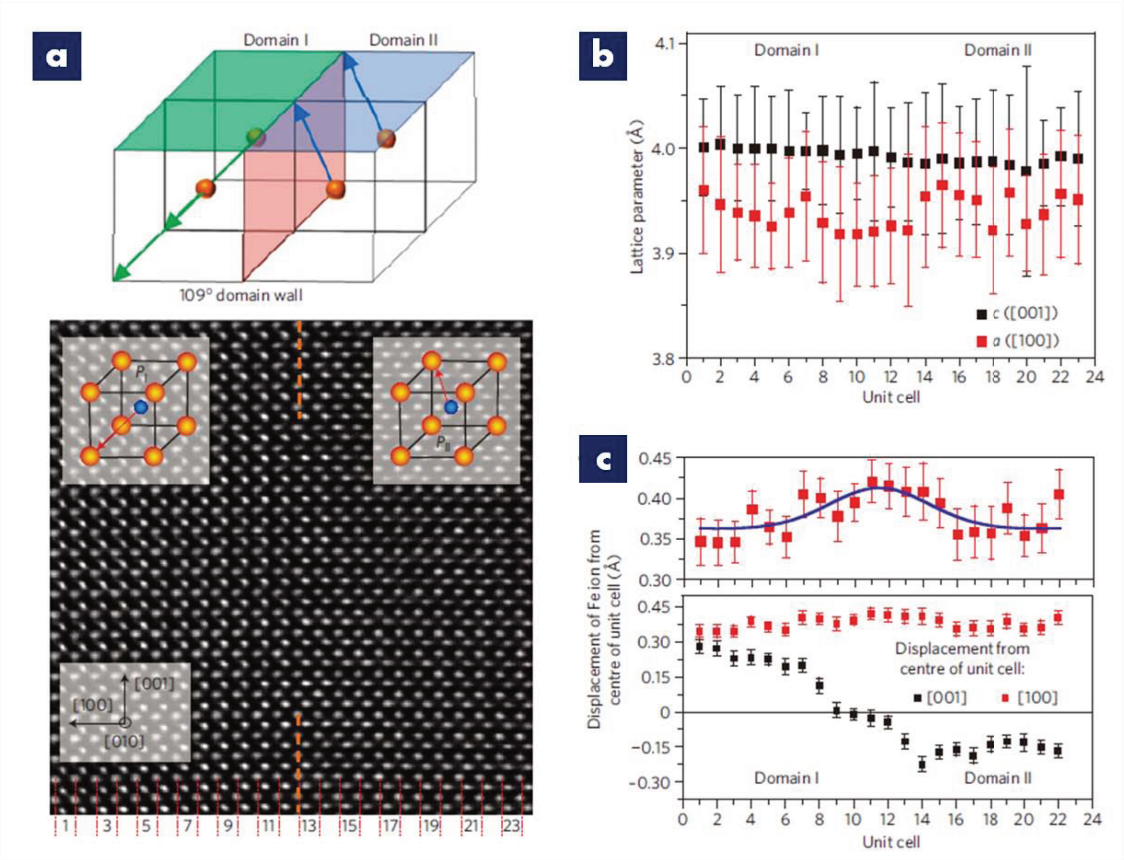

Figure 4.8: Structural analysis of domain walls. (a) Schematic diagram of 109° domain wall and exit-wave-reconstructed HRTEM image of a 109° domain wall imaged along the [010] zone axis. (b) Extracted a and c lattice parameters for each unit cell across the domain wall. (c) Extracted Fe-ion displacement relative to the Bi lattice for each unit cell across the domain wall. A close-up (upper panel) reveals an increase in the component of polarization perpendicular to the domain wall.

plane of the film (c) ([001]) (Figure 4.6b). As expected, the in-plane lattice parameter is slightly smaller and the out-of-plane lattice parameter larger than the value in bulk BFO (3.96 $\mathring{A}$) owing to the strain inherent in the epitaxial films. In addition, we find that both the in-plane and out-of-plane film lattice parameters are unchanged in the vicinity of the domain wall. We also extract the relative displacement of the Fe ion with respect to the Bi sublattice, and resolve it into components parallel ([001]) and perpendicular ([100]) to the domain wall (which lies in a (100) plane running vertically across the image and labeled with a dashed orange line) by quantitative analysis of the HRTEM data (Figure 4.6c); this distance is representative of the local polarization. The component of the displacement parallel to the domain wall (along [001]) decreases in magnitude to zero at the center of the domain wall before changing to the same magnitude (but opposite sign) on the other side of the wall, reflecting the change in polarization orientation of the domain. Interestingly, the perpendicular displacement component (along [100]) shows a small increase at the domain wall; we return to the implications of this later. Similar studies were completed on a 71° domain wall as well. Again, only minor variation in lattice parameters was observed across the domain wall. In this case a similar step in Fe-ion displacement is observed parallel to the domain wall, but we are unable to resolve a step in the perpendicular component across the wall.

To investigate the influence of these structural changes on the electronic properties, we next performed a density functional study of the structure and electronic properties for all three ferroelectric domain wall variants. First we performed full structural optimizations of the ionic positions with the lattice parameters fixed to their experimental bulk values; in particular, the oxygen polyhedral rotations around the polar axis, which are know to have a profound effect on both the magnetic [22] and electronic [53] properties and cannot be easily extracted from the HRTEM data, were accurately calculated. As the sense of the oxygen rotations around the polar axis is independent of the direction of polarization along the axis [22] we studied two scenarios; first we initialized the sense of rotation to the continuous across the domain boundary and second we changed the rotation sense when the polarization direction changed. As expected, we found that domain walls with continuous oxygen rotations are considerably lower in energy, because this avoids formation of an antiphase boundary associated with the octahedral rotations. In addition, we investigate domain wall configurations centered at both Bi-O and Fe-O planes and found the Bi-O walls to the slightly lower in energy, confirming the findings of the HRTEM analysis. Our lowest-energy calculated configuration for the 109° domain wall has a domain-wall energy of 206 $\mathrm{mJ\cdot m^{-2}}$.

To confirm that our calculated structure is consistent with our TEM data, we analyzed the layer-by-layer polarization, defined as the sum over the bulk Born effective charges [53] multiplied by the displacements of the ions from their centrosymmetric reference positions in each layer. As expected, the local polarization in the middle of the domain is close to the value calculated for bulk BFO using the same computationally and experimentally determined lattice parameters ($\sim$93 $\mu\mathrm{C\cdot cm^{-2}}$ [53] [54] [55] [56]), confirming that our supercell is large enough to capture the essential physics. Consistent with our TEM analysis, we find an abrupt change in the parallel polarization component across the domain wall and a small change in the normal component at the domain wall.

Our calculations indicate that this small change in the normal component of the polarization across the 109° domain wall leads to a step in the electrostatic potential (planar and macroscopically averaged) of 0.15 eV across the domain wall (Figure 4.9 and Table 4.1); a similar step was computed and explained previously across 90° domain walls in $PbTiO_3$ [51]. Such a potential step should enhance the electrical conductivity by causing carriers in the material to accumulate at the domain wall to

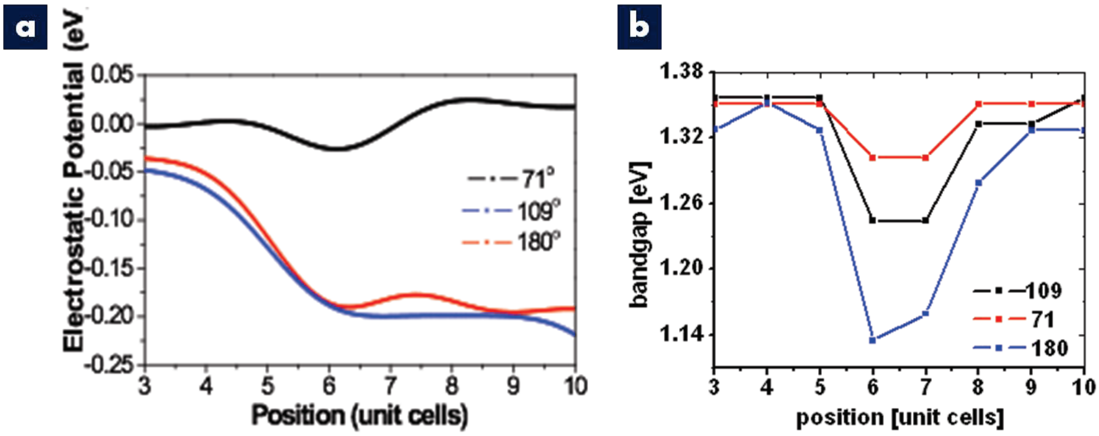

Figure 4.9: Electronic structure across ferroelectric domain walls in $BiFeO_3$. (a) Electrostatic potential change across three types of domain walls. (b) Local Kohn-Sham bandgap change across different domain wall variants. All the domain walls are Bi-centered at position 6.5 in x-axis of the plots.

Table 4.1: Electronic structure at ferroelectric domain walls. Calculated values of the potential step and reduction in band-gap at all three domain wall types.

Domain wall type (°)	Electrostatic potential step (eV)	Change in band-gap (eV)
71	0.02	0.05
109	0.15	0.10
180	0.18	0.20

screen the polarization discontinuity. Our calculations for the 180° domain wall also yield a variation in the normal component of the polarization, and a corresponding potential step of 0.18 eV (Figure 4.9 and Table 4.1). The normal component results from the polarization rotating towards successive adjacent corners of the perovskite unit cell, through a 71° and then a 109° change in the polarization direction before reaching the reversed polarization [57]. This behavior is in striking contrast to the 180° polarization reversal in tetragonal ferroelectrics [51], where the polarization changes in only one direction within the wall plane and no normal component occurs. The 71° wall, however, exhibits no anomaly in the perpendicular component of the ion displacement at the center of the wall, again consistent with our TEM data, and therefore exhibits a negligible electrostatic potential step at the domain wall (Figure 4.9 and Table 4.1).

Finally, we calculate the electronic properties of our structureally optimized domain walls, in particular by comparing the layer-by-layer densities of states in the domain wall and mid-domain regions. Within the central region of the domain, we find, as expected that the local density of states resembles that of bulk BFO, and the local Kohn-Sham band-gap is equal to the value of 1.3 eV obtained for bulk BFO with the same choice of Hubbard parameter U and exchange interaction J, 3 and 1 eV, respectively [53]. (We emphasize that, although the DFT Kohn-Sham band-gaps do not correspond to experimental band-gaps, changes in DFT gaps caused by changes in bandwidth as a consequence of small changes in structure for the same DFT implementation are qualitatively meaningful.) As the domain wall is approached, we find that the changes in the structure do indeed cause changes in the band width and the positions of the band edges. This leads in the 109° (180°) case to a 0.1 eV (0.2 eV) reduction in the band-gap in the domain wall layer from the mid-domain calculated value of 1.3 eV (Table 4.1). For activated conduction at room temperature, such a change in band-gap, or in band-edge offset relative to the Fermi energy of the tip, should lead to considerable changes in conductivity. Consistent with its absence of conduction, the reduction in band-gap in the 71° case is smaller (0.05 eV) (Table 4.1). Interestingly, the magnitude of the band-gap reduction is sensitive to the details of the lattice parameters used in the calculation; if we constrain the lattice parameter to the bulk values, the changes in the band-gap are larger than those for the relaxed structures given in Table 4.1. This suggests that band-structure changes at domain walls might be tunable by epitaxial strain.

4.3 Conduction at as-grown domain walls

Using the method described in section 2.3.2, 2-D arrays of as-grown 109° and 71° domain walls are created on 100 nm thick La-doped (10%) BFO $(011)_C$ thin films on SRO/DSO $(110)_O$ substrates by pulsed laser deposition. With a preliminary PFM and c-AFM study of these BFO films with well aligned 2-D arrays of domain walls, both 109° and 71° domain walls show similar conduction level as the written domain walls (Figure 4.10), where 109° domain walls show a much higher current level (∼5 pA) than 71° domain walls (∼0.1 pA) at a lower sample bias (-1.6 V and -2.2 V for 109° and 71° domain walls, respectively).

In order to investigate more details of transport at the domain walls, we then carried out PFM and c-AFM measurements in UHV environment to investigate the local piezoresponse and conduction properties of these films without interference from surface adsorbates. Since 109° domain walls are more conducting and interesting than 71° domain walls (Figure 4.10), we'll focus more on 109° domain walls in this section. A visual impression of domain structure and the associated change in local conductivity can be seen in Figure 4.11a-c. Here, a clear correlation of 109° domain walls in the material and local conductivity indicated by high c-AFM currents can be seen (Figure 4.11c). The resulting conductive stripes are about 20 nm wide, In order to characterize the associated piezoelectric properties further, we performed local I-V measurements using a c-AFM based setup in UHV. The acquired data for each I-V curve gives insight into the local conduction mechanism at domain walls in the sample [58]. Schottky emission has been shown to be a possible interface limited transport mechanism in ferroelectrics, following

$$I_s = A_{eff}AT^2 \cdot \exp\left\{-\left[\frac{\Phi}{k_BT} - \frac{e}{k_BT}\left(\frac{eE}{4\pi\varepsilon\varepsilon_0}\right)^{1/2}\right]\right\} \tag{4.1}$$

where A is the Richardson coefficient, A_{eff} the effective contact area, Φ the Schottky barrier height and $\varepsilon$the dielectric constant, or a modified version of this expression [59] [60]. Recently, also tunneling into ferroelectric surfaces was investigated and shown to be dominated by the Fowler-Nordheim mechanism, according to [61]

$$I_{FN} = A_{eff} \cdot \frac{e^3 m_{Pt}}{8\pi h m_{BFO}\Phi} \cdot E^2 \cdot \exp\left\{-\left[\frac{8\pi\sqrt{2m_{BFO}}}{3he} \cdot \frac{\Phi^{3/2}}{E}\right]\right\} \tag{4.2}$$

where Φ_B denotes the barrier height, E the electric field, effective A_{eff} tunneling

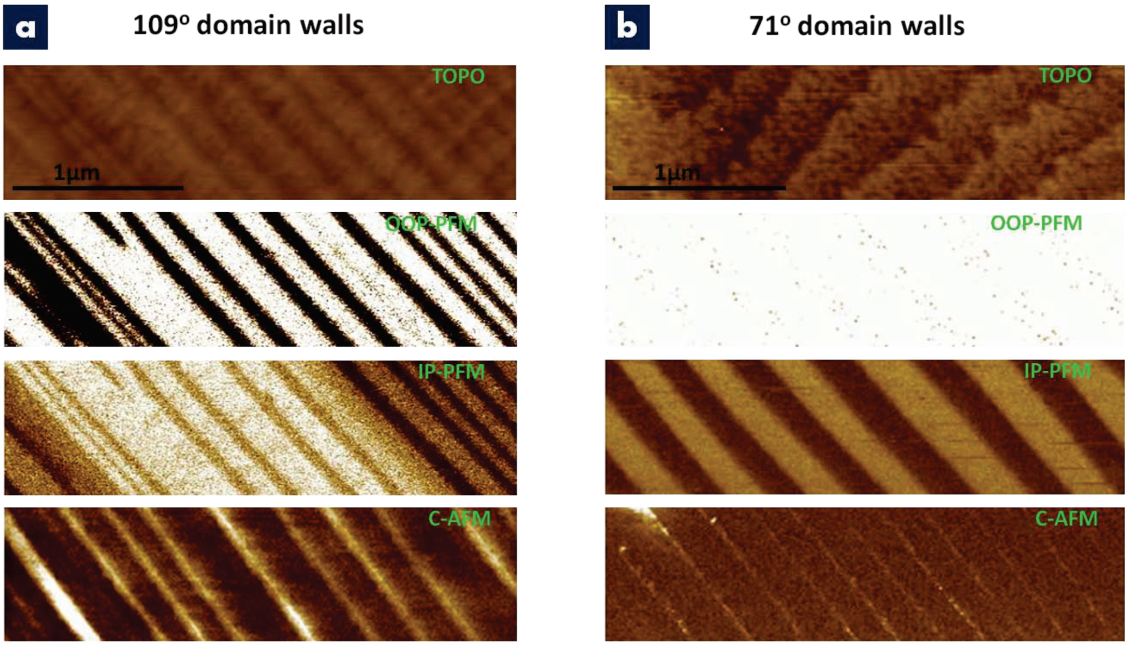

Figure 4.10: Conduction at 109° and 71° as-grown domain walls. (a), (b) From top to bottom: topography, OOP-PFM, IP-PFM, and c-AFM images of as-grown 109° and 71° domain patterns and domain walls. C-AFM images of 109° and 71° domain walls are taken at 1.6 V and 2.2 V, respectively; and the current scales shown are 5 pA for 109° domain walls and 0.2 pA for 71° domain walls.

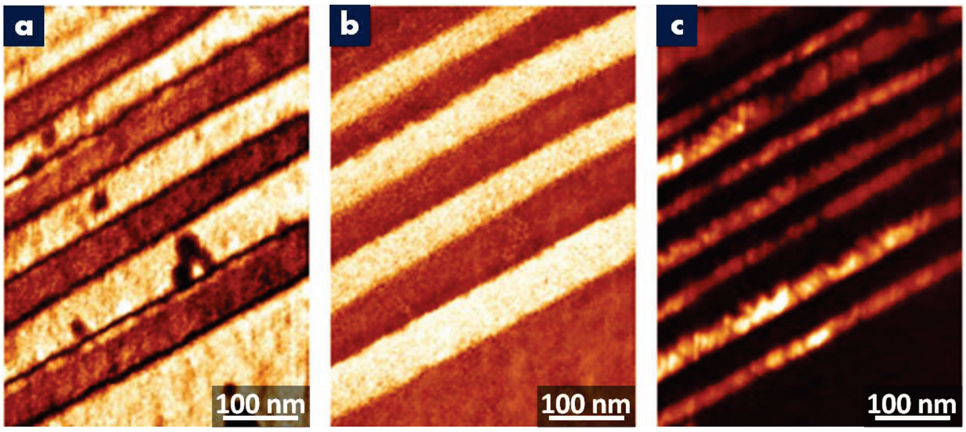

Figure 4.11: PFM and c-AFM images taken simultaneously at 109° domain walls. (a) PFM amplitude and (b) PFM phase images of a BFO sample with 109° stripe domains. (c) simultaneously acquired c-AFM image of the same area showing that each 109° domain wall is electrically conductive.

area, and m_{Pt} and m_{BFO} the effective electron mass in the Pt-coated tip and the BFO.

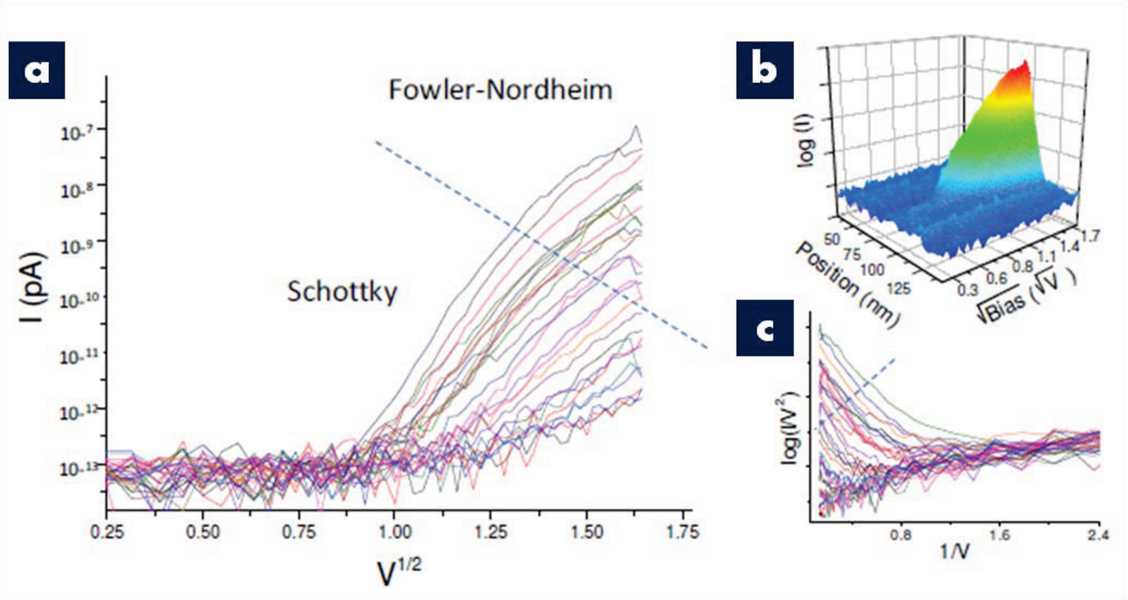

Figure 4.12: a, Several I-V curves measured by stepping the c-AFM tip perpendicular across a domain wall at 340 K. Data plotted in linear coordinates for Schottky emission. b, 3-D plot of such a measurement. c, same data as in Figure 4.12a plotted in linear coordinates for Fowler-Nordheim tunneling.

Figure 4.12 shows local I-V curves acquired with a conductive AFM tip stepping perpendicular to a domain wall at 340 K. All measurements were done with the same force (load) on the tip to get comparable I-V curves. Figure 4.12b gives a visual impression of the local conductivity as a function of position across the wall. For Figure 4.12a and b the data has been plotted in a way that linearizes it within the framework of a Schottky model. Clearly, for lower current an bias values, the data is linear, indicating that Schottky emission is a likely mechanism for the interface limited conduction. For higher currents and biases we see a transition to a significant curvature in the I-V curves. If the same data is plotted in a way that linearizes it for Fowler-Nordheim tunneling, we see that this high current - high bias region follows straight lines (Figure 4.12c). This likely indicates a transition from Schottky emission to Fowler-Nordheim tunneling as the predominant conduction mechanism.

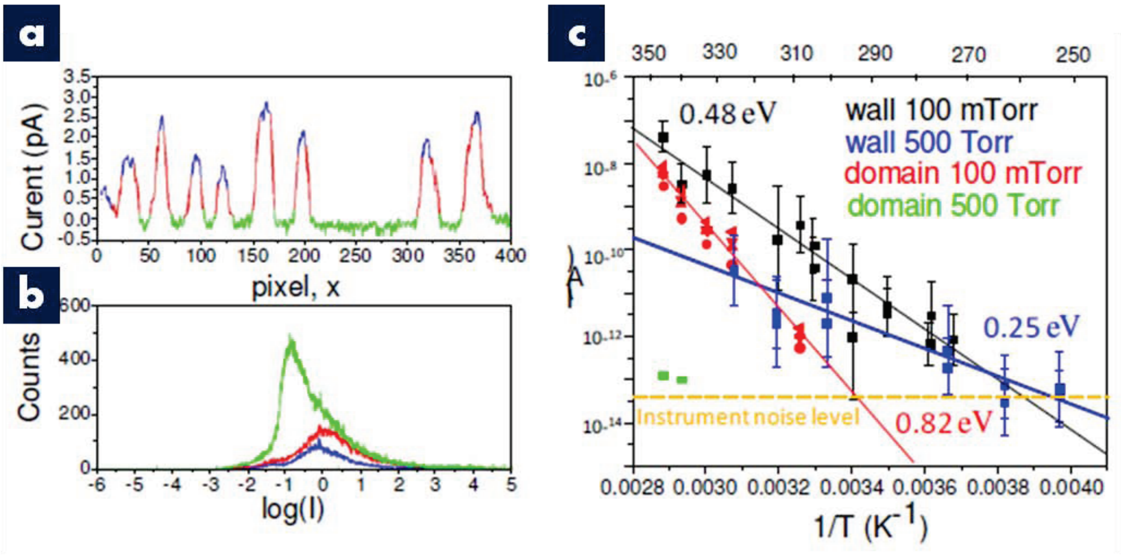

Figure 4.13: a, histogram analysis, saturated peak value (blue), whole peak (red), and whole raw data (green) are extracted. B, typical histograms of log(I). c, Current levels extracted from histogram analysis of c-AFM images at various temperatures and tip biases for the 500 Torr oxygen cooled sample and 100 mTorr oxygen cooled sample. The error ars are FWHM of the correponding histograms. Activation energies are given in the inset.

In order to explain the observed behavior of the measured current, we turn to a detailed analysis of the temperature dependent conduction properties at the domain walls, as it is known that domain wall properties are temperature dependent, e.g. for ferroelastic walls in $LaAlO_3$ [62]. For this we performed histogram analysis of c-AFM images of conducting walls acquired at different temperature (Figure 4.13a). This allows us to extract spatially averaged current values at each temperature and applied voltage. The current histograms are relatively broad, as disorder may originate from the energy distribution of the oxygen vacancy levels, intrinsic variations in the contact potential, and extrinsic variations in the contact area. The dominant origin will strongly depend on the relative contributions of the surface- and bulk-limited conductance. Temperature dependent current values are shown in Figure 4.13c. Activation energies are extracted and shown in the inset.

In all cases, the activation energy for thermally activated transport at the 109° domain walls is extracted to be 0.24-0.5 eV (Figure 4.12a). A possible origin for increased activation energies for the 100 mTorr sample could be clustering of vacancies, which has been reported in other materials such as $SrTiO_3$ [50]. There it was shown that oxygen clustering lowers the energy levels of the oxygen vacancies by about a factor of 2. Another possible scenario is that oxygen vacancies directly influence the structure of the domain wall [50] [63], thus giving rise to a change in transport properties. We note that similar measurements performed off the domain wall on samples cooled in 100 mTorr oxygen (where overall current values are higher, and thus a reasonable temperature range for I-V measurements is accessible) gave consistently higher activation energies of ~0.82 eV (Figure 4.13b).

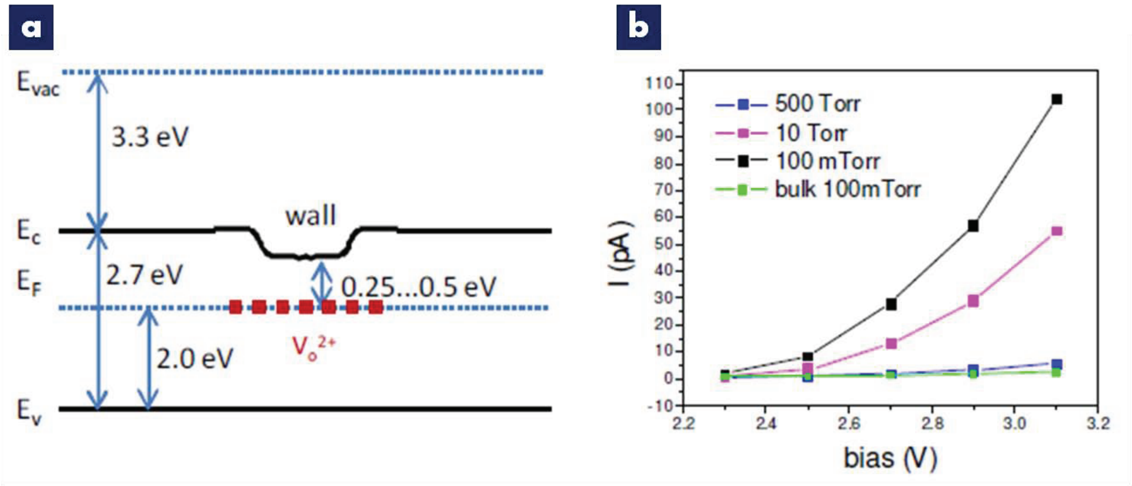

Figure 4.14: Band diagram of 109° domain walls extracted from c-AFM study. (a) Schematic band diagram for the 109° domain wall. (b) Current levels extracted from istogram analysis of c-AFM images at room temperature for samples with different oxygen cooling pressure and thus varying density of oxygen vacancies.

The mechanism of the reported transport in La-doped $BiFeO_3$ can be understood by an electronic conduction mechanism as a consequence of oxygen vacancy activation in an electric field. By taking the band gap value, electron affinity, oxygen vacancy band position and work function of the bulk material and the wall [64] [65] [66] [67]. A schematic of the band structure at the domain wall can be obtained as shown in Figure 4.14a. This model of enhanced conduction at the domain walls, driven by a local change in the band-gap, a potential step across the wall as a defect chemistry is substantiated by the results of experiments in which we deliberately introduced oxygen vacancies into the system by different oxygen cooling pressures during growth. As seen in Figure 4.14b larger concentrations of oxygen vacancies lead to a correspondingly increased current; changing the cooling pressure from 500 Torr to 100 mTorr leads to an increase in current of more than one order of magnitude. Curiously the difference in the activation energy between the domain wall and surface area away from the wall on the 100 mTorr sample is comparable to the predicted lowering of the conduction band edge from DFT calculations (0.2-0.5 V depending on the type of the wall), which may indicate that electrons tunnel or hop from the tip into the conduction band of $BiFeO_3$, the the corresponding lowering of the band-edge is reflected in the measured barrier height.

4.4 Scanning tunneling microscopy study at as-grown domain walls

In this section, we further explore the 109° and 71° domain walls by measuring the local electronic structure using scanning tunneling microscopy (STM) in a cross-sectional geometry. STM and scanning tunneling spectroscopy (STS) studies provide direct experimental insight into the origin and nature of the observed electronic conductivity at the domain walls in BFO with atomic resolution. Tunneling current-voltage characteristics reveal electronic properties at domain walls, involving a decrease in the local band-gap and built-in asymmetrical potential barriers at domain walls as discussed in the previous section.

In this study, $BiFeO_3$/Nb-$SrTiO_3$ samples with 2-D arrays of domain walls were used and cleaved. As discussed in chapter 2, and again schematically illustrated in Figure 4.15a and b, the orientation of 71° domain walls, where the adjacent ferroelectric polarizations changes from $[\bar{1}1\bar{1}]$ direction to $[\overline{111}]$ direction, exhibits a 45° tilt angle with respect to the interfacial boundary of BFO/Nb-STO (pseudocubic (001) plane), as examined in the $(0\bar{1}0)$ cleaved plane. On contrast, the orientation of 109° domain walls, which are between ferroelectric polarizations along $[\bar{1}11]$ and $[\overline{111}]$ directions, are perpendicular to the interfacial boundary of BFO/Nb-STO. These distinct and well-defined differences in domain wall orientations allow us to identify 71° and 109° domain walls easily at the cleaved surfaces. Figure 4.15c,d depicts typical topographic images of the 71° and 109° domain wall in constant current mode, where the distance between the tip and sample was stabilized at scanning parameters of +3.5 V and 1.2 nA. The corresponding electronic structure of the as-grown 71° and 109° domain walls are displayed in Figure 4.15e and f. Combining the topographic images with the corresponding electronic images facilitates the determination of the location of the domain walls.

Maps of the tunneling conductance were recorded simultaneously with the topo-

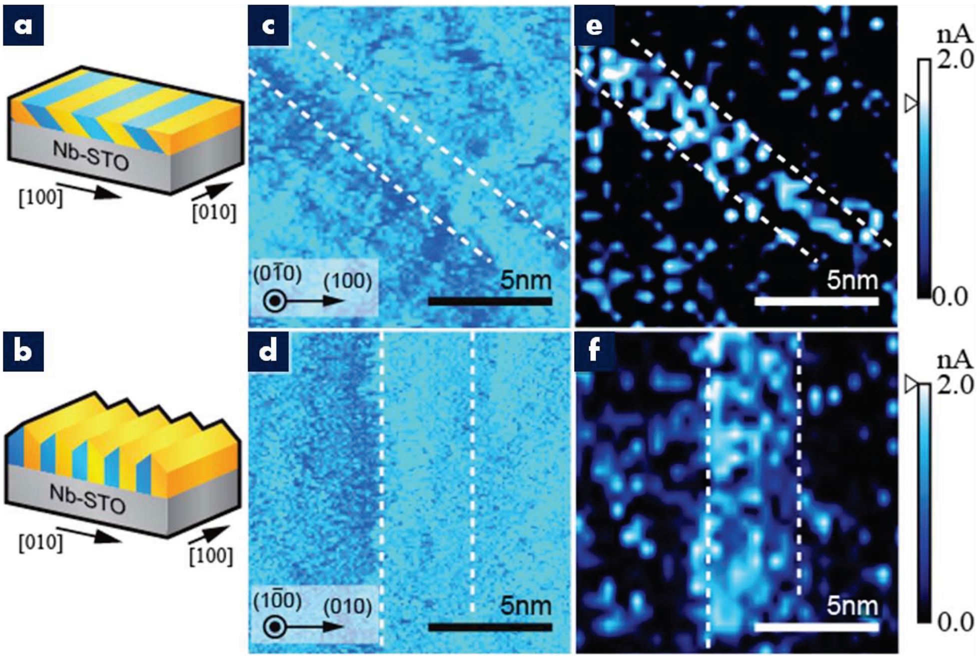

Figure 4.15: (a), (b) Schematics of 2-D arrays of as-grown 71° and 109° domain walls, respectively. (c), (d) Cross-section topographic images of the 71° and 109° domain walls, respectively, taken at a sample bias of -3.50 V. (e), (f) Cross-section electronic structrues images of 71° and 109° domain walls, respectively, taken at a sample bias of +2.00 V.

graphical images by varying the sample bias V_s and acquiring the differential tunneling current (dI/dV) characteristics as a function of the sample bias using lock-in detection. Scanned with fixed lifting height and sample bias, domain walls are imaged as bright bands in the electronic structure images, suggesting higher tunneling conductance comparing to the domain area. Then, spectral analysis of the sequentially layered electronic characteristics across the domain walls (Figure 4.16) provide more insight of the increased tunneling current at the walls. For each spectrum, the feedback loop was turned off and the sample voltage (V_s) was ramped between -3 V and +3 V. Figure 4.16 presents and shows the analysis of several detailed experimental spatial spectroscopic measurements through 71° and 109° domain walls. Several colored solid bars in the atomic-resolution electronic images of the walls in Figure 4.16a and b indicate the spatial positions, and the corresponding spectra are shown in c and d. The resulting tunneling spectra in Figure 4.16c and d are plotted as the differential tunneling current dI/dV as a function of the sample bias across the domain walls. In a band-gap region with zero tunneling current, the approximate locations of valence-band maximum (E_v) and conduction-band minimum (E_c) are extracted and indicated by tick marks in Figure 4.16c and d. The variations in the band structures at different sites along the length of the 109°/71° domain walls attribute to the fluc-

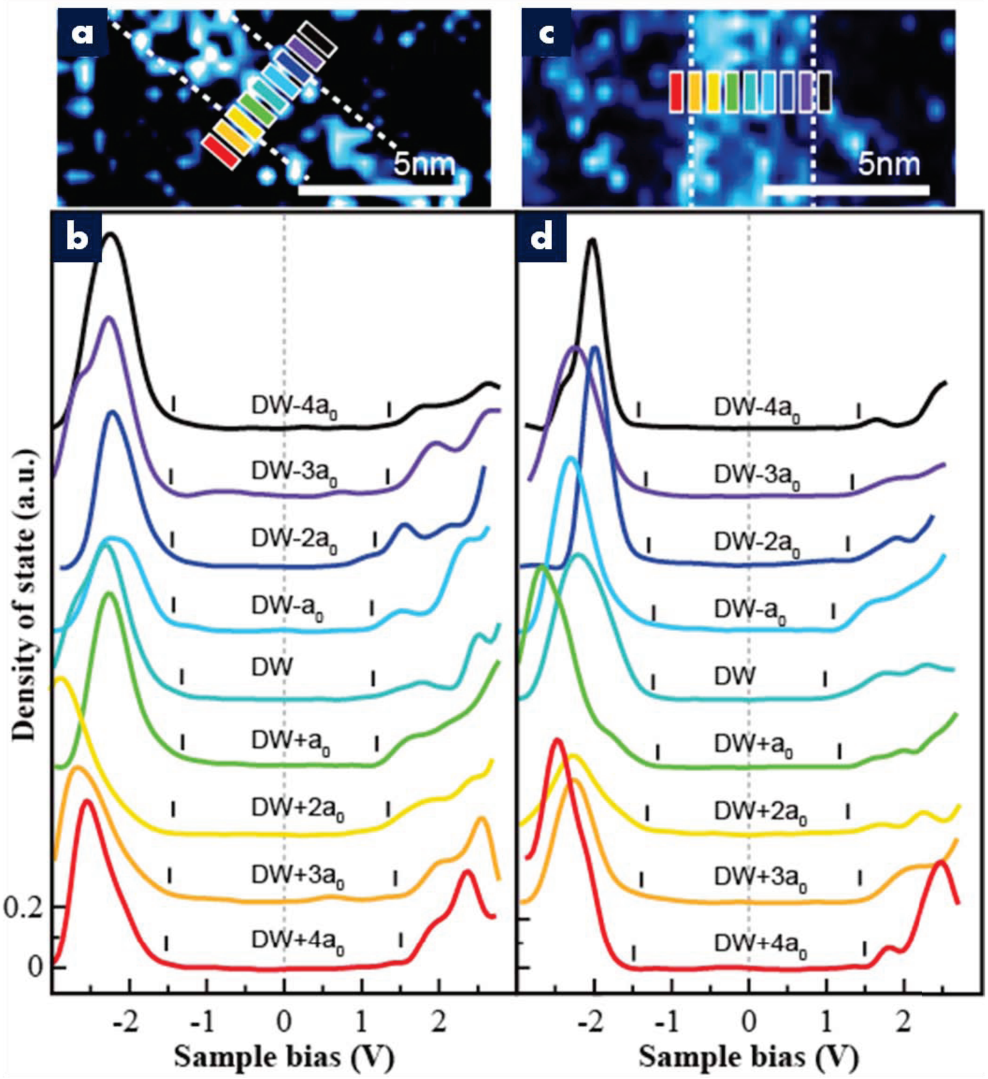

Figure 4.16: Layer-by-layer dI/dV measurements across (a), (c) 71° and (b), (d) 109° domain walls, acquired at ∼110 K. Bars in (a) and (b) denote positions where the electronic spectra are probed, while (c) and (d) show the corresponding spectra within the detection limits. The band edges are indicated by black tick marks in (c) and (d).

tuations in the positions of band edges. Consequently, the variation in the band edge is analyzed from several dI/dV curves on different sites for each domain wall. The uncertainties on each band edge position are ∼0.19 and ∼0.23 eV for 109° and 71° domain walls, respectively.

The fact that conduction can be activated at the domain walls of BFO at room temperature evokes considerations for the changes in band-gap (E_g) across the domain walls. The local layer-by-layer band-gap is extracted from the difference between the

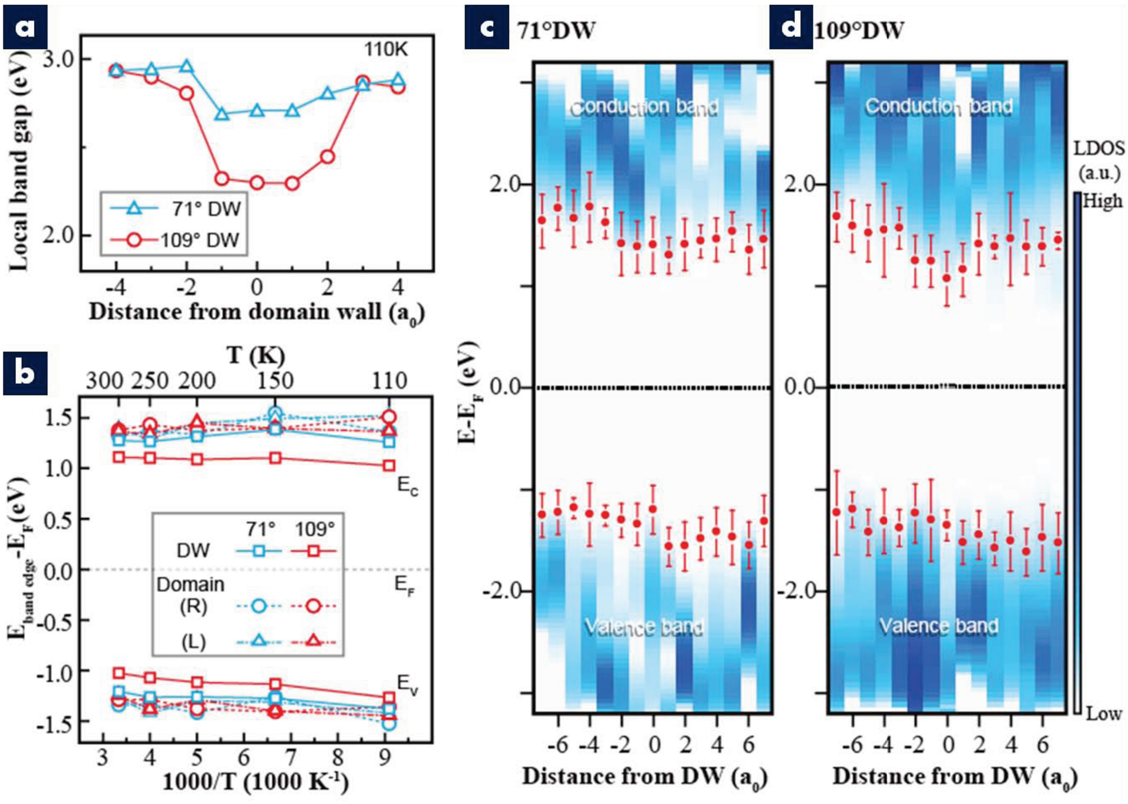

Figure 4.17: Electronic band structures across 71° and 109° domain walls. (a) Local bandgap across 71° and 109° domain walls at ∼110 K. (b) Temperature-dependent band edges change from 110 to 300 K for 71° and 109° domain walls along with domain areas by the right side (R) and left side (L) of the walls. Atomic-scale evolution of band structure across (c) 71° and (d 109° domain walls at ∼110 K. The band edges are indicated by red symbols with error bars in (c) and (d). The black dashed lines represent the Fermi level.

conduction (E_c) and valence band edges (E_v) of electronic characteristics for different domain walls. Figure 4.17a reveals a significant decrease in band gaps at the domain walls from the mid-domain value of ∼2.9 eV at 110 K [66]. The spatial extent of the changes in the local band-gap presents a region of ∼2 nm, consist with the theoretical estimations. [68] It should be noted that the magnitude of the changes in the band-gap depends strongly on the domain-wall type. For the 71° wall, a local band-gap reduction of 0.20 eV, ∼6% decrease from the mid-domain band-gap, is observed. However, the band edge had a marked shift at the 109° domain wall, and its local band-gap is considerably suppressed. According to the present STM measurements, the 109° domain wall has a band-gap of ∼2.4 eV, with a reduction of ∼0.50 eV (∼17%) from the band-gap of the mid-domain region. These STM experimental results show a larger band-gap reduction across domain walls as compared to the theoretically predicted values, e.g., 0.05 eV for 71° domain walls and 0.10 eV for 109° domain walls. [68] [64] This larger reduction of the electronic band-gap across the 109° domain walls is in a better agreement with the experimental results of high electrical conductivity discussed in the previous sections of this chapter.

The changes in the electronic structure due to polarization reorientations could lead to an electrostatic potential step at the domain boundary and there fore influence the local mobility of electron and hold pairs, which is the key factor for the recently observed photovoltaic effect in BFO [69] [70]. Therefore, the immediate question is how the ferroelectric polarization reorientation across the wall influences the electronic properties at the walls. As shown in Figure 4.17b, the temperature-dependent electronic properties in the temperature range of 100-300 K are analyzed. The small temperature dependence of the Fermi level relative to the band edges as shown in this figure implies that the detected free carriers in BFO mainly arise from the intrinsic valence-to-conduction band transitions. In this case, the Fermi level only shifts relative to the band edge in the order of kT (k is the Boltzmann constant and T is the temperature), which is about 0.05 eV in the studied temperature range, and thus these STM results can be considered as intrinsic electronic properties. Consequently, the built-in potential for electrons across the domain walls can be correlated from the variation of the separation between the conduction band and the Fermi level (E_F). Since the measured tunneling current is proportional to the density of the electrons at the semiconductor surface, a smaller band-gap or a smaller separation between the conduction-band edge and the Fermi level imply a larger carrier density. Therefore, a prominent reduction of the band-gap size at 109° domain walls implies that the carrier density of the energy sub-bands near the Fermi level is noteworthy and suggests more electrons accumulate at the 109° domain wall region. In addition, the factor of larger potential difference across 109° domain wall is attributed to the experimental evidence that the 109° domain wall always appears thicker than the 71° domain wall in the electronic STM images in Figure 4.15e and f.

Generally, the offsets of the analyzed layer-by-layer band edges can give insight into the characteristics of the intrinsic carrier density distribution or the electrostatic potential steps across domain walls. With the characteristics of $\mathrm{d}I/\mathrm{d}V$ curves, shown in Figure 4.16, the atomic-scale evolution of local electronic properties across domain walls can be quantitatively depicted and directly traced in Figure 4.17c and d. The key feature observed is that the change of band-gap is mainly attributed to the shift of the conduction band. The significant downward shift in the conduction-band edge can be correlated with the Fe-O octahedral deformations in the wall region [68] [71] [72] [73], leading to the change in Fe-O-Fe band angle and the surroundings of minority-spin Fe $3d$ states at the domain wall. This difference originates from the polarization discontinuity at the walls. The visualized atomic-scale band alignment provides a direct portray of how the band structures evolve across the domain walls. Figure 4.17c and d show that the band edges are asymmetric for domains approaching the 71° and 109° domain walls from different sides. According to the STM measurements, the shift of the conduction-band and valence-band edges for the domains on the two sides of 71° (109°) domain wall are about 0.15 (0.15) eV, which is larger than that found in theoretical estimations [68]. The results observed in STM measurements can be mainly results from the polarization-induced surface potential modification on the ferroelectric domain surface. [61] [74] The magnitude of the modification of the barrier height in the vicinity of the domain wall can also be estimated from realistic parameters in a simple dielectric gap model (polarization P=60μC cm^{-2}, the length of the depletion region $\delta \approx$0.25 nm, and the dielectric constant $\varepsilon \approx$100).

Chapter 5

Magnetotransport at domain walls in $BiFeO_3$

As discussed in Chapter 3, the X-ray spectromicroscopy experiments strongly suggest the existence of an enhanced magnetic moment in the samples with 109° domain walls, likely emanating at the walls themselves. This, coupled with the observation of electrical conduction at the same type of domain walls discussed in Chapter 4, raises an intriguing question: is there a possibility of observing magnetotransport phenomena at such domain walls? This chapter focuses on transport behavior of 109° domain walls measured with a lateral transport device. Moreover, with an application of external magnetic field, details in magnetotransport and the observation of a significant magnetoresistance will be disscussed.

5.1 Lateral transport at domain walls in $BiFeO_3$ films.

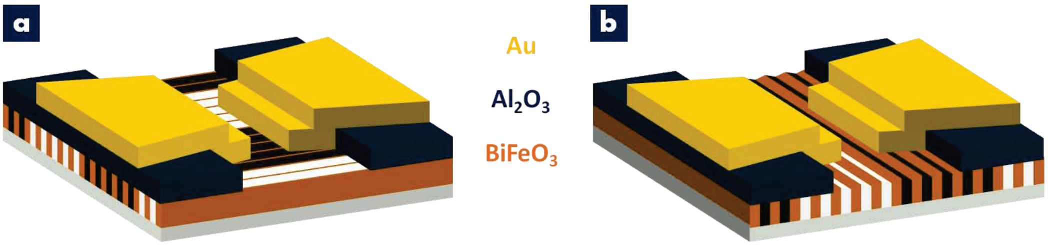

Figure 5.1: Schematics of device structures. (a) An example of current path parallel to the domain walls. (b) An example of current path perpendicular to the domain walls.

Test structures for in-plane transport measurements were fabricated using standard photolithography techniques. Schematically described in Figure 5.1a, in-plane transport structures were fabricated with 150 nm thick Au electrodes separated by 0.75-1.5 μm; 10 nm thick Al_2O_3 was deposited as an insulating layer to limit the current paths. Au electrodes were fabricated in two geometries relative to the domain wall directions, which restrict the current paths parallel (Figure 5.1a) or perpendicular to the domain walls. We typically observe a strong anisotropy of transport (20-50 times) between transport parallel and perpendicular to the domain walls (Figure 5.2). I-V curves for test structures with 50 μm and 20 μm contact lengths are shown in Figure 5.2 in red and pink, respectively, and illustrate the scaling of the total current with the number of domain walls included in the transport path. With the electrode pair restricted to be perpendicular to the domain walls, we consistently observe higher resistances. In contrast, similar devices constructed on 71° domain wall samples exhibit isotropic transport and resistivity between the electrodes in the two orthogonal contact geometries. Therefore, we conclude that the 109° domain walls, that are much less resistive than the domain are, are the main current paths connecting the in-plane electrodes.

We then proceeded to map out the temperature (4-300 K) dependence of transport with the current transport along the 109° domain walls. When the Current-Temperature (I-T) data is plotted on a log scale (Figure 5.3a), two distinct regimes are observed. In the high temperature regime (i.e., >200 K), the transport can be described by a thermally activated behavior as shown in Figure 5.3b for several constant voltage sweeps. By doing the a linear fit with the following equation,

$$I = I_0 \cdot e^{-\Delta E/k_B T} \tag{5.1}$$

The thermal activation energy can be extracted as ~0.25 eV. This transition in transport behavior at ~200 K is intriguing, particularly since phase transitions in BFO

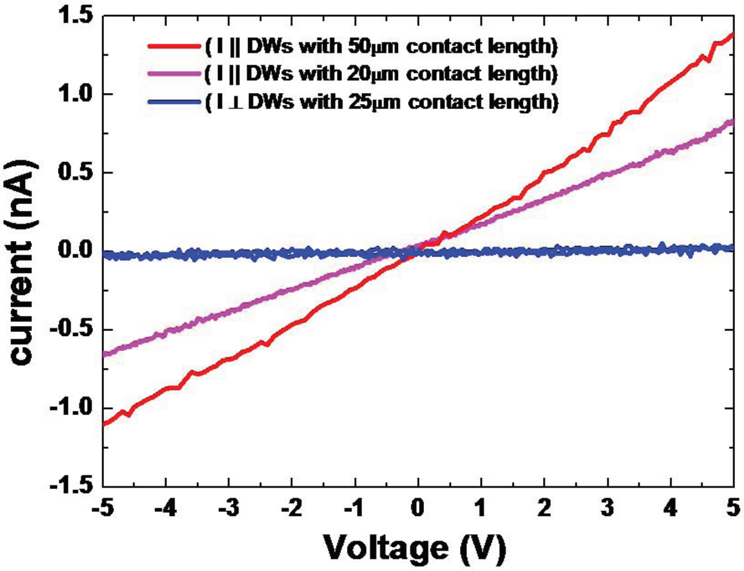

Figure 5.2: I-V curves of 109° domain walls with different electrode geometries. Blue curve corresponds to the current path perpendicular to the 109° domain walls with 25 μm contact length. Red and pink curves correspond to the transport along the 109° domain walls with contact length of 20 μm and 50 μm, respectively.

near 200 K have been observed in other work. [75] The activation energy of ~0.25 eV observed from the fits of the experimental data (Figure 5.13b) is in close agreement with atomic force microscopy based measurements of thermally activated transport in such wall, which is in detail discussed in the previous chapter. This activation energy is also consistent with recent calculations of oxygen vacancy trap states in BFO [76], suggesting that this thermally activated component is arising from detrapping of carriers from oxygen vacancies. At temperatures below 200 K, the transport behavior is better described by a variable range hopping (VRH) model [77] (Figure 5.3c) with the following equation

$$I = I_0 \cdot e^{-(T_0/T)^{1/(d+1)}} \tag{5.2}$$

The dimensionality of the VRH process, d, can be estimated from the fits to the experimental data. As shown in Figure 5.3d, d values of 0, 1, 2, and 3 have been applied as fitting parameter illustrated by colored curves. Our data agrees well with both a 2-D (i.e., d=2) as well as a 3-D (i.e., d=3) transport behavior. In contrast, the data cannot be fitted to a classical thermally activated transport process (i.e., d=0) or for a 1-D (i.e., d=1) VRH model. We note that variable range hopping is commonly observed in doped oxides [77] and specifically has been identified as the low-temperature conduction mechanism in other trivalent iron oxides, such as α-Fe_2O_3 and γ-Fe_2O_3 [78] [79].

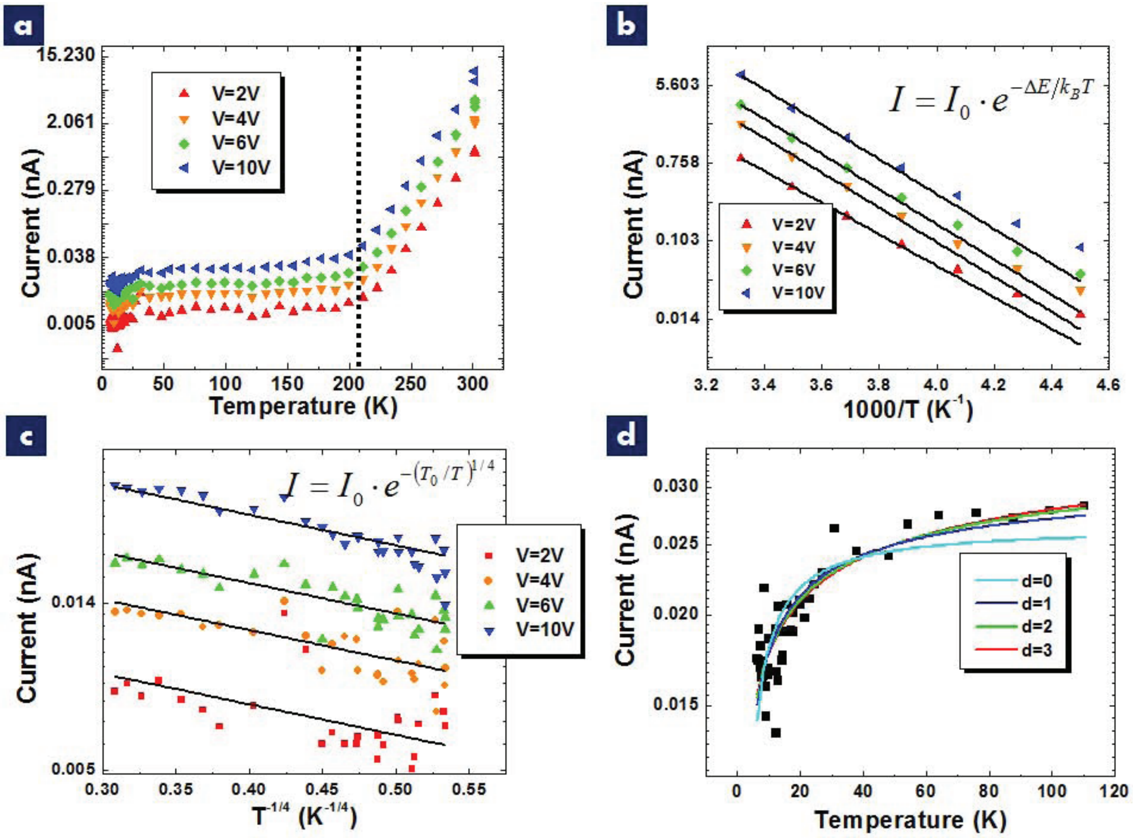

Figure 5.3: Temperature dependent transport study on 109° domain wall samples. (a) Current-Temperature (I-T) curves with various voltage bias. (b) I-T curves above 200 K with thermal activation fitting. (c) I-T curves below 160 K with variable range hopping fitting (d=3). (d) Fitting of I-T curves of transport along 109° domain walls based on variable range hopping model with linear temperature axis. The fitting curves correspond to different d value are shown in different colors.

5.2 Magnetotransport at domain walls in BiFeO$_3$ films.

We next turn to the magnetic field dependence of the transport behavior, which revealed several intriguing aspects. First, all the samples exhibited a marked negative magnetoresistance (MR) when both magnetic field and transport were parallel to the domain walls (black curves, Figure 5.4b; device geometry shown as Figure 5.4a with magnetic field applied along red arrow). Negative MR values as high as ~60% were obtained at a magnetic field of 7 T. Strikingly when the magnetic field was applied perpendicular to the transport path [both in-plane (green arrow in Figure 5.4a and green curve in Figure 5.4b) and out-of-plane (blue arrow in Figure 5.4a and blue curve

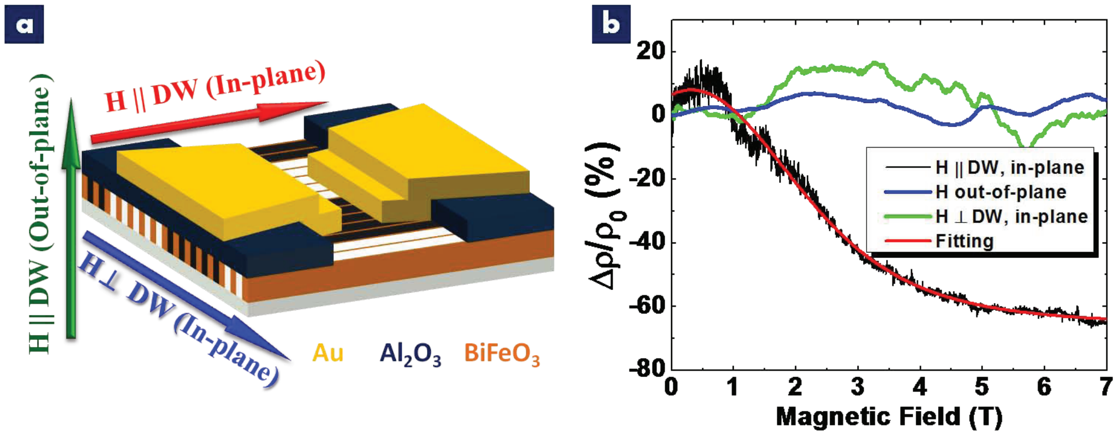

Figure 5.4: Magnetotransport study on 109° domain wall samples. (a) A schematic illustrates the directions of the applied magnetic field with the transport device geometry that constrains the current path along the 109° domain walls. (b) Anisotropic magnetoresistance in different directions of external magnetic field as illustrated in (a) at a temperature of 30 K.

in Figure 5.4b)] or when the transport is perpendicular to the walls, very little MR is observed, indicating that the MR is directly related to the preferential transport parallel to the walls. Then, resistance-temperature curves of a similar device have also been measured under two different magnetic fields, 0 T and 8 T (blue and red curves in Figure 5.5, respectively). As shown in this plot, the MR effect only shows up when the temperature is lower than the transition temperature (200 K), which strongly suggests that the magnetic interaction in electron hopping process is the key factor that causes the observation of significant MR. Moreover, when we go lower in temperature (lower than 40 K), the magnitude of MR effect gets significantly larger, from ~20% at 100 K to ~50% at ~10 K.

In order to understand the microscopic origins of the MR behavior, we first describe the intrinsic magnetic order within the two domains on either side of the domain wall (Figure 5.6). Several pervious experimental studies have shown that the spin spiral in the bulk of BFO is broken when it is grown as a thin film [40]. Further, the degeneracy of the easy plane of magnetization (i.e., {111} in the bulk) is also broken due to the epitaxial strain that is imposed, leading to the formation of an antiferromagnetic easy axis along $\langle 11\bar{2} \rangle$ with the ferroelectric polarization along $\langle 111 \rangle$ axis [80]. As shown schematically in Figure 5.6, with the domain wall formed in a (100) plane, the domain areas (left and right cubes) have ferroelectric polarizations (blue arrow in left cube and orange arrow in right cube) pointing along $\langle \overline{111} \rangle$ and $\langle \bar{1}11 \rangle$ and antiferromagnetic easy axes (green arrows) pointing along $\langle \overline{11}2 \rangle$ and $\langle 1\bar{1}2 \rangle$,

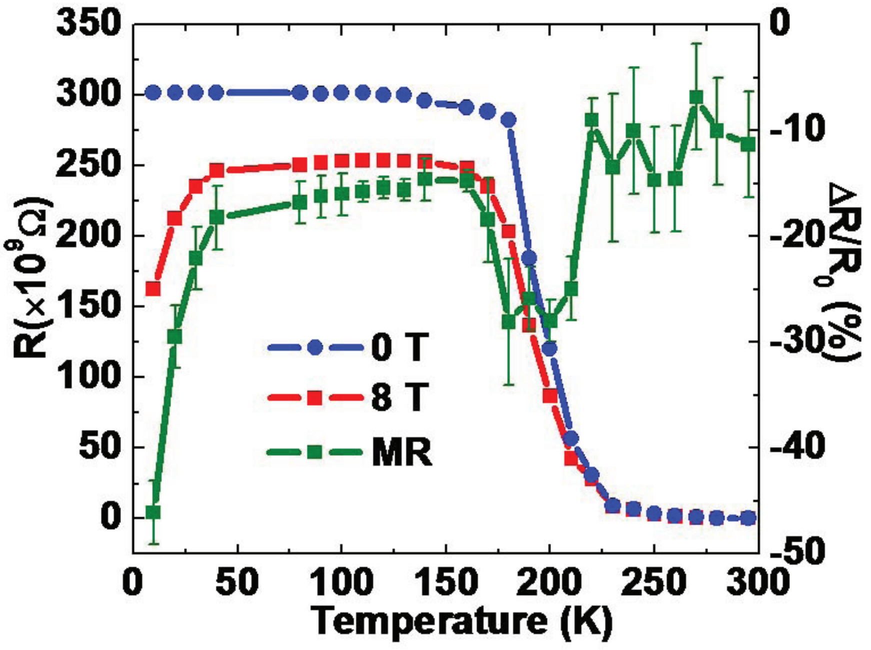

Figure 5.5: Resistance-temperature curves at two different external magnetic fields showing in red (8 T) and blue (0 T). The corresponding magnetoresistance is shown in green.

respectively. The key question is this: what happens to the antiferromagnetic easy axis as one approaches the domain wall from either side? The simplistic perspective is to assume that the antiferromagnetic easy axis rotates smoothly from one domain to the other; specifically, at the wall, the antiferromagnetic easy axis tracks the angular bisector (green arrow in the middle cube) of the easy axes in the adjacent domains, i.e., it lies along the $\langle 0\bar{1}2\rangle$ direction which is in the domain wall plane. Here, the spin rotation process across the domain wall costs exchange interaction energy between neighbor spins, but gain magnetic anisotropy energy by not rotating too far from the antiferromagnetic easy axes. However, another possible spin arrangement consists of sacrificing the magnetic anisotropy energy and the spins are lying along the common line of blue and orange easy plane (red arrows) in Figure 5.6. Moreover, if we only consider the strain effect at the center of the domain wall, [001] direction (yellow arrow in the middle cube, which has its ferroelectric polarization pointing in [100] direction [64] [68]) becomes its favorable antiferromagnetic easy axis in the domain wall. Since these three (twelve, counting the 4-fold symmetry along [100]) possible directions are calculated to have energies very closed to each other, the antiferromagnetic easy axes will have twelve possibilities in the domain wall, which results in twelve possible orientations for the canted moment that is always perpendicular to them. This schematic, in the light of the PEEM studies in the previous chapters, strongly suggests the possibility of a preferred axis of magnetization parallel to the wall surface (along [010] in the case of Figure 5.6). With this as the framework, we now address the possible origins of the MR behavior.

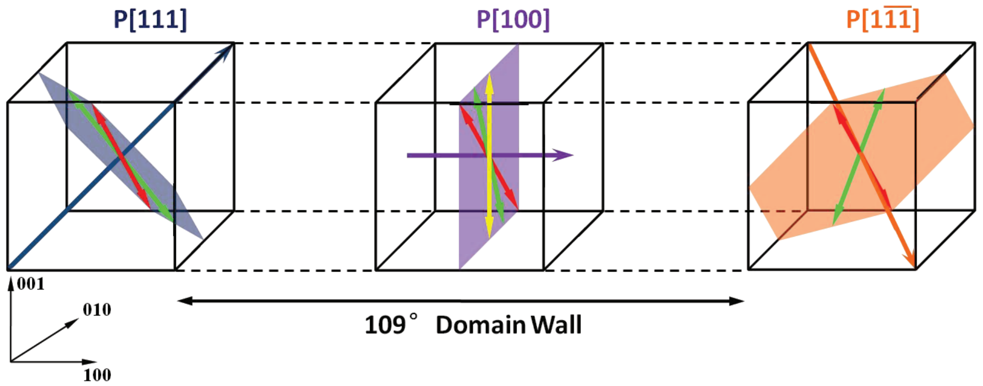

Figure 5.6: Schematic of ferroelectric polarization and the evolution of antiferromagnetic easy axis within one single domain wall with the domain wall plane in (100).

Our model for the observed MR is based on a modification of the hopping process between spin-clusters in an external magnetic field. [81] Before the application of a magnetic field, the effective moments of each cluster are randomly directed (while the canted moments are aligned in one direction within each spin cluster). With an applied magnetic field, the canted moments of all the spin clusters begin to align along the field direction, and the negative magnetoresistance can be described as a result of reduced resistivity arising from this stronger degree of spin alignment.

The resistivity of this system can be separated into two parts: spin-related resistivity, ρ_s, and spin-unrelated resistivity, ρ_{ns}. Then the total resistivity of the system can be described as

$$\rho = \rho_s + \rho_{ns} \tag{5.3}$$

Since ρ_{ns} is a constant with the application of external magnetic field B, the magnetoresistance of this system can be written as

$$\begin{aligned}\frac{\rho(B)-\rho(0)}{\rho(0)} &= \frac{\rho_s(B)+\rho_{ns}-\rho_s(0)-\rho_{ns}}{\rho_s(0)+\rho_{ns}} \\ &= \frac{\rho_s(B)+\rho_s(0)}{\rho_s(0)+\rho_{ns}} \\ &= \left(1+\frac{\rho_{ns}}{\rho_s(0)}\right)^{-1}\cdot\frac{\rho_s(B)-\rho_s(0)}{\rho_s(0)} \\ &= A\cdot\frac{\rho_s(B)-\rho_s(0)}{\rho_s(0)} \qquad (5.4)\end{aligned}$$

where A is a constant.

With the application of magnetic field, the hopping barrier W that emerges from the VRH model can be modified by adding an extra term ΔW that is related to the misorientations of the magnetic moments. Then, the current can be written as

$$I = I_0\cdot\exp\left\{-\frac{\Delta W}{k_BT}\right\} \qquad (5.5)$$

where $\Delta W = \alpha M^2$, and M is the net magnetization of the system generated by the external magnetic field. Considering the spin-clusters as superparamagnet, M is related to the external field B through the Langevin function:

$$M = L\left(\frac{\mu B}{k_BT}\right) \qquad (5.6)$$

where $L(x)=\coth(x)-1/x$.

Then the transport current $I(B)$ can be described as follows with applied external magnetic field B:

$$I(B) = I_0\cdot\exp\left\{-\frac{\alpha(L(x))^2}{k_BT}\right\} = I_0\cdot\exp\left\{C\cdot(L(x))^2\right\} \qquad (5.7)$$

where $x=\dfrac{\mu B}{k_BT}$, and constant $C=-\dfrac{\alpha}{k_BT}$

Then the spin-related magnetoresistance can be written as

$$\begin{aligned}\frac{\rho_s(B)-\rho_s(0)}{\rho_s(0)} &= \frac{\rho_s(B)}{\rho_s(0)}-1 \\ &= \frac{V/I(B)}{V/I_0}-1 \\ &= \frac{I_0}{I(B)}-1 \\ &= \exp\left\{-C\cdot(L(x))^2\right\}-1 \qquad (5.8)\end{aligned}$$

Therefore, the total magnetoresistance can be calculated as

$$\begin{aligned}\frac{\rho\left(B\right)-\rho\left(0\right)}{\rho\left(0\right)}&=A\cdot\frac{\rho_s\left(B\right)-\rho_s\left(0\right)}{\rho_s\left(0\right)}\\&=A\cdot\left\{\exp\left\{-C\cdot\left(L\left(x\right)\right)^2\right\}-1\right\}\end{aligned}\qquad(5.9)$$

where $x=\dfrac{\mu B}{k_BT}$. Constants A, C, and $\dfrac{\mu}{k_BT}$ are extracted from fitting the experimental data. The corresponding fit is shown in Figure 5.4b (red curve), which is reasonably close at a qualitative level. From the fit, we were able to extract the magnitude of $\dfrac{\mu}{k_BT}$ in the Langevin function as equal to 0.5 T^{-1}, which provides insight into the average moment (and therefore size) of the spin clusters. For example, using a measurement temperature of 30 K, we calculate a cluster moment of $\sim 22\mu_B$. The physical size of the cluster then depends on the magnitude of the canted moment within the walls. A lower bound for the canted moment is the bulk value of $\sim 0.03\mu_B$; another bound for the canted moment can be estimated from the resolution limit of the PEEM, which is typically $\sim 0.1\mu_B$. Under these boundary conditions, the spin cluster size is in the range of ~200-550 unit cells in volume (where each unit cell is $\sim 4\times 4\times 4$ Å^3). Using a wall width of 3-5 unit cells (obtained from the atomic resolution TEM images shown in Chapter 3, Figure 3.1), the lateral size of the spin cluster is estimated to be ~8-14 unit cells (i.e., 3-6 nm).

In summary, we have systematically studied the nature of magnetism in BFO thin films possessing 71° and 109° ferroelectric domain walls. We observe enhanced magnetic moments in samples with ordered arrays of 109° domain walls, while samples with ordered arrays of 71° domain walls show no such enhanced magnetic moment. This enhancement correlates to the repeatable observation of an exchange bias in samples that are comprised predominantly or such 109° domain walls. Macroscopic theoretical analyses also point to the emergence of an enhanced magnetic moment at the walls; the details of the nature of magnetism (i.e., ferromagnetic, spin glass, etc.) as well as the magnitude of the moments sill need further detailed sutdies. On a microscopic basis, such an enhancement could be attributed to the symmetry change at 109° domain walls leading to an increase of the canting angle between neighboring Fe spins. [68] The nature of the antiferromagnetic domain wall (i.e., its width, the magnitude of the local magnetic moment within the wall) as well as the strength of the coupling between the ferroelectric and antiferromagnetic walls in BFO area issues that still need to be resolved both from a theoretical and experimental perspective. We note that the interaction between ferroelectric and antiferromagnetic domain walls has been studied in model multiferroics such as $\mathrm{YMnO_3}$ and $\mathrm{BiFeO_3}$. In both cases it has been shown that the antiferromagnetic domain walls are significantly wider (by ~1-2 orders of magnitude) compared to the ferroelectric walls. [43] [44] It is quite likely that the enhanced strain as well as the more complex domain wall topology is likely to further enhanced the possibility of obtaining larger moments at the domain walls. However, this very complexity is also likely to give a large variability in the observed magnetic moments as has been observed in the case of films grown on $SrTiO_3$ substrates. By far, the most interesting aspect of the research presented in this paper is the large MR behavior at such walls; clearly, the limits of this behavior need to be determined with further work.

Chapter 6

Mixed phase structure in $BiFeO_3$ epitaxial films

In the previous chapters, the domain walls have been discussed as one special kind of interface which show interesting properties, such as enhanced magnetization, conduction and large magnetoresistance while the bulk material is a antiferromagnet with very small canted moment and robust ferroelectric insulator. This chapter focuses on another interesting system, rhombohedral-like and tetragonal-like mixed-phase $BiFeO_3$ film, where both of its interfaces (phase boundaries) and each individual phase may show intriguing phenomena because of the discontinuity of the order parameters and large constraints between adjacent phases. Although the smooth and gradual transition (details in the Section 6.1) between the rhombohedral-like and tetragonal-like phases makes the discontinuity of the order parameters unobvious and the properties of the phase boundaries hard to observe, the large constraints between adjacent phases also bring new properties and functionalities to each individual phase, especially an electrically controllable largely enhanced magnetization observed in the highly distorted rhombohedral-like phase, which will be discuss in detail in this chapter.

Modern functional materials, for example ferromagnets and piezoelectrics, are typically chemically complex and exhibit the coexistence of multiple phases that evolve as a consequence of chemical alloying [82]. In such materials, huge responses to external stimuli are often found at phase boundaries. In the past two decades, examples of the discovery of such behavior include the emergence of colossal magnetoresistance in doped manganites, high-temperature superconductivity in doped cuprates, and large piezoelectric responses in relaxor ferroelectrics [83]. The large piezoelectric coefficients in $Pb(Zr_x,Ti_{1-x})O_3$ (PZT), $Pb(Mg_{0.33},Nb_{0.67})O_3$-$PbTiO_3$ (PMN-PT), and $Pb(Zn_{0.33},Nb_{0.67})O_3$-$PbTiO_3$ (PZN-PT) systems, for example, occur in compositions that lie at the boundary between two crystal structures, for example, a rhombohedral-to-tetragonal phase boundary [84] [85] [86] [87]. These giant piezoelectric responses have made PZT, PMN-PT, and PZN-PT the materials of choice for a variety of applications ranging from micropositioners to acoustic sensing in sonar. Notwithstanding the dramatic progress in the development of functional piezoelectric devices from these lead-based perovskites, two broad questions remain: (i) are there lead-free alternatives to the above-mentioned systems, and (ii) are there viable alternative pathways that are fundamentally different from the chemical alloying approaches (such as that seen in the PZT and PMN-PT systems) to achieve large piezoelectric responses? In this chapter, it will be discussed that epitaxial strain can be used to drive the formation of a phase boundary and create large piezoelectric responses in lead-free ferroelectric materials, as well as, enhanced magnetization in this mixed-phase system. This phase boundary was first understood as morphotropic phase boundary; however, with deeper understanding in later experiments, this phase boundary is now understood as isostructural (or, isosymmetric) phase boundary at room temperature, and transforming into morphotropic phase boundary above 200 °C.

6.1 Structure of Mixed Phase $BiFeO_3$ System

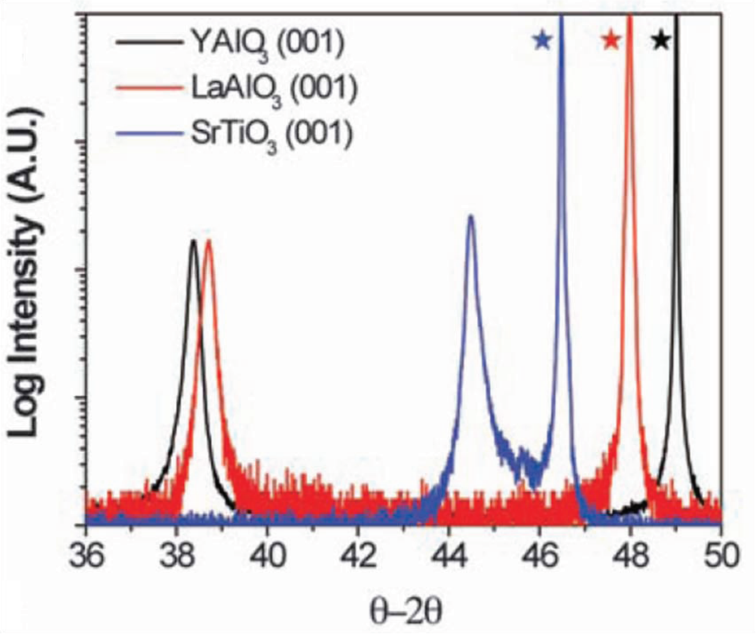

Figure 6.1: X-ray diffraction of the pseudocubic 002-diffraction peak of BFO/STO (001), BFO/LAO (001), and BFO/YAO (110) shows the presence of a long-axis T phase on both LAO and YAO substrates. Substrate peaks are marked with a star.

In this section, we are going to discuss the evolution of structural change between different phases in this isostructural mixed-phase BFO system. BFO is a multiferroic perovskite that exhibits antiferromagnetism coupled with ferroelectric order [3] [4]. The structural stability of the parent rhombohedral phase of this material has been the focus of a number of theoretical studies [88] [55]. In its bulk form, BFO occurs in the $R3c$ space group but it is often studied in the form of thin films where it is subject to an epitaxial constraint. Such constraints impose coherency and strain that, in general, distort the bulk structure and/or stabilize phases not present in the bulk material. Although the parent ground state in thin films is a monoclinic-distorted rhombohedral (Cc), a monoclinic-distorted tetragonal phase (Cc space group, with in-plane lattice parameter $a \sim 3.665$ Å and out-of-plane lattice parameter $c \sim 4.655$ Å) with a large spontaneous polarization has been identified [88] [89] [90]. We use the "T" notation in reference to a parent monoclinic-distorted tetragonal phase that has a c axis lattice parameter of ~ 4.65 Å. Similarly, we use the "R" notation in reference to a monoclinic-distorted rhombohedral parent phase that has a c axis lattice parameter of ~ 4.0 Å. It has been established that the strain is particularly effective in altering the stable crystal structure of thin films where strains of several percent can be imparted through commensurate epitaxial growth on an underlying substrate [91]. We show that epitaxial strain can be used to stabilize the T phase of BFO and that intermediate strains position BFO on a isostructural phase transition between its T and R phases. After establishing the characteristics of the pure T phase, we show that the T and R phases can coexist on a length scale of tens of nanometers in films grown with intermediate strain and have huge piezoelectric responses.

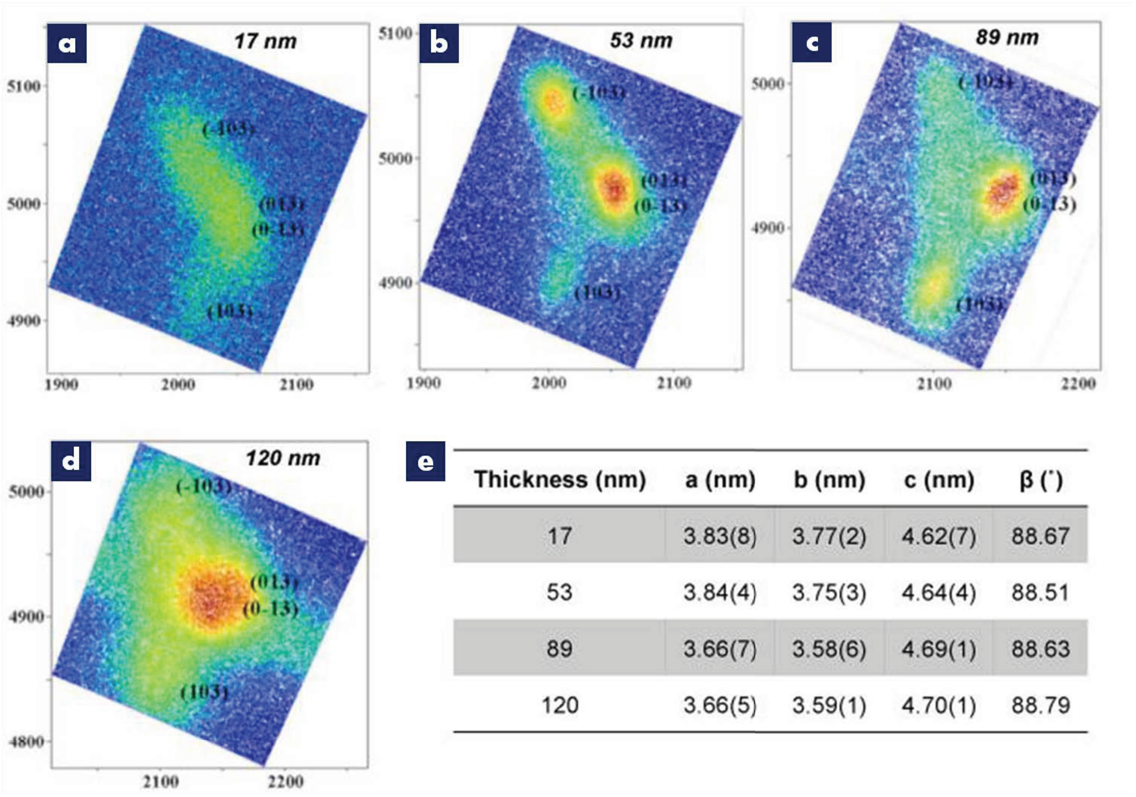

Thickness (nm)	a (nm)	b (nm)	c (nm)	β (˚)
17	3.83(8)	3.77(2)	4.62(7)	88.67
53	3.84(4)	3.75(3)	4.64(4)	88.51
89	3.66(7)	3.58(6)	4.69(1)	88.63
120	3.66(5)	3.59(1)	4.70(1)	88.79

Figure 6.2: Reciprocal space maps of the 103 and 013 diffraction peaks of the T phase BFO in (a) 17 nm, (b) 53 nm, (c) 89 nm, and (d) 120 nm thick films. The x and y axes are Q_x×10000 (r.l.u) and Q_y×10000 (r.l.u) respectively. The table in (e) summarizes the structure of the various unit cells based on these detailed X-ray diffraction studies.

We grew epitaxial BFO films using conventional molecular beam epitaxy (MBE) and laser-MBE on single-crystal substrates of (001) $LaAlO_3$ (LAO) (rhombohedral with a pseudocubic lattice parameter a=3.79 Å) and (110) $YAlO_3$ (YAO) (orthorhombic with a pseudocubic lattice parameter a=3.69 Å). Reference rhombohedral phase of BFO were grown on (001) $SrTiO_3$ (STO) (cubic with lattice parameter a=3.905 Å) substrates. For electrical and piezoresponse force microscopy (PFM) studies only, a 3- to 50-nm layer of epitaxial $La_{0.5}Sr_{0.5}CoO_3$ (LSCO) (a=3.82 Å) , $La_{0.7}Sr_{0.3}MnO_3$ (LSMO) (a=3.85 Å), or $LaNiO_3$ (LNO) (a=3.84 Å) was used as a bottom electrode.

Detailed structural characterization was completed by a combination of X-ray diffraction, reciprocal space mapping, and scanning transmission electron microscopy based atomic imaging (TEAM 0.5 at the National Center for Electron Microscopy). Ferroelectric domains were imaged and switched using PFM as described in previous chapters. Local surface displacements were measured using high-resolution atomic force microscopy (AFM) as a function of applied DC field.

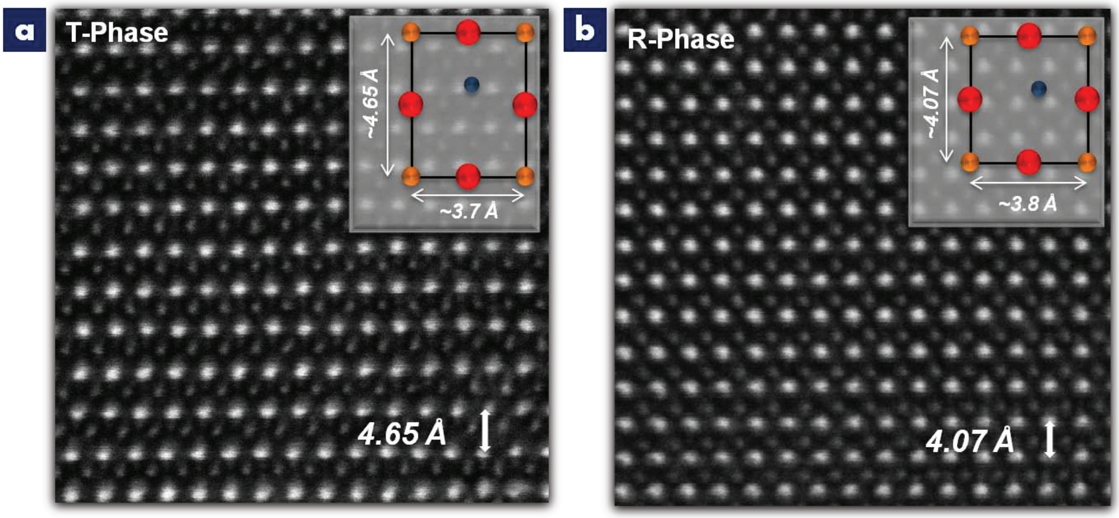

Figure 6.3: Atomic resolution STEM images of the T phase (a) and the R phase (b),respectively. Insets show schematic illustration of the unit cell.

These measurements of the structural aspects of the T phase and its evolution with thickness were completed without a bottom electrode in order to understand the direct influence of epitaxial constraint on the direct influence of epitaxial constraint on the phase evolution. Figure 6.1 shows a typical $\theta - 2\theta$ scan of BFO films grown on LAO, YAO, and STO substrates. The films grown on the reference STO substrate show the same monoclinically distorted rhombohedral structure that is established in the literature [92] [93] [94] [95]. In contrast, the films grown on LAO and YAO exhibit strong reflections at 2θ values corresponding to an out-of-plane lattice parameter of $\sim$ 4.65 Å. Detailed reciprocal space mapping scans as a function of film thickness reveal a number of interesting aspects. First, for thinner films on LAO substrates (less than $\sim$50 nm), we measure the in-plane lattice parameters to be a $\sim$3.84 Å and b $\sim$3.76 Å, respectively. (See Figure 6.2 for reciprocal space map data used to determine these lattice constants.) Second, we observe a monoclinic tilt of the structure with $\beta \sim 88.6°$. On the other hand, for thicker films (>50 nm) we observe the coexistence of the two phases. The insets of Figure 6.3a and b schematically describe the T and R phases.

The atomic structure of these two phases was imaged directly using the TEAM

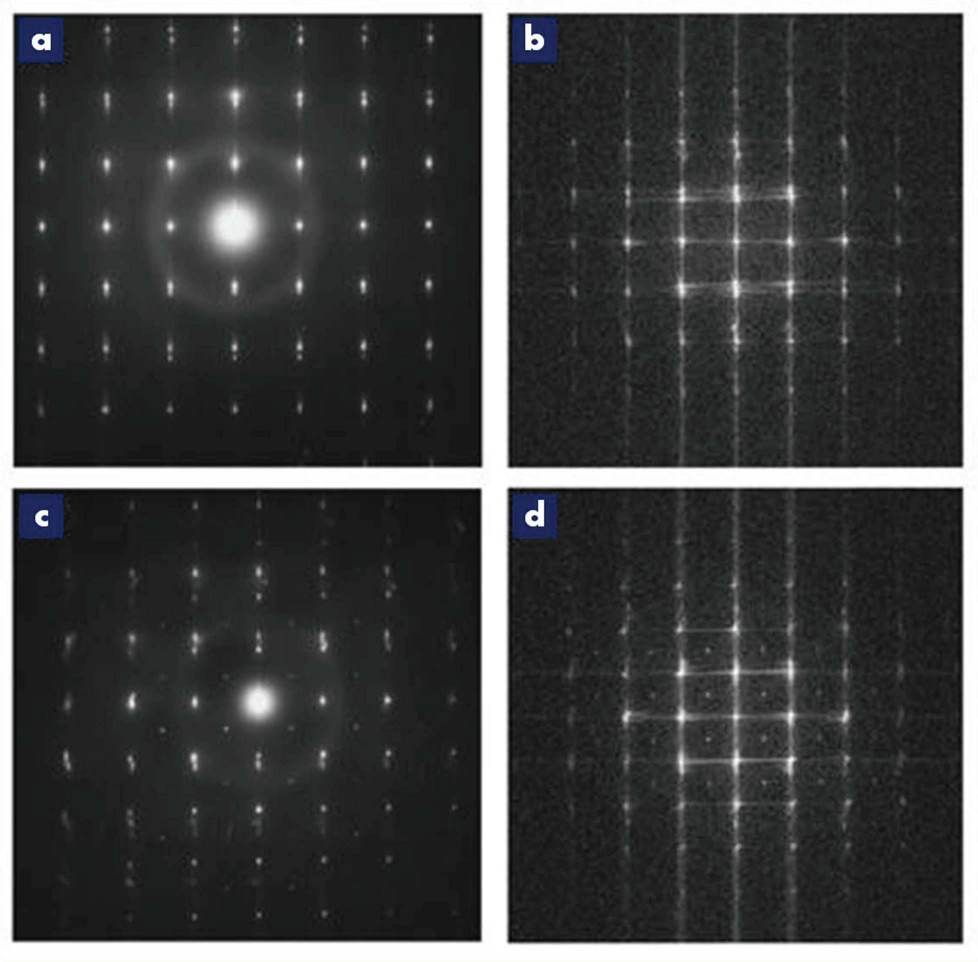

Figure 6.4: Electron diffraction patterns and Fourier transforms, respectively, for R phase BFO (a and b) and T phase BFO (c and d), which correspond to Figure 6.3b and a, reveal distinct differences in symmetry.

0.5 transmission electron microscope. Atomic resolution high-angle annular dark-field scanning transmission electron microscopy (HAADF-STEM) images, also referred to as Z-contrast images, of these two different phases are shown in Figure 6.3a and b, respectively. Both images were acquired along the perovskite pseudocubic direction and exhibit atomic columns with two distinct intensities, with the Bi atom columns appearing brighter than the Fe atom columns. The strong atomic-number contrast of HAADF-STEM prevents the observation of the oxygen atomic columns next to the cation-containing columns. It is interesting to note that the small size of the aberration-corrected electron probe (∼0.6 Å) used for the HAADF-STEM imaging and the high mechanical and electrical stability of the microscope employed allowed for resolving the displacement of the Fe atoms from the center of the unit cell defined by Bi rectangles. The electron diffraction patterns and the Fourier transforms in Figure 6.4, obtained from the images in Figure 6.3, reveal clear differences between the symmetries of the T and R phases.

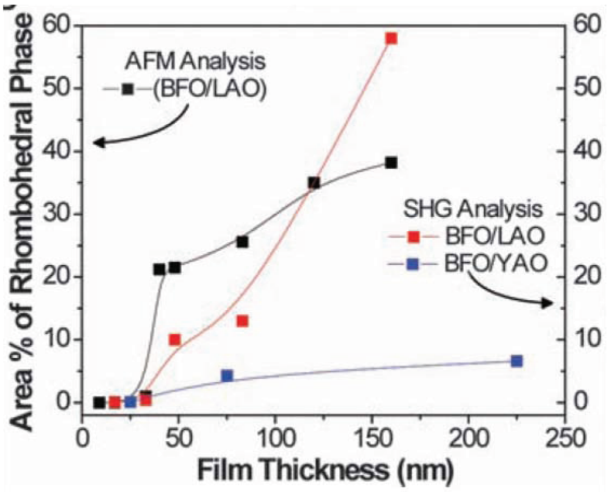

Figure 6.5: The evolution of the structure with thickness, including the area fraction (left axis and the volume fraction of the R phase.)

As the films are made thicker, we observe the mergence of the R phase that coexists with the T phase. The relative areal and volume fractions of these two phases as a function of film thickness are shown for films on both LAO and YAO substrates in Figure 6.5. Areal fractions were calculated from detailed high-resolution AFM studies of the surface, shown in Figure 6.6, while second harmonic generation (SHG) studies (described in the following paragraph) shown in Figure 6.7 gives volumetric fractions. As expected, in the case of films grown on YAO (the substrate with the smallest lattice mismatch with the T phase), we observe that the film remains essentially tetragonal-like for the range of thinknesses studied. In contrast, films grown on LAO show a distinct evolution of the phase mixture due to relaxation of the epitaxial strain with increased thickness.

Optical second harmonic generation (SHG) was employed to structurally differentiate between the films and estimate the increase in R phase with film thinkness. Fundamental light of 65 fs, 800 nm wavelength, 82 MHz pulses from a Ti-sapphire laser were employed in transmission geometry. The size of the diameter of the circular probe area was 60 μm. The T phase is expected to be $4mm$ constrained monoclinic symmetry while the fully relaxed films are expected to have the bulk-like $3m$ constrained monoclinic symmetry. These two symmetry components can be neatly separated from each other by a simple SHG experiment. If the polarization c-axis is pointing out-of-plane of the $4mm$ film, no signal is generated when the film normal is coincident with the incident fundamental beam ($\theta = 0°$); hence all signal in this

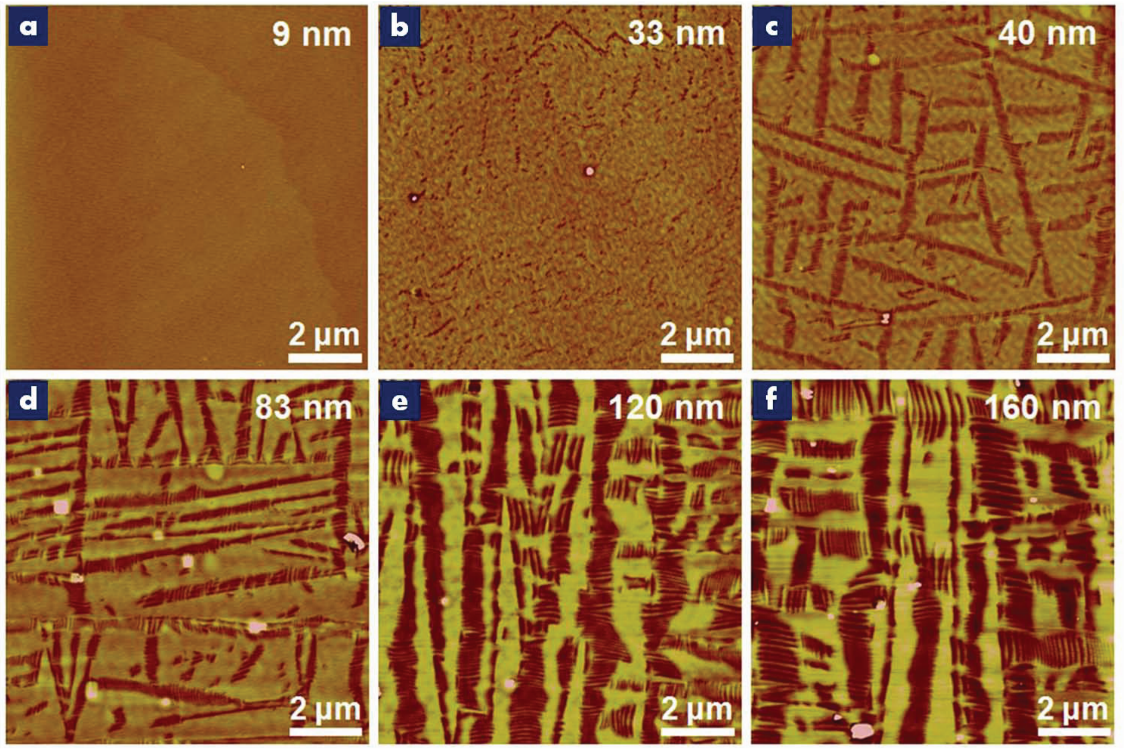

Figure 6.6: Thickness dependence evolution of surface morphology as probed by atomic force microscopy for (a) 9 nm, (b) 33 nm, (c) 40 nm, (d) 83 nm, (e) 120 nm, and (f) 160 nm.

geometry is from the R phase. When $\theta \neq 0°$, the T phase is found to dominate the generate *p*-polarized SHG signal as determined from the symmetry analysis of SHG polarization studies (Figure 6.7). Thus the volume fraction of R phase in the film was approximately estimated as

$$f_{Rh} \sim \frac{sI_p^{2\omega}(\theta = 0°)}{sI_p^{2\omega}(\theta = 0°) + I_p^{2\omega}(\theta = 30°)} \tag{6.1}$$

and is plotted in Figure 6.5. The phase stabilities and their boundaries are predicted from both thermodynamic analysis (solid lines in Figure 6.8) and phase-field model (scattered symbols in Figure 6.8) in which the spatial distribution of the polarization field and its evolution is described by the time dependent Ginzburg-Landau (TDGL) equations. For films of the same thickness, a purely tetragonal film tiled by $\theta = 30°$ to the surface normal was found to produce $\sim$ 3 times the *p*-polarized SHG signal of a purely rhombohedral BFO (001) film in normal incidence, reflecting a difference in the (square of the) effective nonlinear coefficients of the two cases; hence s $\sim$3, was used in the above relation. While the actual value of f_{Rh} could be in error by a volume fraction of $\sim \pm 5\%$, the trend of f_{Rh} with increasing film thickness is correct.

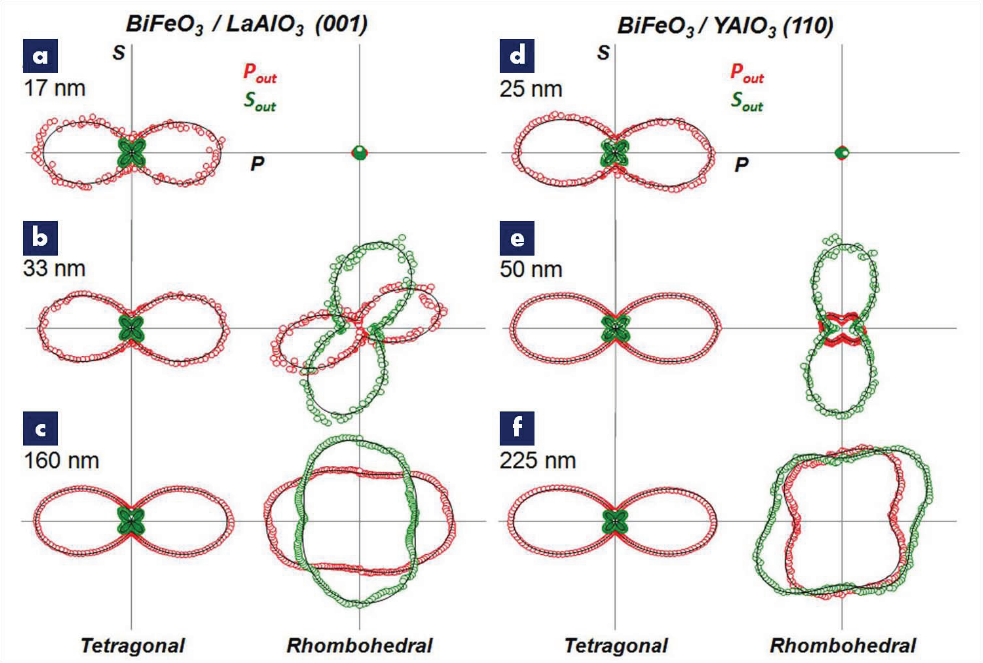

Figure 6.7: SHG signal obtained in tilted (left plots, $\theta = 30°$) and normal (right plots, $\theta = 0°$) incidence configurations for the BFO/LAO (a-c) with output analyzer along S (green) and P (red) polarizations and BFO/YAO (d-f) films with output analyzer along 45° (green) and −45° (red) to the pseudocubic axes. The SHG signal for $\theta = 0°$ increases with film thickness, suggesting increasing contribution from the R phase in films on both substrates. The $\theta = 30°$ is dominated by SHG signal from the T phase. Solid black lines are theory fits for T and R phases, accounting for different domain variants.

Let us now turn our attention to understanding the atomic structure of this isosymmetric phase boundary in this mixed phase. High-resolution AFM images (Figure 6.9a) show a characteristic striped contrast that we attribute to the mixed phase. From such images, the spacing of the stripes is measured to be ∼30 to 50 nm, with a peak-to-valley height difference of 2 to 3 nm (Figure 6.9b). We then carried out low- and high-resolution transmission electron microscopy (TEM) studies of this mixed phase region. Figure 6.10a shows a typical low-magnification TEM image of the portion of the sample that exhibits the striped contrast. The spacing of the stripes in this image is commensurate with that obtained in the AFM image, that is 30 to 50 nm. Higher-resolution atomic imaging (carried out on the TEAM 0.5 microscope) reveals the structural details of this mixed phase (Figure 6.10b), in which the T phase is interspersed between two R phase regions. The structure changes smoothly from the T phase to the R phae over a distance of ∼10 unit cells, as shown in Figure 6.10c. Specifically, the out-of-plane lattice parameter changes from 4.06 Å in the R phase to 4.65 Å in the T phase without the insertion of misfit dislocations. The in-plane lat-

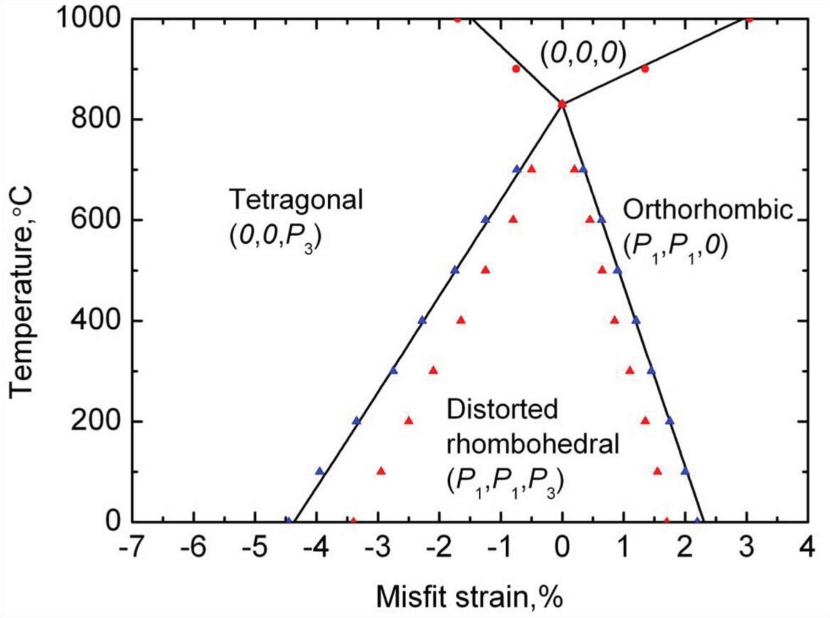

Figure 6.8: Phase stability diagram of (001) BFO thin film as a function of temperature and misfit in-plane strain. Scattered symbols are phase boundaries from phase-field simulation and solid lines are from thermodynamic calculation.

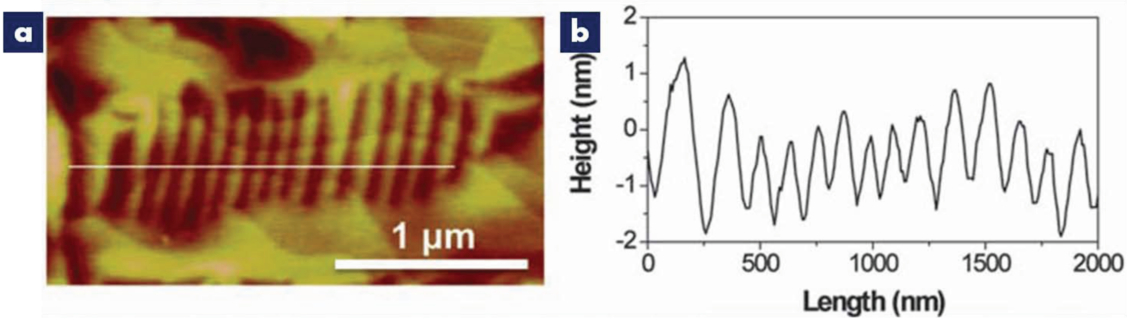

Figure 6.9: Morphology of mixed phase feature. (a) High-resolution AFM image of a mixed phase region. (b) Corresponding line trace at white line in (a) demonstrates ~2 to 3 nm height changes going from the peak to the valley.

tice parameter is constrained by the substrate lattice parameter and changes slightly (from ~3.8 Å in the R phase to ~3.7 Å in the T phase). Thus, the c/a ratio changes from 1.07 for the R phase to 1.27 in the T phase in just over 10 unit cells.

To understand the observed coexistence of T and R phases, we performed density functional calculations within the local density approximation plus the Hubbard parameter U (LDA+U) approximation ($U_{eff} = U - j = 2$ eV), using the projector

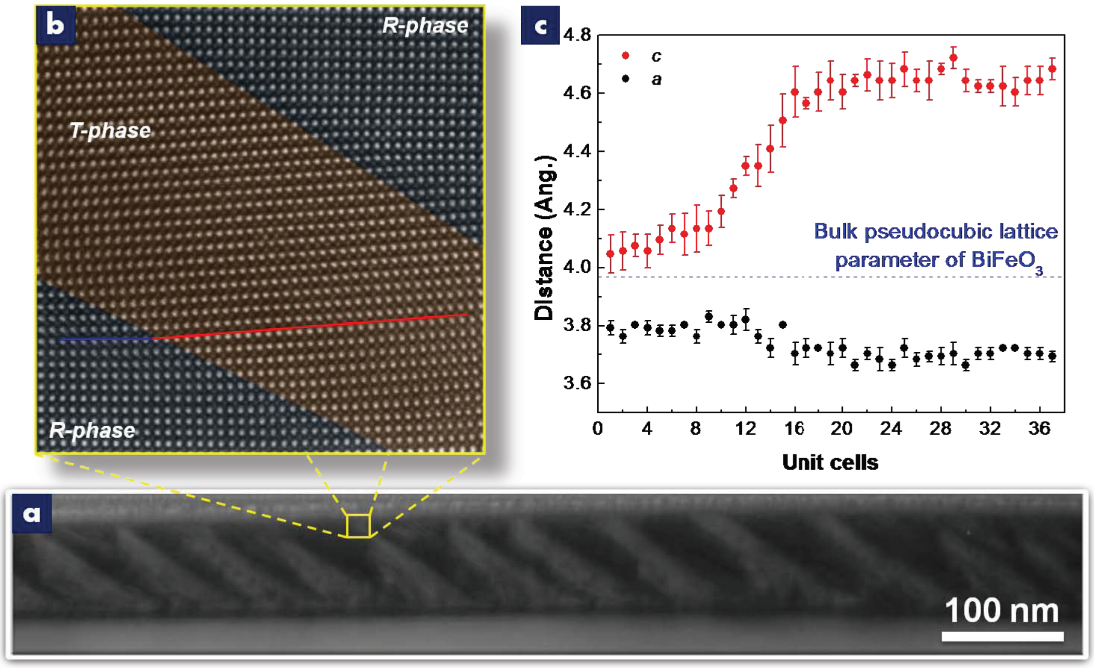

Figure 6.10: Structural evolution at T/R phase boundary in mixed phase BFO films. (a) Low-resolution cross-sectional TEM image of a mixed phase region in a 85-nm-thick BFO/LAO film. Here, the light areas correspond to the T phase and the dark areas to the R phase. (b) High-resolution TEM image of the boundary between R and T regions, indicated by dashed lines. A smooth transition between phases is observed; no dislocations or defects are found at the interface. (c) Corresponding in-plane (a, black) and out-of-plane (c, red) lattice parameters (mean±SD) demonstrate nearly a 13% change in the out-of-plane lattice parameter in just under 10 unit cells.

augmented wave (PAW) method as implemented in the Vienna ab initio simulation package (VASP) [96] [97]. We use a monoclinic 10-atom unit cell, which allows the structure to continuously change from the $R3c$ rhombohedrally distorted symmetry of bulk BFO to the $P4mm$ tetragonally distorted symmetry. We employ a 5 by 5 by 5 k-point sampling and a plane wave energy cut-off of 550 eV, and assume a G-type antiferromagnetic ordering of bulk BFO. To simulate the effect of epitaxial strain, we constrain the unit cell lattice vectors in the pseudocubic (001) plane and relax the out-of-plane cell parameter and all internal coordinates by minimizing the Hellman-Feynman forces to tolerance of 0.005 eV/Å. The internal coordinates are initialized corresponding to monoclinic Cc symmetry. The results for compressive strain are shown in Figure 6.11a and b. Strains are given relative to the LDA+U equilibrium lattice parameter a=3.89 Å of bulk $R3c$ BFO.

We find that for a compressive strain, around 4.5% BFO undergoes a strain-

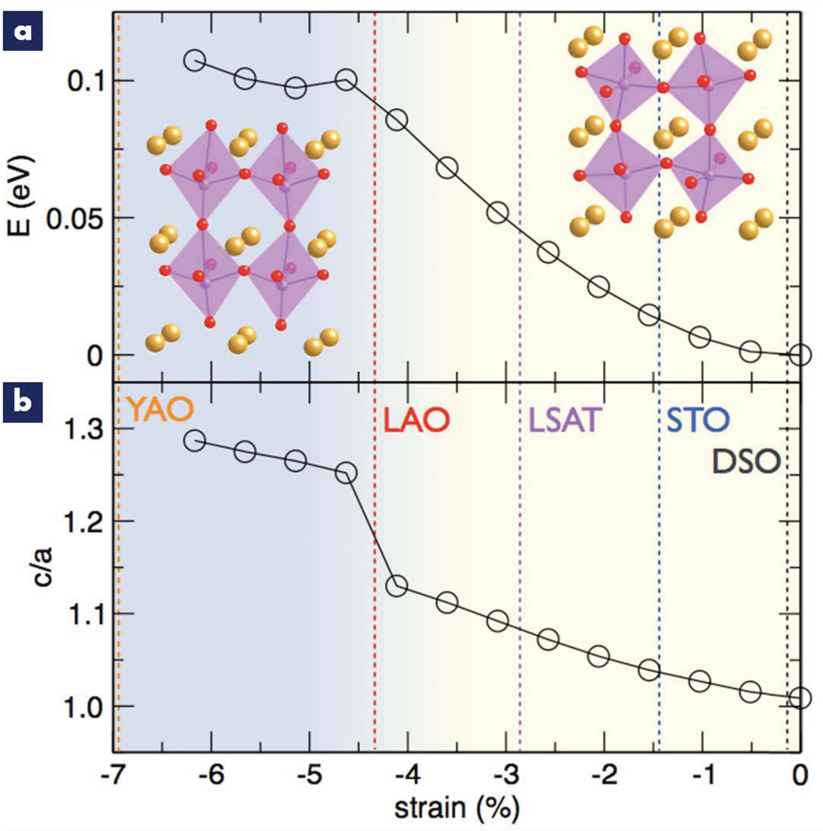

Figure 6.11: Ab initial calculations of phase evolution between T and R phases. (a) Evolution of the energy of the BFO structure as a function of in-plane strain. (b) Evolution of the c/a lattice parameter ratio as a function of strain for BFO. These data show the presence of two phases – both with monoclinic symmetry – the long-axis T phase (left) and the short-axis R phase. The lattice mismatches between a number of commonly used and tested oxide substrates are shown as dashed lines.

induced iso-symmetric structural transformation [98] that is accompanied by an abrupt increase in c/a ratio (Figure 6.11). Although the structures on both sides of this transition have the same monoclinic symmetry (Cc), there is a distinct change in the ionic coordinates from a distorted version of the rhombohedral bulk structure (with octahedral coordination of the Fe^{+3} cation) to a structure with essentially five-fold coordination of the Fe cation, resembling the "super-tetragonal" structure observed for $PbVO_3$ and $BiCoO_3$ [99] [100] but with additional tilting of the oxygen polyhedra (see insets in Figure 6.11a). The energy versus strain curve (Figure 6.11a) shows a maximum separating the two lower-energy phases at around 4.5% strain, suggesting that films strained to this critical value may lower their energy by spontaneously phase-separating into the T and R phases. In this case, the two phases have in-plane lattice parameters that are smaller and larger, respectively, than that of the substrate, allowing for phase-separation without an overall change of in-plane film dimensions. Films grown at higher strain values will be in the metastable tetragonal-like phase energy minimum and are not expected to phase separate. Wehave investigated this experimentally by studying the evolution of the BFO films on a wide range of substrates, including (110) $DyScO_3$ (DSO) (a=3.94 Å), STO (a=3.905 Å), (001) $(LaAlO_3)_{0.3}(SrAl_{0.5}Ta_{0.5}O_3)_{0.7}$ (LSAT) (a=3.87 Å), LAO (a=3.79 Å), and YAO (a=3.69 Å) (all lattice parameters reported here are the cubic or pseudocubic values, and the lattice mismatch of the various substrates relative to bulk BFO is shown in Figure 6.11a and b). These studies show that BFO films on YAO consist entirely of the T phase for film thicknesses up to ∼220 nm, whereas films on LAO are mixed T and R phases, and films on LSAT, STO, and DSO are rhombohedral-like in nature, consistent with the theoretical predictions in Figure 6.11. Phase field calculations, shown in Figure 6.8, confirm the conclusions from ab initio calculations. They also reveal the existence of the two-phase region between the tetragonal-like and rhombohedral-like phases and show the persistence of this two phase region at finite temperature.

6.2 Electrically Controllable Spontaneous Magnetism in Nanoscale Mixed Phase $BiFeO_3$ System

In this section we will continue discussing the strain induced formation of a nanoscale mixture of the T and R phases. Over the past two decades, novel physical phenomena have emerged in complex oxides, at interfaces that are naturally created within the system (e.g., phase-separated manganites, relaxor ferroelectrics), or in artificially engineered heterostructures [86] [101] [102] [27] [29] [103]. Although many of these phenomena have emerged as a consequence of chemical substitutions, strain control is emerging as an equally powerful tool to create and manipulate such phenomena [104]. In this study we describe a novel approach to create a new magnetic state in BFO and the ability to electrically control this emergent magnetism at room temperature. An enhanced spontaneous magnetization arises in the R phase that is strain confined between areas in T phase. We demonstrate that this local magnetic moment can be erased by the application of an electric field. Moreover, reversal of the electric field polarity restores the mixed phase structure [45] [105].

6.2.1 Structure-topography relation of mixed phase system

Again, the samples were prepared using pulsed laser deposition in conjunction with high-pressure reflective high-energy electron diffraction to monitor the growth of the BFO thin films. A bottom conducting layer of $LaNiO_3$ was inserted in order to eliminate charging effects during X-ray illumination in magnetic measurements.

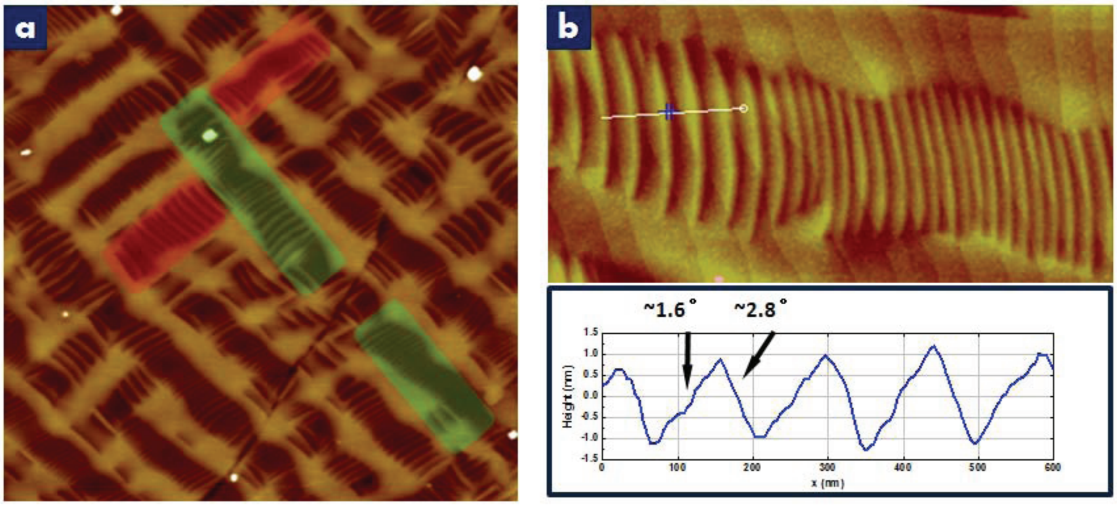

Figure 6.12: Detailed high-resolution AFM study of mixed phase BFO samples. (a) AFM topography image of mixed phase BFO sample. Red and green shaded areas indicate two sets of mixed phase features oriented at 90° to each other. (b) High-resolution AFM topography image of a mixed phase structure (top panel) and cross section line profile along the white line. R and T phases show different slopes of $\sim 1.6°$ and $\sim 2.8°$.

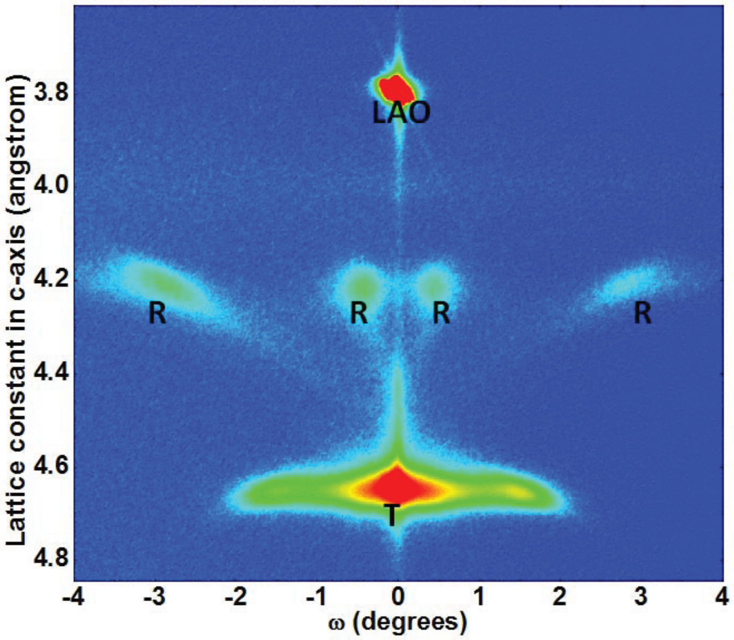

Figure 6.13: X-ray diffraction $2\theta - \omega$ map of a mixed phase film.

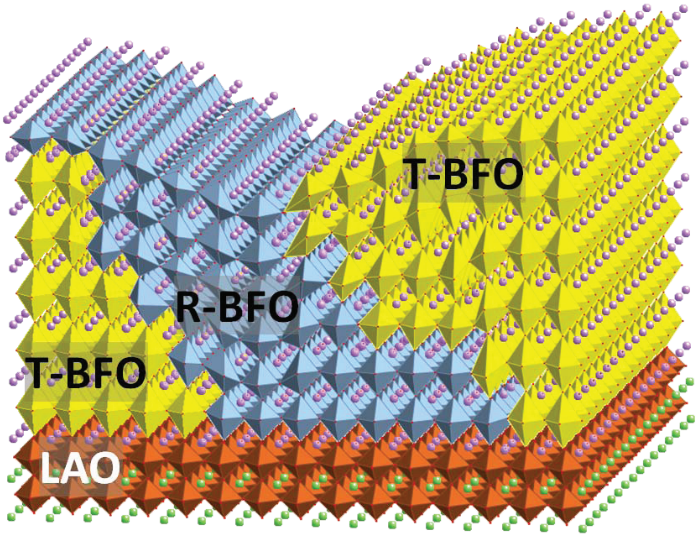

Figure 6.14: Schematic of T/R mixed phase structure.

Partial strain relaxation through control of the film thickness leads to the formation of two orthogonal arrays of nanoscale, T+R phase mixtures, as imaged by AFM shown in Figure 6.12a. The individual stripe-like regions, Figure 6.12b, consist of a nanoscale ensemble of T and R phase with a characteristic length scale of 20-40 nm. The graph in the bottom panel of this figure shows a cross-sectional line-profile of the mixed phase area, revealing two different tilting angles (2.8° and 1.6° relative to the surface plane) of the mixed phase areas. The structural details of such a mixed phase ensemble were identified from careful X-ray $2\theta-\omega$ scans, such as that shown in Figure 6.13. The X-ray data also identifies the structural distortion of the R phase, with out-of-plane lattice parameter of (c=4.17 Å); this coupled with reciprocal space maps provides a measure of the in-plane dimensions of this highly strained R phase to be 3.82 Å. From the four peaks arising from the R phase, Figure 6.13, the tilt angles for these can be divided into two groups, one $\sim$ 2.8° and the other $\sim$ 0.6°, which correspond to the green and red shaded area in Figure 6.12a. The broadening angle for the T phase (c=4.64 Å) is estimated to be $\sim$ 1.6°, resulting from the tilting of the T phase, consistent with the AFM measurement. Compared to the AFM line profile, we find that the R phase with a tilt angle of 2.8° is on the other side of the peaks to the T phase. Therefore, we can locate the R and T phases with the slopes of the topography shown in Figure 6.12b and schematically illustrated in Figure 6.14. The AFM and X-ray diffraction studies clearly establish the nanoscale, R-T mixed phase ensemble, in which the R phase is highly strained compared to the bulk. Since BFO in the bulk is a well-known ferroelectric and canted antiferromagnet [22] [106] [56], it is natural to ask: what is the magnetic state of the mixed phase BFO, especially in the highly strained R phase?

6.2.2 Enhanced magnetization in the highly distorted R phase in mixed phase $BiFeO_3$ films

X-ray magnetic circular dichroism (XMCD) (see Appendix X for details) is a powerful method to study the magnetic response of a material [107] [108]. We have employed this technique to explore the magnetic response of BFO films with mixed phases, and compared to unconstrained R and pure T phase films. X-ray absorption spectra (XAS) at Fe^{3+} $L_{2,3}$-edge using left and right circularly polarized soft X-rays, at grazing incidence ($\theta = 30°$) were obtained as a function of the external magnetic field in total electron yield (TEY) mode. Figure 6.15 shows the XMCD signal obtained from the difference between XAS in positive and negative (parallel and antiparallel to the k-vector of the incident X-rays) magnetic field ($+/-$ 2 T) and fixed X-ray polarization. The red curve in Figure 6.15 is from a pure rhombohedral phase BFO sample, which gives a negligible XMCD signal (since the canted moment is only ~6-8 emu/cc). No canting of Fe^{3+} spins is allowed in the tetragonal-like phase BFO due to symmetry and thus, it does not exhibit any XMCD (data in green in Figure 6.15) [109]. The significantly larger XMCD spectra of mixed T+R phase BFO ensembles are shown as the black curves in Figure 6.15, indicating that a higher magnetic moment is present in mixed phase BFO films. The XMCD spectra in Figure 6.15 are measured with left circularly polarized (LCP) X-rays; they reverse polarity when using right circularly polarized (RCP) X-rays, confirming that the response is magnetic in origin.

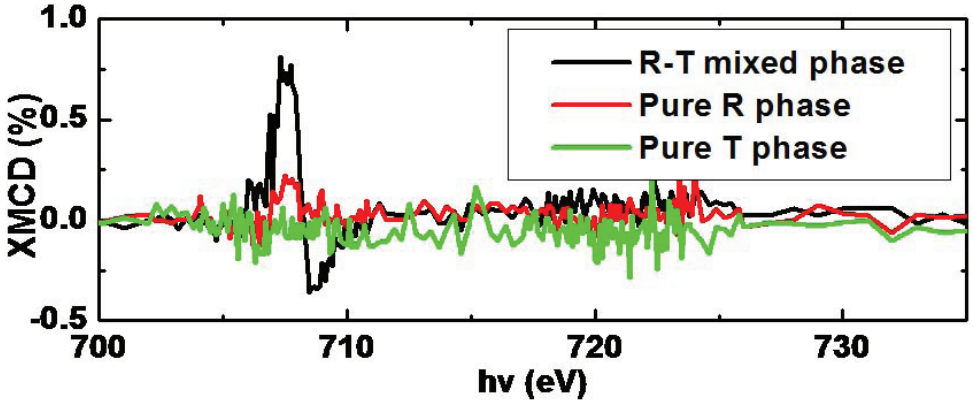

Figure 6.15: X-ray magnetic circular dichroism study of mixed phase, pure rhombohedral phase, and pure tetragonal-like phase BFO films. Fe^{3+} $L_{3,2}$ XMCD spectra of BFO films in the three different phases probed using fixed X-ray circular polarization (right circularly polarized) and point-by-point reversal of the external magnetic field of magnitude 2 T.

These measurements clearly reveal the existence of a spontaneous magnetic moment in the mixed phase samples. From the ∼ 0.7% XMCD signal, and using data for other iron oxide systems (Fe_3O_4) [110] [111] as a semi-quantitative calibration, we estimate the averaged magnetization to be of the order of 20-30 emu/cc in the top 5 nm (penetration depth for electrons in TEY mode) of the sample surface. In order to explore the microscopic origins of this enhanced magnetic moment, the XMCD signal was imaged using photoemission electron microscopy (PEEM).

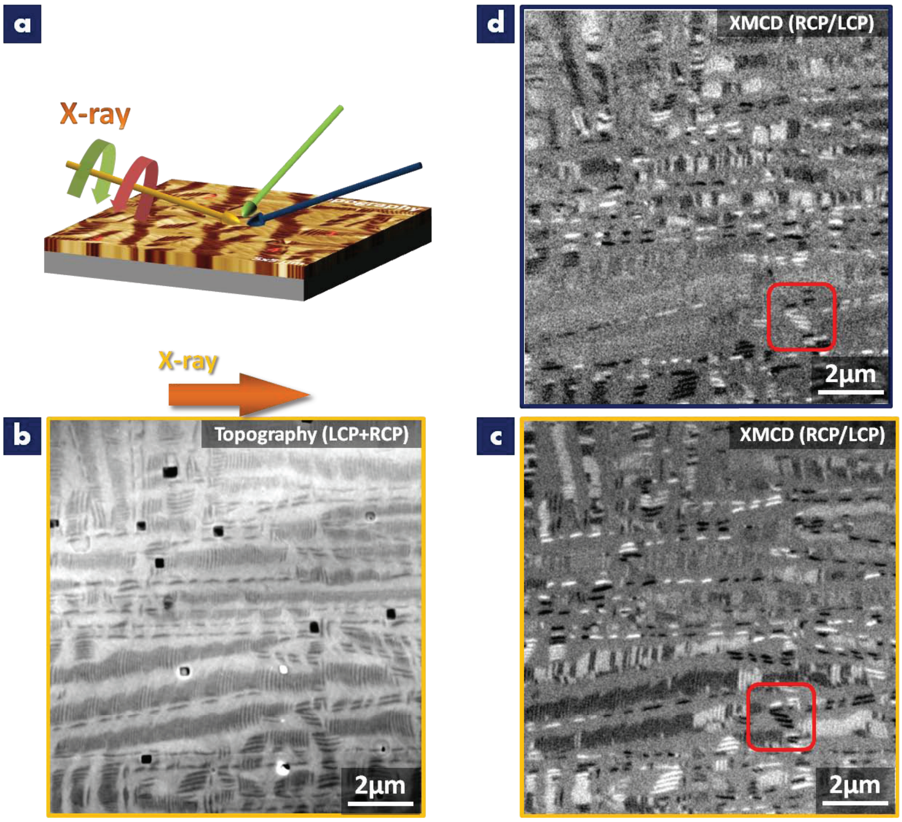

Figure 6.16: Photo-emission electron microscopy imaging of mixed phase film. (a) Schematic of geometry of the measurements. The circularly polarized X-rays indicated by yellow green and blue arrows impinge on the sample at 30° grazing incidence along different crystal orientations. (b) PEEM image obtained from the sum of PEEM image taken with left and right circularly polarized X-rays gives topographical contrast. (c) XMCD-PEEM image showing enhanced magnetic contrast is given from the ratio of PEEM images taken with left and right circularly polarized X-rays at the same location. (d) XMCD-PEEM image, showing reversed magnetic contrast, obtained after a sample rotation of 180° as compared to (b).

Spatially resolved PEEM images were obtained using both LCP and RCP incident X-rays at a grazing incidence angle ($\theta = 30°$). To enhance the difference in the

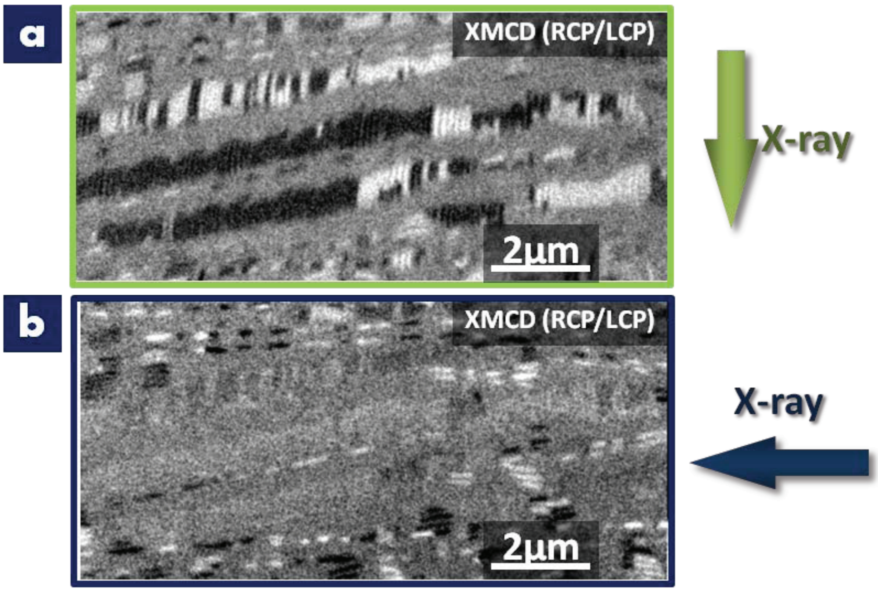

Figure 6.17: XMCD-PEEM images shown in (a) and (b) are obtained after a rotation of 90° and 180° of the sample, respectively relative to image in Figure 6.16b.

magnetic contrast and eliminated the contribution from the topographic contrast, the ratio of the two images were taken. The image contrast is effectively a map of the local magnetization vector; regions that have their magnetic moment lying parallel to the X-ray wave vector show bright contrast, while those that are antiparallel appear in dark contrast. XMCD-PEEM images were taken with the incident X-rays at various orientations ($\phi = 0°$, $90°$, $180°$), shown schematically in Figure 6.16a. Figure 6.16b is the PEEM image obtained by LCP X-ray at $\phi = 0°$, showing magnetic contrast superimposed with topographic contrast (main part). The darker areas in this image are in the valleys of the mixed phase features and brighter areas are at the peaks. Then, XMCD-PEEM image, which cancels the topographic contribution and enhance the magnetic contrast, is obtained from the ratio between the PEEM image taken with LCP and RCP incident X-rays. The XMCD image (Figure 6.16c) reveals the intrinsic magnetic contrast that appears as bright and dard stripe-like patterns indicating that these stripes have magnetic moments lying parallel and antiparallel to the incident X-rays. When the sample is rotated by 180°, all of the stripes reverse contrast, which further confirms the magnetic origin, Figure 6.16d. Moreover, after a 90° rotation of the sample about the sample normal, the stripes show weak or no contrast when the incident X-ray is perpendicular to their long axes; at the same time, the stripes show strongest contrast when the incident X-ray is parallel to their long sides (Figure 6.17). These measurements clearly indicate that the magnetic moments in the stripe-like area are lying along the long axis of the stripes. It is also important to note that

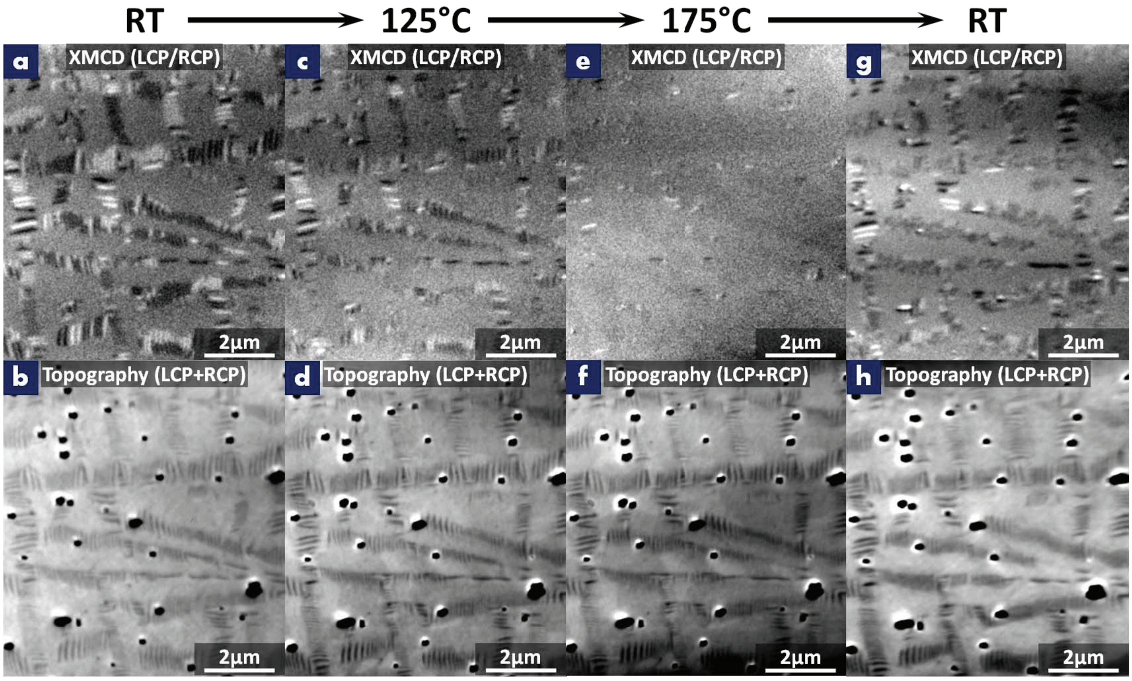

Figure 6.18: Temperature dependent PEEM imaging of mixed phase BFO films. (a), (c), (e), and (g) are XMCD-PEEM images at room temperature, 125°C,175°C and back to room temperature. XMCD-PEEM images are analyzed from the ratio of LCP and RCP images at the same location. (b), (d), (f), and (h) are corresponding topography images at varies temperature.

the regions in bright and dark magnetic contrast in Figure 6.16b are approximately of equal fractions. Then, temperature dependent PEEM images (Figure 6.18) have also been taken with heating and cooling process. Starting from room temperature, the XMCD-PEEM in Figure 6.18a shows similar magnetic contrast of the mixed phase stripes, while the topographic PEEM image (Figure 6.18b) shows its characteristic morphology. When the sample is heated up to 125°C, the magnetic contrast in the XMCD-PEEM image (Figure 6.18c) becomes burry and the black and white stripes in this images start to fade away. When the temperature hits 175°C, 99% of the magnetic contrast in the XMCD-PEEM image (Figure 6.18e) vanishes. However, as soon as we turn off the heat and cool the sample back to room temperature, the magnetic contrast of the mixed phase stripes re-appears and 80% of which recovered their original contrast, while the switching of individual stripe contrast can be observed. The important thing to note is that the topography of this area (Figure 6.18b,d,f, and h) remains unchanged during the whole heating and cooling process.

To further explore the origins of the magnetic response (i.e., does it arise at the interface between the T/R phases OR is it located within the highly strained R

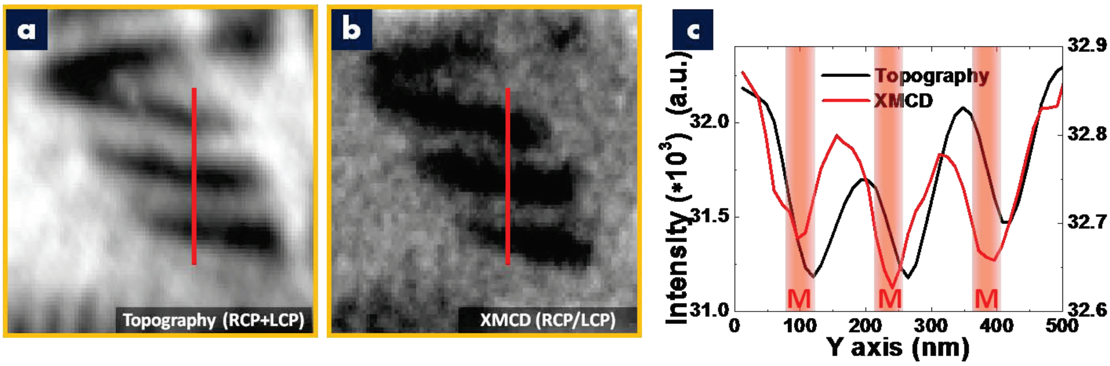

Figure 6.19: Detailed PEEM analysis of a mixed phase structure. (a), (b) Zoom-in topographic and XMCD-PEEM image of the area indicated by a red box in Figure 6.16c. (c) Line profile of the topographic and XMCD signal at the red line marked in (a) and (b).

phase), we focus on the area indicated by a red square in Figure 6.16c and compare with both the AFM line scans and the corresponding piezo-response force microscopy (PFM) images of the same area. Figure 6.19a and b are the topographic and XMCD-PEEM image of a mixed phase structure indicated by the red box in Figure 6.16c. By taking the line profiles of both topographic and XMCD-PEEM image (Figure 6.19c) at the same location (red line in Figure 6.19a and b), surprisingly, we see an off-set of the magnetic signal (red curve in Figure 6.19c) to the topography (black curve in Figure 6.19c) of the same location. The areas where the magnetic moment reaches its maxima [dips (local minima) of the red curve, indicated with red bands] only appear one side of the mixed phase strips (black curve). As we discussed in Figure 6.12, on one side of the "hill" (stripe) locates the T phase, and the other side locates the phase. However, it is not obvious that on which side the magnetic moment emerges. In order to understand this, we applied PFM to scan the same area. Figure 6.20a is the AFM topography image and the corresponding in-plane PFM image acquired simultaneously at exactly the same position is shown in Figure 6.20b. The PFM image shows bright contrast of "lip-shaped" patterns surrounding the stripe-like features. By obtaining a line profile across the mixed phase features at the same position as in Figure 6.19, the topography curve (black curve in Figure 6.20c) shows a significant asymmetry of slopes on the two sides of the mixed phase stripes similar to what was shown in the cross sectional AFM line profile in Figure 6.12b. Combining the IP-PFM line profile (green curve in Figure 6.20c) with the topology scan (black curve in Figure 6.20c) helps us to conclude that the "lip-shaped" patterns form the T/R interface. More importantly, the area enclosed by the "lip-shaped" region is on the steeper side, which is the R-phase as shown in Figure 6.12b. By superimposing the PEEM and PFM line profiles together in Figure 6.20d, it is clear that this highly distorted R-phase is the source of the enhanced magnetic moment in the XMCD image, arising

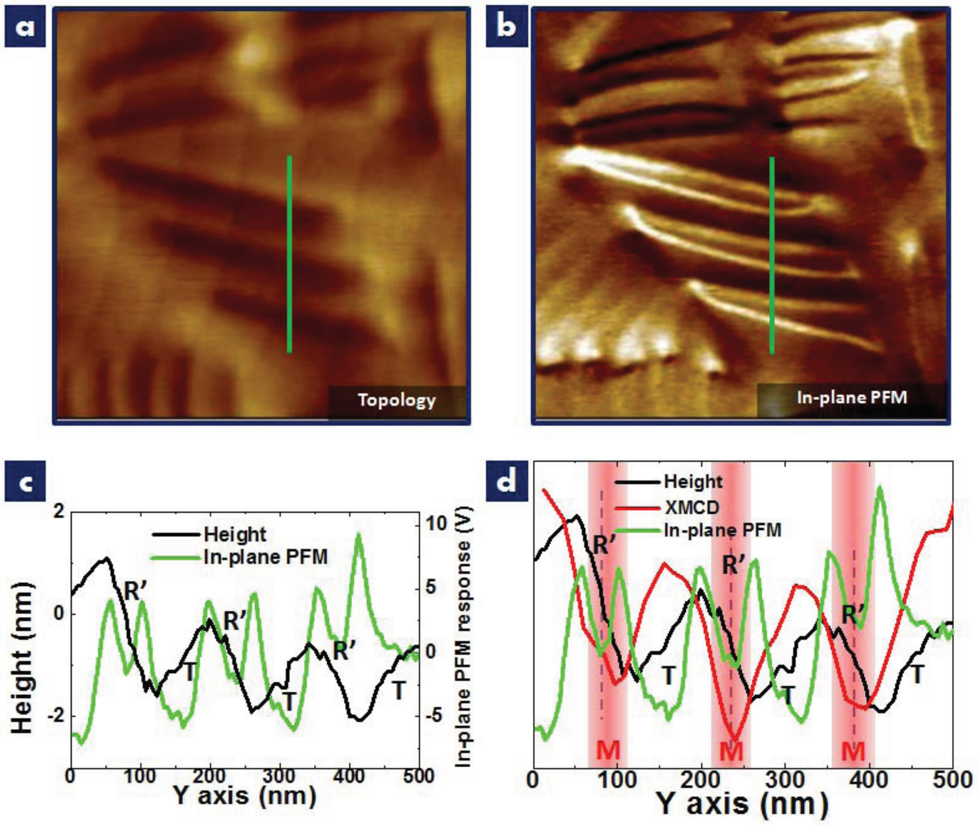

Figure 6.20: Detailed PFM combined with PEEM analysis of a mixed phase structure. (a), (b) Topographic and in-plane PFM image of the area indicated by a red box in Figure 6.16c. (c) Line profile of the topography and in-plane PFM signal at the green line marked in (a) and (b). (d) Combined line profile of both PEEM and PFM information at the same location obtained from the red line at Figure 6.19a and b and Figure 6.20a and b.

from a piezomagnetic effect [112] [113] [114], which can be estimated as follows.

Since the magnetization of the system is given by

$$M = \chi H \tag{6.2}$$

we have

$$dM = \chi dH \tag{6.3}$$

Also the stress and the strain can be related with Young's Modulus

$$d\sigma = Y d\varepsilon \tag{6.4}$$

Then we have

$$\frac{dM}{d\sigma} = \frac{\chi}{Y}\frac{dH}{d\varepsilon} = \frac{\chi}{Y}\left(\frac{d\varepsilon}{dH}\right)^{-1} \tag{6.5}$$

The enhancement of the magnetization can be estimated as

$$\begin{aligned}\Delta M &= \frac{dM}{d\sigma}\cdot\Delta\sigma = \frac{\chi}{Y}\left(\frac{d\varepsilon}{dH}\right)^{-1}\Delta\sigma \\ &\simeq \frac{5\times10^{-5}\mathrm{emu}\cdot\mathrm{cc}^{-3}\cdot\mathrm{Oe}^{-1}}{2\times10^{11}\mathrm{P}}\cdot\left(10^{-9}Oe^{-1}\right)^{-1}\times10^{9}\mathrm{P} \\ &= 250\mathrm{emu}\cdot\mathrm{cc}^{-3} \end{aligned} \tag{6.6}$$

where

$$\begin{aligned}\chi &= 5\times10^{-5}\mathrm{emu}\cdot\mathrm{cm}^{-3}\cdot\mathrm{Oe}^{-1} \\ Y &\approx 2\times10^{11}\mathrm{P} \\ \left(\frac{d\varepsilon}{dH}\right) &\approx 10^{-9}\mathrm{Oe}^{-1} \\ \Delta\sigma &\approx 10^{9}\mathrm{P}\end{aligned}$$

Although this estimation doesn't give us a exact quantitative match to our experimental data, the measured enhanced magnetization (~50 emu·cm^{-3}) does qualitatively agree with the calculated number. The difference between these two values mainly comes from the factor $d\varepsilon/dH$, which doesn't have an accurate experimental value.

Macroscopic conventional SQUID magnetometry of a large set of mixed phase samples (Figure 6.21) yielded an average magnetic moment of ~5 emu/cc that is consistently higher than the pure T-phase samples that show moments ~1 emu/cc. This moment in the mixed phase can be understood from a careful examination of the AFM and PEEM images coupled with XRD studies. The AFM images show a surface area fraction of the R-phase of ~30-40%; however, careful analysis of 2θ-ω XRD scans (Figure 6.13) yields a volume fraction of the R-phase of ~10-15%, suggesting that the R-phase is tapered towards the substrate. From this volume fraction information the magnetic moment of the R-phase is estimated to be ~30-50 emu/cc, which is consistent with the data we obtained from surface-sensitive XMCD measurements. In order to further verify the existence of this magnetic moment we explored the exchange coupling of this moment to a ferromagnetic layer.

2.5 nm thick, ferromagnetic $\mathrm{Co_{.90}Fe_{.10}}$ (CoFe) thin films were deposited onto BFO films containing a large fraction of mixed phase regions at room temperature by CD magnetron sputtering in a UHV system of base pressure of $\sim 5\times10^{-8}$ Torr. The CoFe films were capped with a 2 nm thick layer of Pt to prevent its oxidation. A uniform magnetic field of 200 Oe was applied during the CoFe growth to set the uniaxial anisotropy direction. Then, Co-edge XMCD-PEEM imaging was employed in different orientations (Φ = 0°, 45°, 90°, 180°) to investigate the ferromagnetic domain structures in CoFe layer. Figure 6.22a is taken with LCP X-rays, which clearly shows us the topography of mixed phase structure covered by CoFe that

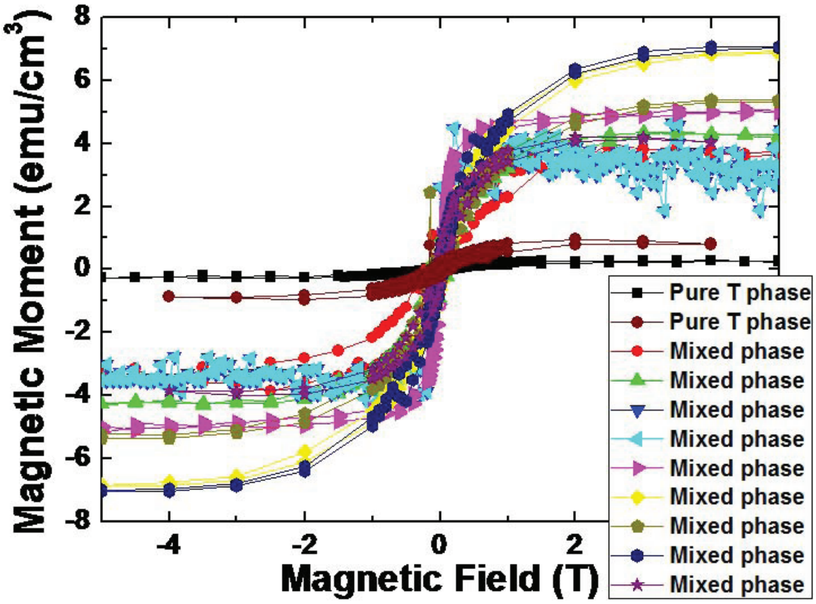

Figure 6.21: SQUID magnetometry measurements on mixed phase and pure tetragonal phase BFO films. This series of measurements addresses the averaged magnetization of mixed phase and pure tetragonal phase BFO films.

was grown in an applied magnetic field along $[\bar{1}\bar{1}0]$ direction (green arrow). Bar-shaped magnetic domains can be seen in the XMCD-PEEM images (Figure 6.22b-e). It is interesting to note that the bar-shaped domain patterns in these magnetic images strongly resemble the corresponding bar-shaped patterns (identified within the red box and schematically depicted in Figure 6.22f) in the topographic image in Figure 6.22a. Figure 6.22b was taken with circularly polarized X-rays incident from [100] direction (orange arrow), which shows horizontal bar-shaped domains in dark contrast while vertical bar-shaped domains appear in neutral (gray) contrast, indicating that the magnetization of CoFe in the horizontal and vertical domains are pointing antiparallel ($[0\bar{1}0]$) and perpendicular ([100] or $[\bar{1}00]$) to the incident X-rays, respectively. This magnetization direction coupled with the moment in the mixed phase features (along the long side of the mixed phase stripes but the short side of the CoFe domains), which is also schematically shown in Figure 6.22f. When we rotate the sample by 45° with respect to the sample normal, the XMCD amplitude from the CoFe domains decreases by about a factor of $\sqrt{2}$, reflecting the reduced contrast in the PEEM image shown in Figure 6.22c. This confirms our interpretation of the moment directions. With a 90° rotation of the sample, the change of contrast of XMCD-PEEM image (Figure 6.22d) suggests that the moments in the vertical CoFe domains lie along [100] direction. Finally, a 180° rotation of the sample gives us a fully reversed contrast image (Figure 6.22e), confirming the contrast we observed here

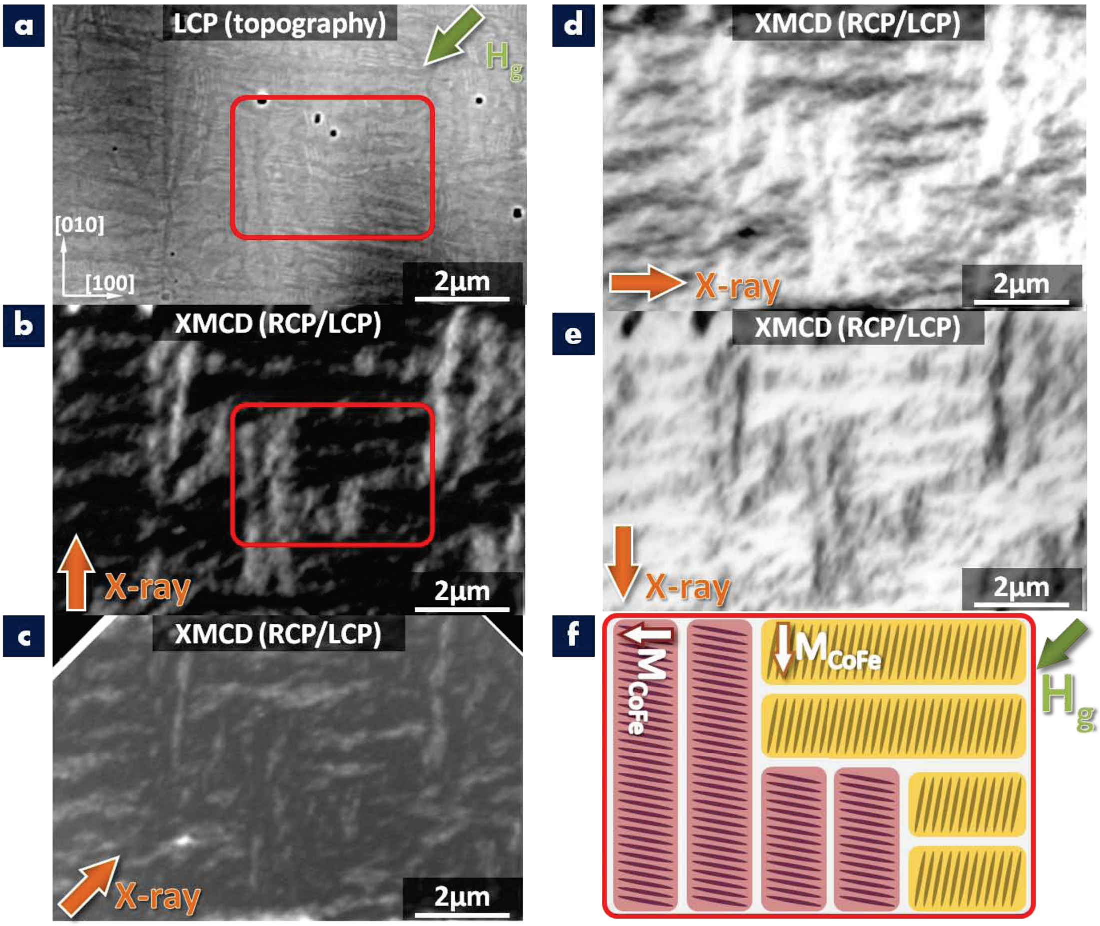

Figure 6.22: Exchange coupling between $Co_{.90}Fe_{.10}$ layer and mixed phase $BiFeO_3$ films beneath. (a) LCP-PEEM image of CoFe layer on mixed phae BFO film showing mainly topographic contrast. The green arrow indicates the direction of applied magnetic field during CoFe growth. (b)-(e) XMCD-PEEM image obtained from the ratio of LCP and RCP-PEEM images of the same area, showing magnetic contrast of CoFe domains. White, black and gray contrast indicate magnetic moment pointing parallel, antiparallel, and perpendicular to the incident X-rays. The direction of incident X-rays is marked by orange arrows. (f) Schematic of magnetic domains in CoFe (wide yellow and purple bars), which simulates the CoFe domain structures of the red-boxed area in (a) and (b), coupled with the mixed phase structure (thin dark ovals) beneath. Magnetic moment of CoFe domains are shown as white arrows. Scale bars are 2 μm.

is indeed magnetic in origin and that the moments in the CoFe layer are magnetically coupled to the moment in the R-phase of the BFO underlayer [115]. This robust magnetic coupling provides additional evidence on the existence of magnetic moments embedded in R-phase of the mixed phase nanostructures in BFO.

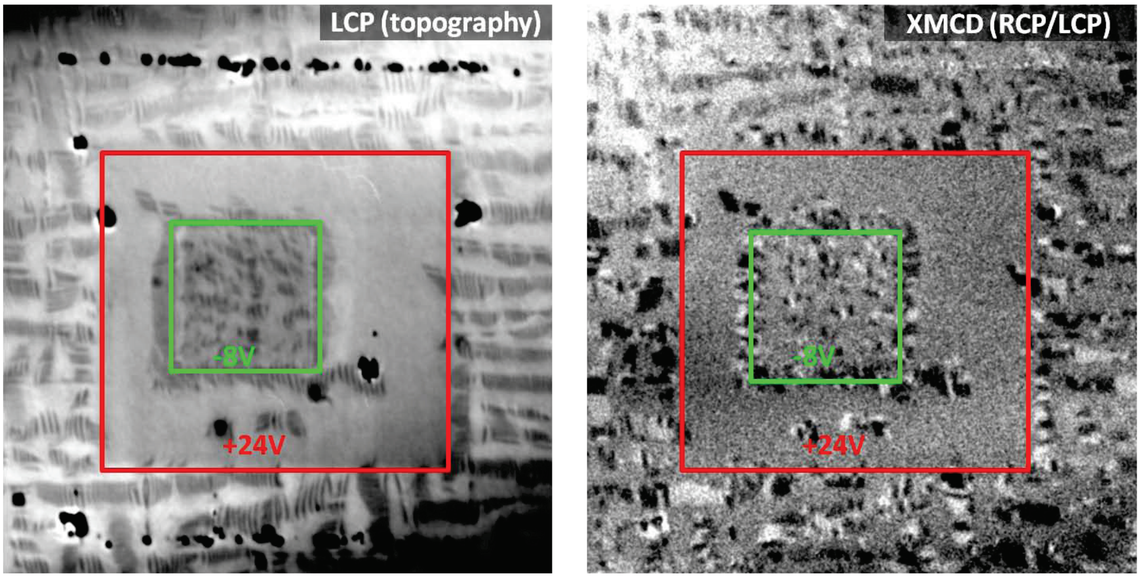

Figure 6.23: Illustration of electrical control of magnetism in mixed phase $BiFeO_3$ thin films. (a) LCP-PEEM image of a box-in-box electrically switched area, where the mixed phase stripes are erased in the area indicated by a red box by scanning with a PFM tip at +24V DC bias and returned by applying -8V DC bias in the area indicated by a green box. (b) XMCD-PEEM image of same area as in (a) showing magnetic contrast from the mixed phase structures. The magnetic moments between the red and green boxes are erased by the electric field and the magnetic moments in the green boxed are turned on again.

Having established the existence of a nanoscale magnetic moment in the highly distorted R-phase, we demonstrate the electric field modulation of this magnetism. By applying a +24 V DC bias to a PFM tip and scanning over the red rectangular area (Figure 6.23a), the mixed phase features can be transformed into pure tetragonal phase. Then, applying a -8V DC bias to the green rectangular area, the mixed phase features return. Details of the electric field induced phase evolution and the corresponding changes in the piezoresponse are discussed in ref. [116]. LCP- and XMCD-PEEM images of this area are shown in Figure 6.23. By mapping the magnetic moments (XMCD image, Figure 6.23b), no magnetic contrast is observed in the area between the green and red boxes, consistent with the non-magnetic state of tetragonal phase. In contrast, the XMCD image shows the characteristic stripe-shaped features both inside the green box and outside the red box area, indicative of a magnetic moment in them. Therefore, we conclude that magnetic moments in these stripe-shaped nanoscale mixed phase regions can be erased and rewritten at room temperature withe only the application of an electric field.

In summary, we have demonstrated a novel approach to manipulate the canted moment of the R-phase of $BiFeO_3$, by creating a nanoscale ensemble in which the

R-phase is mechanically confined by regions of the T-phase. This nanoscale mixture displays functional responses that are strikingly different from the parent phases. Detailed analyses using a combination of experimental probes reveal that the enhanced magnetic moment resides within the distorted R-phase rather than at the interfaces. The strong coupling to the underlying lattice is a primary reason that this moment is not switchable with a magnetic field; in contrast, it can be controlled by electric fields that making it a novel vehicle to demonstrate magnetoelectric coupling and electric field control of magnetism in this multiferroic system. Deterministic control of the location, size and distribution of this mixed phase ensemble would be a critical enabler of approaches to use the results of this study in future magnetoelectronic applications.

Bibliography

[1] Spaldin, N. A. *Magnetic Materials: Fundamentals and Applications* (Cambridge University Press, 2003).

[2] Fiebig, M. Revival of the magnetoelectric effect. *J. Phys. D.: Appl. Phys.* **38**, R123–R152 (2005).

[3] Eerenstein, W., Mathur, N. D. & Scott, J. F. Multiferroic and magnetoelectric materials. *Nature* **442**, 759–765 (2006).

[4] Ramesh, R. & Spaldin, N. A. Multiferroics: Progress and prospects in thin films. *Nature Mater.* **6**, 21–29 (2007).

[5] Cheong, S.-W. & Mostovoy, M. Multiferroics: A magnetic twist for ferroelectricity. *Nature Mater.* **6**, 13–20 (2007).

[6] Hill, N. A. Why are there so few magnetic ferroelectrics? *J. Phys. Chem. B* **104**, 6694–6709 (2001).

[7] Wang, J. *et al.* Epitaxial $BiFeO_3$ multiferroic thin film heterostructures. *Science* **299**, 1719–1722 (2003).

[8] Hur, N. *et al.* Electric polarization reversla and memory in a multiferroic material induced by magnetic fields. *Nature* **429**, 392–395 (2004).

[9] Kimura, T., Goto, T., Ishizaka, K., Arima, T. & Tokura, Y. Magnetic control of ferroelectric polarization. *Nature* **426**, 55–58 (2003).

[10] Attwood, D. *Soft X-rays and Extreme Ultraviolet Radiation* (Cambridge, 2000).

[11] Stöhr, J. & Anders, S. X-ray spectromicroscopy of complex meterials and surfaces. *IBM J. Res. Develop* **44**, 535–551 (2000).

[12] Stöhr, J., Padmore, H. A., Anders, S., Stammler, T. & Scheinfein, M. R. Principles of x-ray magnetic dichroism spectromicroscopy. *Surf. Rev. Lett.* **5**, 1297–1308 (1998).

[13] Stöhr, J. *NEXAFS Spectroscopy* (Springer-Verlag, 1992).

[14] Jorgensen, J. D. *et al.* Structural properties of oxygen-deficient $yba_2cu_3o_{7-\delta}$. *Phys. Rev. B* **41**, 1863–1877 (1990).

[15] Millis, A. J., Shraiman, B. I. & Mueller, R. Dynamic jahn-teller effect and colossal magnetoresistance in $la_{1-x}sr_xmno_3$. *Phys. Rev. Lett.* **77**, 175–178 (1996).

[16] Dagotto, E., Hotta, T. & Moreo, A. Colossal magnetoresistant materials: They key role of phase separation. *Phys. Rep.* **344**, 1–153 (2001).

[17] Schmid, H. Multi-ferroic magnetoelectrics. *Ferroelectrics* **162**, 317–338 (1994).

[18] Kittel, C. *Introduction to Solid State Physics* (John Wiley and Sons, Inc., 1996).

[19] Stöhr, J. & Siegmann, H. C. *Magnetism From Fundamentals to Nanoscale Dynamics* (Springer, 2006).

[20] Merz, W. J. Domain formation and domain wall motions in ferroelectric batio_3 single crystals. *Phys. Rev.* **95**, 690–698 (1954).

[21] Streiffer, S. K. *et al.* Domain patterns in epitaxial rhombohedral ferroelectric films. i. geometry and experiments. *J. Appl. Phys.* **83**, 2742–2753 (1998).

[22] Ederer, C. & Spaldin, N. A. Weak ferromagnetism and magnetoelectric coupling in bismuth ferrite. *Phys. Rev. B* **71**, 060401 (2005).

[23] Zalesskiĭ, A. V., Frolov, A. A., Khimich, T. A. & Bush, A. A. Composition-induced transition of spin-modulated structure into a uniform antiferromagnetic state in a $\mathrm{Bi}_{1-x}\mathrm{La}_x\mathrm{FeO}_3$ system studied using ^{57}Fe NMR. *Phys. Solid State* **45**, 141–145 (2003).

[24] Chu, Y.-H. *et al.* Nanoscale domain control in multiferroic $\mathrm{BiFeO_3}$ thin films. *Adv. Mater.* **18**, 2307–2311 (2006).

[25] Chu, Y.-H. *et al.* Domain control in multiferroic $\mathrm{BiFeO_3}$ through substrate vicinality. *Adv. Mater.* **19**, 2662–2666 (2007).

[26] Kalinin, S. V., Shao, R. & Bonnell, D. A. Local phenomena in oxides by advanced scanning probe microscopy. *J. Am. Ceram. Soc.* **88**, 1077–1098 (2005).

[27] Reyren, N. *et al.* Superconducting interfaces between insulating oxides. *Science* **317**, 1196–1199 (2007).

[28] Chakhalian, J. *et al.* Magnetism at the interface between ferromagnetic and superconducting oxides. *Nature Physics* **2**, 244–248 (2006).

[29] Yu, P. *et al.* Interface ferromagnetism and orbital reconstruction in $BiFeO_3 - La_{0.7}Sr_{0.3}MnO_3$ heterostructures. *Phys. Rev. Lett.* **105**, 027201 (2010).

[30] Přívratská, J. & Janovec, V. Pyromagnetic domain walls connecting antiferromagnetic non-ferroelastic magnetoelectric domains. *Ferroelectrics* **204**, 321–331 (1997).

[31] Přívratská, J. & Janovec, V. V. spontaneous polarization and/or magnetization in nonferroelastic domain walls: Symmetry predictions. *Ferroelectrics* **222**, 23–32 (1999).

[32] Feibig, M. Magnetoelectric correlations in multiferroic manganites revealed by nonlinear optics. *Adv. in Solid State Phys.* **46**, 255–267 (2008).

[33] Mostovoy, M. Ferroelectricity in spiral magnets. *Phys. Rev. Lett.* **96**, 067601 (2006).

[34] Tokunaga, Y. *et al.* Composite domain walls in a multiferroic perovskite ferrite. *Nature Materials* **8**, 558–562 (2009).

[35] Lajzerowicz, J. & Niez, J. J. Phase transition in a domain wall. *J. Physique Lett.* **40**, L165–L169 (1979).

[36] Aird, A. & Salje, E. K. H. Sheet superconductivity in twin walls: experimental evidence of WO_3. *J. Phys.: Condens. Matter* **10**, L377–L380 (1998).

[37] Choi, T. *et al.* Insulating interlocked ferroelectric and structural antiphase domain walls in multiferroic $YMnO_3$. *Nature Materials* **9**, 253–258 (2010).

[38] Roginska, Y. E., Tomashpolsky, Y. Y., Venevtsev, Y. N., Petrov, V. M. & Zhdanov, G. S. Nature of dielectric and magnetic properties of $BiFeO_3$. *Sov. Phys. - JETP* **23**, 47 (1966).

[39] Kiselev, S. V., Ozerov, R. P. & Zhdanov, G. S. Detection of magnetic order in ferroelectric $BiFeO_3$ by neutron diffraction. *Sov. Phys. Dokl.* **7**, 742 (1963).

[40] Béa, H. *et al.* Mechanisms of exchange bias with multiferroic $BiFeO_3$ epitaxial thin films. *Phys. Rev. Lett.* **100**, 017204 (2008).

[41] Martin, L. W. *et al.* Nanoscale control of exchange bias with $BiFeO_3$ thin films. *Nano Lett.* **8**, 2050–2055 (2008).

[42] Daraktchiev, M., Catalan, G. & Scott, J. F. Landau theory of domain wall magnetoelectricity. *Phys. Rev. B* **81**, 224118 (2010).

[43] Goltsev, A. V., Pisarev, R. V., Lottermoser, T. & Fiebig, M. Structure and interaction of antiferromagnetic domain walls in hexagonal $YMnO_3$. *Phys. Rev. Lett.* **90**, 177204 (2003).

[44] Gareeva, Z. V. & Zvezdin, A. K. Interacting antiferromagnetic and ferroelectric structures of multiferroics. *private communication* .

[45] Nolting, F. *et al.* Direct observation of the alignment of ferromagnetic spins by antiferromagnetic spins. *Nature* **405**, 767–769 (2000).

[46] Cruz, M. P. *et al.* Strain control of domain-wall stability in epitaxial $BiFeO_3$ (110) films. *Phys. Rev. Lett.* **99**, 217601 (2007).

[47] Meyer, B. & Vanderbilt, D. Ab initio study of ferroelectric domain walls in $PbTiO_3$. *Phys. Rev. B* **65**, 104111 (2002).

[48] Stemmer, S., Streiffer, S. K., Ernst, F. & Rühle, M. Atomistic structure of 90° domain walls in ferroelectric $PbTiO_3$ thin films. *Phil. Mag. A* **71**, 713–724 (1995).

[49] Floquet, N. & Valot, C. Ferroelectric domain walls in $BaTiO_3$: Structural walls model interpreting fingerprints in XRPD diagrams. *Ferroelectrics* **234**, 107–122 (1999).

[50] Jia, C.-L. *et al.* Atomic-scale study of electric dipoles near charged and uncharged domain walls in ferroelectric films. *Nature Materials* **7**, 57–61 (2008).

[51] Wu, X. & Vanderbilt, D. Theory of hypothetical ferroelectric superlattices incorporating head-to-head and tail-to-tail 180° domain walls. *Phys. Rev. B* **73**, 020103 (2006).

[52] Allen, L. J., McBride, W., O'Leary, N. L. & Oxley, M. P. Exit wave reconstruction at atomic resolution. *Ultramicroscopy* **100**, 91–104 (2004).

[53] Neaton, J. B., Ederer, C., Waghmare, U. V., Spaldin, N. A. & Rabe, K. M. First-principles study of spontaneous polarization in multiferroic $BiFeO_3$. *Phys. Rev. B* **71**, 014113 (2005).

[54] Li, J. F. *et al.* Dramatically enhanced polarization in (001), (101), and (111) $BiFeO_3$ thin films due to epitiaxial-induced transitions. *Appl. Phys. Lett.* **84**, 5261–5263 (2004).

[55] Ravindran, P., Vidya, R., Kjekshus, A., Fjellvåg, H. & Eriksson, O. Theoretical investigation of magnetoelectric behavior in $BiFeO_3$. *Phys. Rev. B* **74**, 224412 (2006).

[56] Lebeugle, D. *et al.* Electric-field-induced spin flop in $BiFeO_3$ single crystals at room temperature. *Phys. Rev. Lett.* **100**, 227602 (2008).

[57] Kubel, F. & Schmid, H. Structure of a ferroelectric and ferroelastic monodomain crystal of the perovskite $BiFeO_3$. *Acta Crystallogr. B* **46**, 698–702 (1990).

[58] Simmons, J. G. Transition from electrode-limited to bulk-limited conduction processes in metal-insulator-metal systems. *Phys. Rev.* **166**, 912–920 (1968).

[59] Scott, J. F. Magnetoelectric memories – a disruptive techology? *Chem. Phys, Chem.* **10**, 1761–1762 (2009).

[60] Kim, Y., Alexe, M. & Salje, E. K. H. Nanoscale properties of thin twin walls and surface layers in piezoelectric WO_{3-x}. *Appl. Phys. Lett.* **96**, 032904 (2010).

[61] Maksyovych, P. *et al.* Polarization control of electron tunneling into ferroelectric surfaces. *Science* **324**, 1421–1425 (2009).

[62] Chrosch, J. & Salje, E. K. H. Temperature dependence of the domain wall width in $LaAlO_3$. *J. Appl. Phys.* **85**, 722–727 (1999).

[63] Angoshtari, A. & Yavari, A. Effect of strain and oxygen vacancies on the structure of 180° ferroelectric domain walls in $PbTiO_3$. *Comput. Mater. Sci.* **48**, 258–266 (2010).

[64] Seidel, J. *et al.* Conduction at domain walls in oxide multiferroics. *Nature Materials* **8**, 229–234 (2009).

[65] Wu, J., Lou, X., Wang, Y. & Wang, J. Resistive hysteresis and diodelike behavior of $BiFeO_3$/ZnO heterostructures. *Electrochem. Solid-State Lett.* **13**, G9–G12 (2010).

[66] Yang, H. *et al.* Rectifying current-voltage characteristics of $BiFeO_3$/Nb-doped $SrTiO_3$ heterojuction. *Appl. Phys. Lett.* **92**, 102113 (2008).

[67] Zhang, J. *et al.* Surface, bulk, and interface electronic states of epitaxial $BiFeO_3$ films. *J. Vac. Sci. Technol. B* **27**, 2012–2014 (2009).

[68] Lubk, A., Gemming, S. & Spaldin, N. A. First-principles study of ferroelectric domain walls in multiferroic bismuth ferrite. *Phys. Rev. B* **80**, 104110 (2009).

[69] Yang, S.-Y. *et al.* Above-bandgap voltages from ferroelectric photovoltaic devices. *Nat. Nanotechnol.* **5**, 143–147 (2010).

[70] Pintilie, L. *et al.* Orientation-dependent potential barriers in case of epitaxial Pt-$BiFeO_3$-$SrRuO_3$ capacitors. *Appl. Phys. Lett.* **94**, 232902 (2009).

[71] Catalan, G. & Scott, J. F. Physics and applications of bismuth ferrite. *Adv. Mater.* **21**, 2463–2485 (2009).

[72] Borisevich, A. Y. *et al.* Mapping octahedral tilts and polarization across a domain wall in $BiFeO_3$ from z-contrast scanning transmission electron microscopy image atomic column shape analysis. *ACS Nano* **4**, 6071–6079 (2010).

[73] Borisevich, A. Y. *et al.* Suppression of octahedral tilts and associated changes in electronic properties at epitaxial oxide heterostructure interfaces. *Phys. Rev. Lett.* **105**, 087204 (2010).

[74] Wu, W. *et al.* Polarization-modulated rectification at ferroelectric surfaces. *Phys. Rev. Lett.* **104**, 217601 (2010).

[75] Singh, M. K., Katiyar, R. S. & Scott, J. F. New magnetic phase transitions in $BiFeO_3$. *J. Phys.: Condens. Matter* **20**, 252203 (2008).

[76] Clark, S. J. & Robertson, J. Energy levels of oxygen vacancies in $BiFeO_3$ by screened exchange. *Appl. Phys. Lett.* **94**, 022902 (2009).

[77] Mott, N. F. & Davis, E. A. *Electronic Processes in Non-crystalline Materials* (Oxford, 1979).

[78] Hasegawa, M., Yanagihara, J., Toyoda, Y., Kita, E. & Ranno, L. Electrical and magnetic properties of γ-Fe_2O_3 epitaxial films. *J. Magn. Magn. Mater.* **310**, 2283–2285 (2007).

[79] Papaioannou, J. C., Patermarakis, G. S. & Karayianni, H. S. Electron hopping mechanism in hematite (α-Fe_2O_3). *Journal of Physics and Chemistry of Solids* **66**, 839–844 (2005).

[80] Holcomb, M. B. *et al.* Probing the evolution of antiferromagnetism in multiferroics. *Phys. Rev. B* **81**, 134406 (2010).

[81] Zhou, J.-S. & Goodenough, J. B. Zener versus de gennes ferromagnetism in $La_{1-x}Sr_xMnO_3$. *Phys. Rev. B* **62**, 3834–3838 (2000).

[82] Goldschmidt, V. M. Crystal structure and chemical constitution. *Trans. Faraday Soc.* **25**, 253–283 (1929).

[83] Dagotto, E. *Nanoscale Phase Separation and Colossal Magnetoresistance* (Springer Verlag, New York, 2003).

[84] Park, S.-E. & Shrout, T. R. Ultrahigh strain and piezoelectric behavior in relaxor based ferroelectric single crystals. *J. Appl. Phys.* **82**, 1804–1811 (1997).

[85] Guo, R. *et al.* Origin of the high piezoelectric response in $PbZr_{1-x}Ti_xO_3$. *Phys. Rev. Lett.* **84**, 5423–5426 (2000).

[86] Fu, H. & Cohen, R. E. Polarization rotation mechanism for ultrahigh electromechanical response in single-crystal piezoelectrics. *Nature* **403**, 281–283 (2000).

[87] Ahart, M. *et al.* Origin of morphotropic phase boundaries in ferroelectrics. *Nature* **451**, 545–549 (2008).

[88] Ederer, C. & Spaldin, N. A. Effect of epitaxial strain on the spontaneous polarization of thin film ferroelectrics. *Phys. Rev. Lett.* **95**, 257601 (2005).

[89] Ricinschi, D., Yun, K.-Y. & Okuyama, M. A mechanism for the 150 μC cm^{-2} polarization of $BiFeO_3$ films based on first-principles calculations and new structural data. *J. Phys.: Condens. Matter* **18**, L97–L105 (2006).

[90] Béa, H. *et al.* Evidence for room-temperature multiferroicity in a compound with a giant axial ratio. *Phys. Rev. Lett.* **102**, 217603 (2009).

[91] Schlom, D. G. *et al.* Strain tuning of ferroelectric thin films. *Annu. Rev. Mater. Res* **37**, 589–626 (2007).

[92] G, X. *et al.* Low symmetry phase in (001) $BiFeO_3$ epitaxial constrained thin films. *Appl. Phys. Lett.* **86**, 182905 (2005).

[93] Chu, Y.-H. *et al.* Ferroelectric size effects in multiferroic $BiFeO_3$ thin films. *Appl. Phys. Lett.* **90**, 252906 (2007).

[94] Béa, H. *et al.* Investigation on the origin of the magnetic moment of $BiFeO_3$ thin films by advanced x-ray characterizations. *Phys. Rev. B* **74**, 020101 (2006).

[95] Yun, K. Y. *et al.* Structural and multiferroic properties of $BiFeO_3$ thin films at room temperature. *J. Appl. Phys.* **96**, 3399–3403 (2004).

[96] Kresse, G. & Furthmüller, J. Efficient iterative schemes for ab initio total-energy calculations using a plane-wave basis set. *Phys. Rev. B* **54**, 11169–11186 (1996).

[97] Anisimov, V. I., Aryasetiawan, F. & Lichtenstein, A. I. First-principles calculations of the electronic structure and spectra of strongly correlated systems: the LDA+U method. *J. Phys. Condens. Matter* **9**, 767–808 (1997).

[98] Christy, A. G. Isosymmetric structural phase transitions: Phenomenology and examples. *Acta Cryst. B* **51**, 753–757 (1995).

[99] Shpanchenko, R. V. *et al.* Synthesis, structure, and properties of new perovskite $PbVO_3$. *Chem. Mater.* **16**, 3267–3273 (2004).

[100] Belik, A. A. *et al.* Neutron powder diffraction study on the crystal and magnetic structures of $BiCoO_3$. *Chem. Mater.* **18**, 798–803 (2006).

[101] Chakhalian, J. *et al.* Orbital reconstruction and covalent bonding at an oxide interface. *Science* **318**, 1114–1117 (2007).

[102] Ohtomo, A. & Hwang, H. Y. A high-mobility electron gas at the $LaAlO_3/SrTiO_3$ heterointerface. *Nature* **427**, 423–426 (2004).

[103] Garcia-Barriocanal, J. *et al.* Colossal ionic conductivity at interfaces of epitaxial ZrO_2:$Y_2O_3/SrTiO_3$ heterostructures. *Science* **321**, 676–680 (2008).

[104] Choi, K. J. *et al.* Enhacement of ferroelectricity in strained $BaTiO_3$ thin films. *Science* **306**, 1005–1009 (2004).

[105] Scholl, A., Ohldag, H., Nolting, F., Stöhr, J. & Padmore, H. A. X-ray photoemission electron microscopy, a tool for the investigation of complex magnetic structures. *Rev. Sci. Instrum.* **73**, 1362–1366 (2002).

[106] Lebeugle, D. *et al.* Room-temperature coexistence of large electric polarization and magnetic order in $BiFeO_3$ single crystals. *Phys. Rev. B* **76**, 024116 (2007).

[107] de Groot, F. High-resolution x-ray emission and x-ray absorption spectroscopy. *Chem. Rev.* **101**, 1779–1808 (2001).

[108] Ohldag, H. *et al.* Correlation between exchange bias and pinned interfacial spins. *Phys. Rev. Lett.* **91**, 017203 (2003).

[109] Hatt, A. J., Spaldin, N. A. & Ederer, C. Strain-induced isosymmetric phase transition in $BiFeO_3$. *Phys. Rev. B* **81**, 054109 (2010).

[110] Lu, Y. X. *et al.* Epitaxial growth and magnetic properties of half-metallic Fe_3O_4 on GaAs(100). *Phys. Rev. B* **70**, 233304 (2004).

[111] Morrall, P. *et al.* Stoichiometry of $Fe_{3-\delta}O_4$(111) ultrathin films on Pt(111). *Phys. Rev. B* **67**, 214408 (2003).

[112] Moriya, T. Anisotropic superexchange interaction and weak ferromagnetism. *Phys. Rev.* **120**, 91–98 (1960).

[113] Phillips, T. G., Townsend, R. L. & White, R. L. Piezomagnetism of CoF_2 and α-Fe_2O_3 from electron-paramagnetic-resonance pressure experiments. *Phys. Rev. Lett.* **18**, 646–647 (1967).

[114] Borovik-Romanov, A. S. Piezomagnetism, linear magnetostriction and magnetooptic effect. *Ferroelectrics* **162**, 153–159 (1994).

[115] Chu, Y.-H. *et al.* Electric-field control of local ferromagnetism using a magnetoelectric multiferroic. *Nat. Mater.* **7**, 478–482 (2008).

[116] Zhang, J. X. *et al.* Large field-induced strains in a lead-free peizoelectric material. *Nat. Nanotechnol.* **6**, 98–102 (2011).

[117] Charles, B. A. *Modern Problems in Classical Electrodynamics* (Oxford University Press, 2004).

[118] Jackson, J. D. *Classical Electrodynamics* (John Wiley and Sons, 1999).

[119] Hofmann, A. *Synchrotron Radiation* (Cambridge, 2004).

[120] Schönhense, G. Imaging of magnetic structures by photoemission electron microscopy. *J. Phys.: Condens. Matter* **11**, 9517–9547 (1999).

[121] Anders, S. *et al.* Photoemission electron microscope for the study of magnetic materials. *Rev. Sci. Instrum.* **70**, 3973–3981 (1999).

[122] Carra, P. & Benoist, R. X-ray natural circular dichroism. *Phys. Rev. B* **62**, R7703–R7706 (2000).

[123] Goulon, J. *et al.* X-ray natural circular dichroism in a uniaxial gyrotropic single crystal of $LiIO_3$. *J. Chem. Phys.* **108**, 6394–6403 (1998).

[124] Alagna, L. *et al.* X-ray natural circular dichroism. *Phys. Rev. Lett.* **80**, 4799–4802 (1998).

[125] van der Laan, G. *et al.* Experimental proof of magnetic x-ray dichroism. *Phys. Rev. B* **34**, 6529–6531 (1986).

[126] Schütz, G. *et al.* Absorption of circularly polarized x rays in iron. *Phys. Rev. Lett.* **58**, 737–740 (1987).

[127] Brüche, E. Elektronenmikroskopische abbildung mit lichtelektrischen elektronen. *Z. Phys.* **86**, 448–450 (1933).

[128] van der Laan, G., Telling, N. D., Potenza, A., Dhesi, S. S. & Arenholz, E. Anisotropic x-ray magnetic linear dichroism and spectromicroscopy of interfacial co/nio(001). *Phys. Rev. B* **83**, 064409 (2011).

Appendix A

Soft X-ray Based Technique

A.1 Synchrotron Radiation

Synchrotron radiation is electromagnetic radiation generated by a synchrotron. However, the first observation of synchrotron radiation was in a cyclotron rather than in a real synchrotron source. A cyclotron is a type of particle accelerator, which accelerate charged particles using a high-frequency, alternating voltage with a perpendicular magnetic field to spiral the particles in a circle. While a cyclotron uses a constant magnetic field and a constant frequency applied electric field, both of these fields are varied in the synchrotron. In synchrotron, magnetic field is applied to turn the particles, so they circulate in a donut-shape pipe; while, electric field is used to accelerate the particles. By increasing both magnetic and electric fields appropriately as the particles gain energy, their path can be held constant as they are accelerated. The path of the particles usually contains both bend and straight sections. The bend sections are where the magnetic field is applied and where the radiation comes out; the straight sections are required at spacings around a ring, in which the undulators are usually built.

Generated by electrons traveling at a velocity closed to the speed of light and at energy of GeV order [1.0-1.9 GeV for Advanced Light Source (ALS)], synchrotron radiation is the brightest artificial source of X-rays. The angular distribution of the radiated energy can be derived from the expressions for the Liénard-Wiechert field as follows [117] [118] [119]

$$\mathbf{B}(\mathbf{r},t) = -\frac{\mu_0 q}{4\pi}\left[\frac{c\hat{\mathbf{n}}\times\vec{\beta}}{\gamma^2 R^2(1-\vec{\beta}\cdot\hat{\mathbf{n}})^3} + \frac{\hat{\mathbf{n}}\times[\dot{\vec{\beta}}+\hat{\mathbf{n}}\times(\vec{\beta}\times\dot{\vec{\beta}})]}{R(1-\vec{\beta}\cdot\hat{\mathbf{n}})^3}\right]_{\text{retarded}} \tag{A.1}$$

$$\mathbf{E}(\mathbf{r},t) = \frac{q}{4\pi\varepsilon_0}\left[\frac{\hat{\mathbf{n}}-\vec{\beta}}{\gamma^2 R^2(1-\vec{\beta}\cdot\hat{\mathbf{n}})^3} + \frac{\hat{\mathbf{n}}\times[(\hat{\mathbf{n}}-\vec{\beta})\times\dot{\vec{\beta}}]}{cR(1-\vec{\beta}\cdot\hat{\mathbf{n}})^3}\right]_{\text{retarded}} \tag{A.2}$$

where $\vec{\beta} = \vec{v}/c$ is the dimensionless velocity of the particles, $\dot{\vec{\beta}}$ is the corresponding acceleration, $\gamma = (1 - \beta^2)^{-frac12}$ is the Lorentz factor, and

$$\begin{aligned}\mathbf{R}(t') &= \mathbf{r} - \mathbf{r}_0(t') \\ R(t') &= |\mathbf{R}| \\ \hat{\mathbf{n}} &= \frac{\mathbf{R}}{R}\end{aligned}$$

which is the unit vector between the observation point and the position of the charge at the retarded time, t'.

If we ignore the near field (first term in the expressions of both $\mathbf{E}$ and $\mathbf{B}$), the radial component of Poynting's Vector can be calculated to be

$$[\mathbf{S} \cdot \hat{\mathbf{n}}]_{\text{retarded}} = \frac{q^2}{16\pi^2\varepsilon_0 c} \left\{ \frac{1}{R^2} \left| \frac{\hat{\mathbf{n}} \times [(\hat{\mathbf{n}} - \vec{\beta}) \times \dot{\vec{\beta}}]}{(1 - \vec{\beta} \cdot \hat{\mathbf{n}})^3} \right|^2 \right\}_{\text{retarded}} \tag{A.3}$$

Then, the energy radiated into per solid angle in the charge's own frame is

$$\begin{aligned}\frac{\mathrm{d}\mathcal{P}}{\mathrm{d}\Omega} =& R(t')^2 \left[\mathbf{S}(t') \cdot \hat{\mathbf{n}}(t')\right] \frac{\mathrm{d}t}{\mathrm{d}t'} \\ =& R(t')^2 \mathbf{S}(t') \cdot \hat{\mathbf{n}}(t') \left[1 - \vec{\beta}(t') \cdot \hat{\mathbf{n}}(t')\right] \\ =& \frac{q^2}{16\pi^2\varepsilon_0 c} \frac{\left|\hat{\mathbf{n}}(t') \times \left\{\left[\hat{\mathbf{n}}(t') - \vec{\beta}(t')\right] \times \overset{\rightarrow\,\cdot}{}(t\beta)\right\}\right|^2}{\left[1 - \vec{\beta}(t') \cdot \hat{\mathbf{n}}(t')\right]^5}\end{aligned} \tag{A.4}$$

When the charge is in instantaneous circular motion with its acceleration $\dot{\overrightarrow{\beta}}$ perpendicular to its velocity $\overrightarrow{\beta}$. Choosing a coordinate system such that instantaneously $\overrightarrow{\beta}$ is in the z direction and $\dot{\overrightarrow{\beta}}$ is in the x direction. With the customary polar angles θ, ϕ defining the direction of observation, the formula above reduces to

$$\frac{\mathrm{d}\mathcal{P}}{\mathrm{d}\Omega} = \frac{q^2}{4\pi c^3} \frac{|\dot{\mathbf{v}}|^2}{(1 - \beta\cos\theta)^3} \left[1 - \frac{\sin^2\theta\cos^2\phi}{\gamma^2 (1 - \beta\cos\theta)^2}\right] \tag{A.5}$$

In the relativistic limit, $\gamma \gg 1$, the angular distribution can be written approximately

$$\frac{\mathrm{d}\mathcal{P}}{\mathrm{d}\Omega} \simeq \frac{2}{\pi} \frac{e^2}{c^3} \gamma \frac{|\dot{\mathbf{v}}|^2}{(1 + \gamma^2\theta^2)^3} \left[1 - frac4\gamma^2\theta^2\cos^2\phi\left(1 + \gamma^2\theta^2\right)^2\right] \tag{A.6}$$

The factor $(1 - \beta\cos\theta)$ in the denominator tips the angular distribution forward into a narrow cone. The figure of the angular distribution has a sharp peak around $\theta = 0$.

A.2 Polarized X-rays

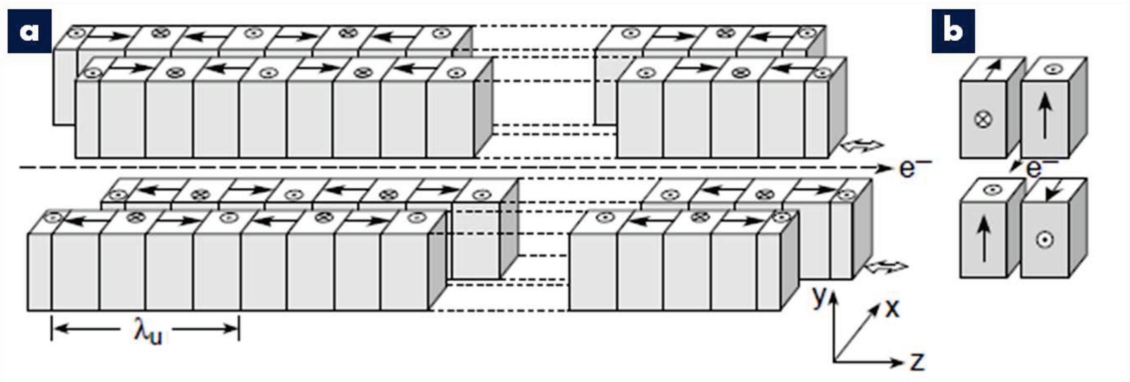

Figure A.1: Schematics of elliptically polarizing undulators. [10]

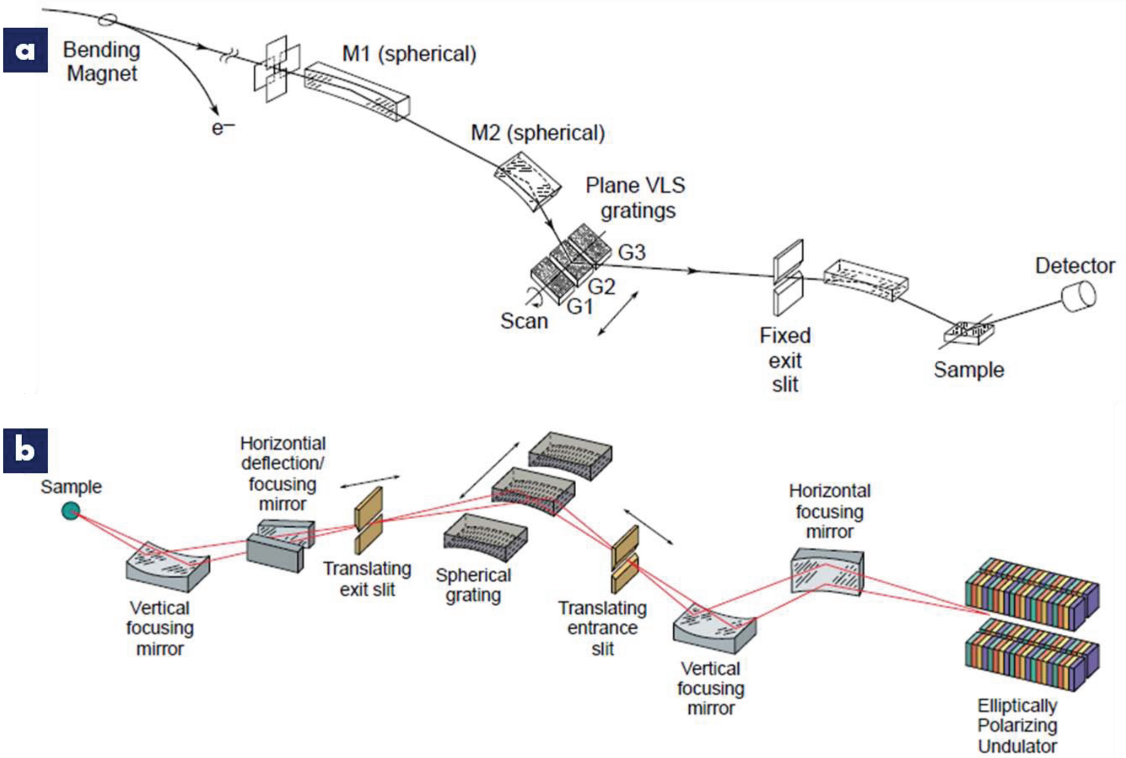

Figure A.2: Schematics of beamline setup of a bending magnet beamline (a) and an EPU beamline (b). [10]

In synchrotron facilities, both bending magnets and undulators can generate synchrotron radiation. However, undulators can provide several orders of magnitude higher flux than a simple bending magnet. Moreover, elliptically polarizing undulators can also provide much purer polarizations. With bending magnet, the planar acceleration geometry appears to make the radiation linearly polarized when observed in the orbital plane, and circularly polarized when observed at a small angle to that plane. An undulator consists of a periodic structure of dipole magnets (Figure A.1), where the static magnetic field is alternating along the length of the undulator with a wavelength λ_u. Electrons are forced to oscillate while traversing this periodic magnet structure, thus radiate energy with the intensity proportional to N^2, where N is the number of periods in the undulator. An EPU contains four sets of dipole magnets. By modulating the phase difference between each pair of the magnets, EPU can produce left and right circularly polarized, as well as linearly polarized X-rays. For EPU with three movable sets of dipole magnets, by careful tuning of the phase delay, EPU can also freely rotate the polarization of linearly polarized X-ray with fine steps. This freedom of linear polarization rotation capability makes it possible to adjust the light polarization freely without changing the sample geometry of the measurements, which is a great advantage of using EPU comparing to a bending magnet. Beamline setup for both bending magnet and EPU beamlines are schmatically illustrated in Figure A.2. [10]

A.3 X-ray Absorption Process

In this section, we describe the X-ray absorption process by deriving the X-ray absorption cross section. The X-ray absorption cross section σ_x of an atom or molecule is defined as the number of electrons excited per unit time divided by the number of incident photons per unit time per unit area. This cross section can be calculated from Fermi's "Golden Rule" for the transition probability per unit time P_{ij} from the initial state $|i\rangle$ to the final state $|f\rangle$ driven by a harmonic time-dependent perturbation $V(t) = \overline{V}e^{-\mathrm{i}\omega t}$ [13]

$$P_{ij} = \frac{2\pi}{\hbar}|\langle f|\overline{V}|i\rangle|^2 \varrho_f(E) \tag{A.7}$$

where $\varrho_f(E)$ is the energy density of final states. In the case of a L-shell excitation P_{ij} is the number of electrons excited per unit time from the $2p$ shell to a final state $|f\rangle$.

By only considering the cross section contribution from the inner shells, we use the inner shell excitation produced by an electromagnetic wave with electric field vector $\boldsymbol{E}$ and vector potential $\boldsymbol{A}$. In the Coulomb gauge, the relation between these two quantities is

$$\boldsymbol{E} = -\frac{1}{c}\frac{\partial \boldsymbol{A}}{\partial t} \tag{A.8}$$

The vector potential can be written in the form of a plane electromagnetic wave of wave vector $\boldsymbol{k}$, frequency ω, and unit vector $\boldsymbol{e}$,

$$\boldsymbol{A} = \boldsymbol{e} A_0 \cos(\boldsymbol{k} \cdot \boldsymbol{x} - \omega t) = \boldsymbol{e} \frac{A_0}{2} \left(\mathrm{e}^{\mathrm{i}(\boldsymbol{k} \cdot \boldsymbol{x} - \omega t)} + \mathrm{e}^{-\mathrm{i}(\boldsymbol{k} \cdot \boldsymbol{x} - \omega t)} \right) \tag{A.9}$$

Then, the photon flux F_{ph} associated with this plane wave, i.e., the number of photons per unit time per unit area, can be calculated from the two equations above

$$F_{\mathrm{ph}} = \frac{A_0^2 \omega}{8\pi\hbar c} = \frac{E_0^2 c}{8\pi\hbar\omega} \tag{A.10}$$

Since the X-ray absorption cross section is defined as

$$\sigma_x = \frac{P_{if}}{F_{\mathrm{ph}}} \tag{A.11}$$

the term P_{if} also needs to be evaluated. The dominant perturbative terms describing the interaction of spinless particles of charge $-e$ and mass m with an electromagnetic field is given by

$$V(t) = \frac{e}{mc} \boldsymbol{A} \cdot \boldsymbol{p} \tag{A.12}$$

where $\boldsymbol{p}$ is the sum of the linear momentum operators of the electrons. Then, the transition probability per unit time is

$$P_{if} \frac{\pi e^2}{2\hbar m^2 c^2} A_0^2 |\langle f | \mathrm{e}^{\mathrm{i}\boldsymbol{k} \cdot \boldsymbol{x}} \boldsymbol{e} \cdot \boldsymbol{p} | i \rangle|^2 \varrho_f(E) \tag{A.13}$$

By assuming $\boldsymbol{k} \cdot \boldsymbol{x} \ll 1$ or $|\boldsymbol{x}| \ll \lambda/2\pi$, where λ is the X-ray wavelength, equation (A.13) can be simplified by retaining only the first term in the expansion of the exponential (dipole approximation). For excitation of the iron L-shell at $\hbar\omega = 710$ eV the wave length is $\lambda/2\pi = 2.8$ Å and —$\boldsymbol{x}$—, characterizing the L-shell diameter, can be estimated from the Bohr radius $a_0 = 0.53$ Å and the atomic number Z as $|\boldsymbol{x}| \simeq 2a_0/Z = 0.04$ Å, so that the dipole approximation is well satisfied. Therefore, the X-ray absorption cross section can be written as [13]

$$\sigma_x = \frac{4\pi^2\hbar^2}{m^2} \frac{e^2}{\hbar c} \frac{1}{\hbar\omega} |\langle f | \boldsymbol{e} \cdot \boldsymbol{p} | i \rangle|^2 \varrho_f(E) \tag{A.14}$$

Since the X-ray absorption process highly depends on the initial and final states of the excited electrons, as well as the energy density of the final states, this process occurs at different energies for different elements. The element specificity of X-ray absorption spectra can be seen in Figure A.2, where a wedge Cu/Fe/Ni sample was probed under X-rays with energy from 650 eV to 1000 eV. As shown in this figure, the X-ray absorption spectra at various points along the wedge are plotted. As the iron layer becomes thicker, the intensity at the iron absorption edge increases since there is more iron to probe; while the intensity at the nickel absorption edge decreases

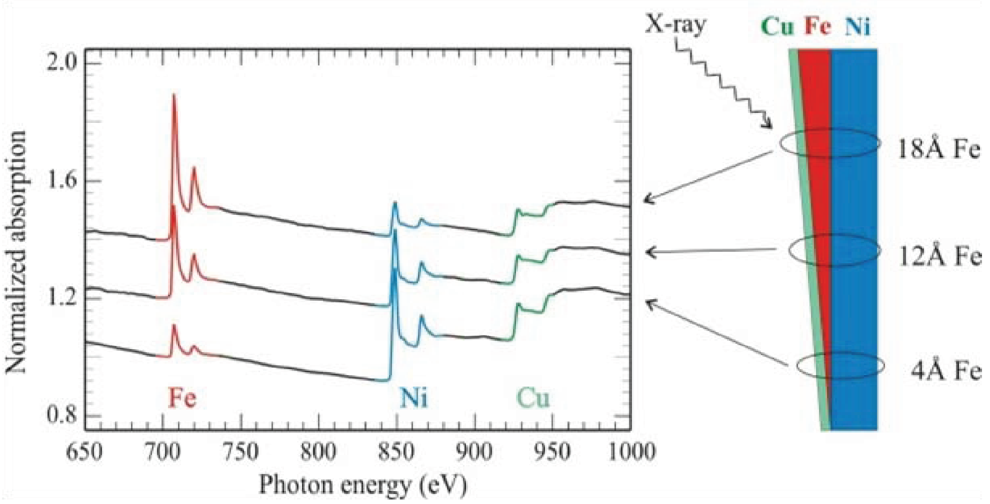

Figure A.3: X-ray absorption spectra of a wedge Cu/Fe/Ni sample, revealing the composition at various points along the wedge. [11]

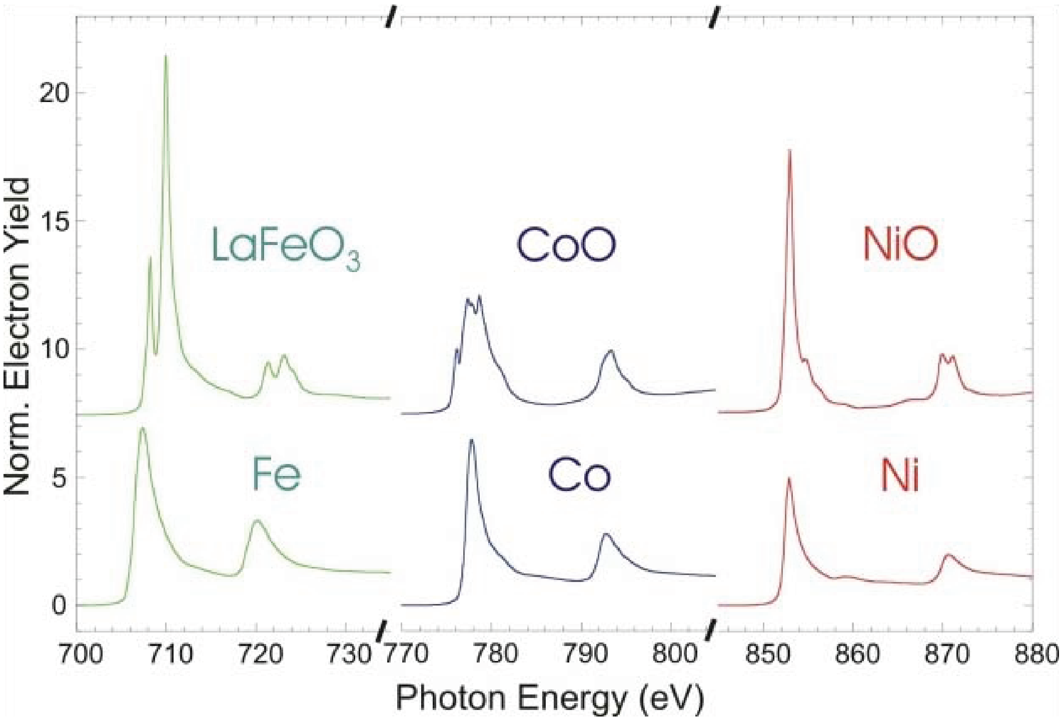

Figure A.4: *L*-edge X-ray absorption spectra of Fe, Co and Ni in the form of elemental metals an oxides. [11]

because the limited electron escape depth of the total electron yield (TEY) technique. The copper layer, at the very top of this wedge sample, provides a constant signal, reflecting its constant thickness. Furthermore, the X-ray absorption line shape also provides information that can be used to determine the chemical environment of the element species. [11] [120] Figure A.3 is an example of the *L*-edge X-ray absorption spectra of Fe, Co, and Ni in the form of elemental metals and their oxides. Instead of having single peak at both L_3 (lower energy) and L_2 (higher energy) absorption edges, the oxides always show multiplet structure at the principle peaks. The emergence of these multiplets is because the empty oxide states are more localized than metal states and their energies are determined by crystal field and multiplet effects. [121] It is worth to mention that since X-ray absorption spectra are governed by dipole selection rules the *d*-shell properties are best probed by *L*-edge absorption studies ($2p$ to $3d$ transitions), which are widely used in the magnetism study in $BiFeO_3$ and other transition metal oxides.

A.4 Magnetic Analysis

Over the years, polarized X-rays has been found to offer sensitivity to many types of order in materials. Dichroism, by one definition describing the effect that light rays having different polarizations are absorbed by different amounts, is one of the most used analysis in polarized X-ray absorption study to investigate structural, electronic and magnetic properties of the materials. Dichroism can arise from a wide range of effects including natural circular dichroism [122] from non-central symmetric crystals [123] [124], linear dichroism from antiferromagnetic [125] and ferroelectric [80] order, and magnetic circular dichroism from ferromagnetic order [126]. In this section I will discuss the principles of X-ray magnetic circular and linear dichroism (XMCD and XMLD) analyses, which are generously applied in the work of this dissertation.

A.4.1 X-ray Magnetic Circular Dichroism

The concepts of XMCD, first established by Schütz, *et al.* [126], are illustrated in Figure A.4, which shows its sensitivity to spin and other angular momentum with circularly polarized X-rays. In these schematics, electrons are excited from spin-orbital split $2p$ levels [$p_{3/2}$ (L_3) and $p_{1/2}$ (L_2)] to $3d$ empty states. The total intensity of the L_3 and L_2 resonances can be directly linked to the number of empty *d* states (N) with the first X-ray absorption sum rule, as shown in Figure A.4a. For a magnetic material, such as Fe, Co, and Ni, the *d* shell has a non-zero spin moment, which is given by the imbalance of spin-up (green *d* band in Figure A.4b) and spin-down (blue *d* band in Figure A.4b) electrons, or equivalently imbalance of spin-up and spin-down holes. In order to probe the difference in the number of *d* holes with up and down spin, we use left and right circularly polarized photons which transfer

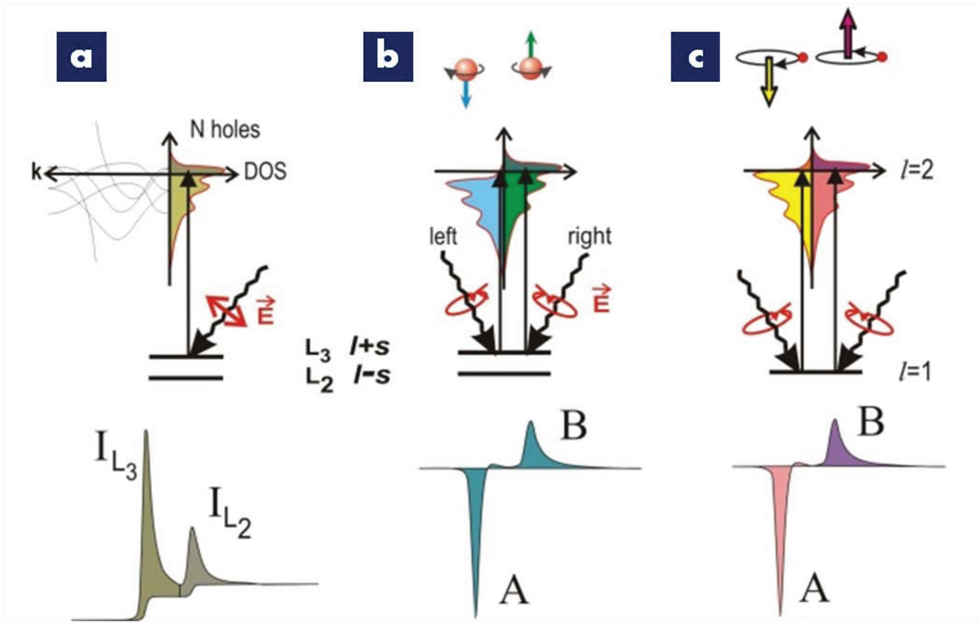

Figure A.5: Schematics of electronic transitions in L-edge X-ray absorption and circular dichroism. (a) Schematic of electronic transitions in conventional L-edge X-ray absorption, in which the total transition intensity of the two peaks is proportional to the number of d holes. (b),(c) X-ray magnetic circular X-ray dichroism giving the information of spin moment and orbital moment, respectively. [11]

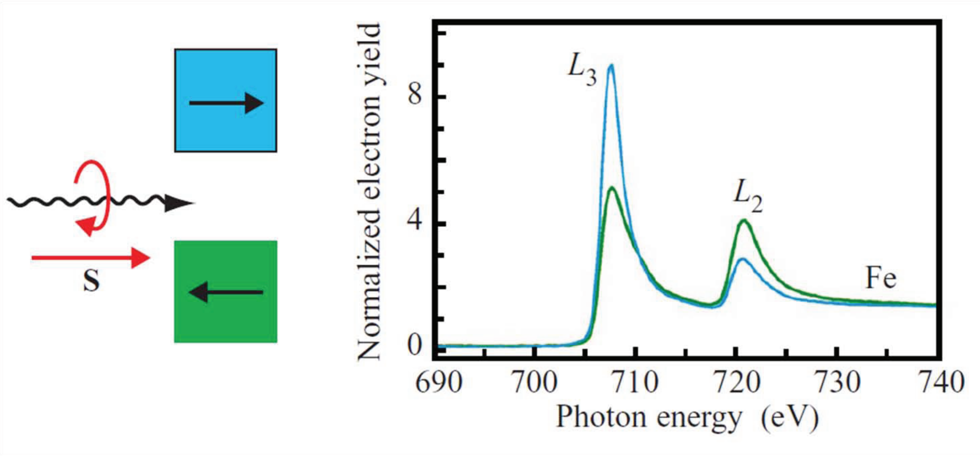

Figure A.6: X-ray absorption spectra when the incident photon spin parallel (in blue) and anti-parallel (in green) to the magnetization direction of the material. [12]

their angular momentum to the excited photoelectrons, so that the X-ray absorption process becomes spin dependent.

The excited photoelectron carries the transferred angular momentum as a spin or other angular momentum, or both. Thus, by applying other sum rules, the spin moment (Figure A.4b) and orbital moment (Figure A.4c) can be determined with XMCD analysis. Right circular photons and left circular photons transfer opposite momentum to the photoelectrons. For example, since $p_{3/2}$ (L_3) and $p_{1/2}$ (L_2) levels have opposite spin-orbital coupling, the spin polarization will be opposite at these two levels. Hence, the X-ray absorption intensity at L_3 edge with right circular photons is higher than with left circular photons; while the X-ray absorption intensity at L_2 edge with right circular photons is lower than with left circular photons (Figure A.4b).

Since spin flip is forbidden in electric dipole transitions (dominant transition in the X-ray absorption process), excited photoelectrons have conserved spins when excited from p core shell into d hole states in the case of L-edge X-ray absorption process. Then, the spin states of the final d hole states and the initial p core states have to be the same. Hence, the spin-split valence shell, i.e.,[$p_{3/2}$ and [$p_{3/2}$ states, acts as a detector for the spin of the excited photoelectron and the transition intensity is proportional to the number of empty d states of a given spin. The magnitude of dichroism has a $\cos\theta$ dependence, where θ is the angle between the photon spin and the magnetization direction of the material. Thus, the maximum dichroism effect can be observed if the photon spin direction and parallel and anti-parallel to the magnetization directions of the material (Figure A.5) [12]. For the photon spin perpendicular to the magnetization directions, the X-ray absorption spectrum lies in the middle of the green and blue curves in Figure A.5.

A.4.2 X-ray Magnetic Linear Dichroism

X-ray linear dichroism, pioneered by van der Laan *et al.* in 1986 [125], only senses the charge order in systems where the absorbing atom has lower than cubic symmetry, which directly leads to its sensitivity to ferroelectric order. However, in the presence of spin order, the spin-orbit coupling lead to preferential charge order relative to the spin direction even in cubic systems, which provides XMLD the capability to determine the spin axis in ferromagnetic and especially antiferromagnetic, to which XMCD has no sensitivity, order. Since the electric field vector ($\boldsymbol{E}$) oscillates along an axis in linearly polarized X-rays, XMLD is only sensitive to axial not direction properties, i.e. antiferromagnetic easy axis. In the following, I will mainly introduce the concept of XMLD probing an antiferromagnetic system, which is widely used to observe the antiferromagnetic domain structures in $BiFeO_3$ and other materials.

The maximum XMLD effect can be obtained for $\boldsymbol{E}$ parallel versus $\boldsymbol{E}$ perpendicular to the magnetic axis, as shown in Figure A.6. In contrast to the XMCD effect, which has a $\cos\theta$ dependence, the XMLD effect has a $\cos^2\theta$ dependence, where θ is the angle between the electric field vector and the magnetic axis. [12] Since X-ray linear dichroism can arise from both electric and magnetic asymmetries, it is

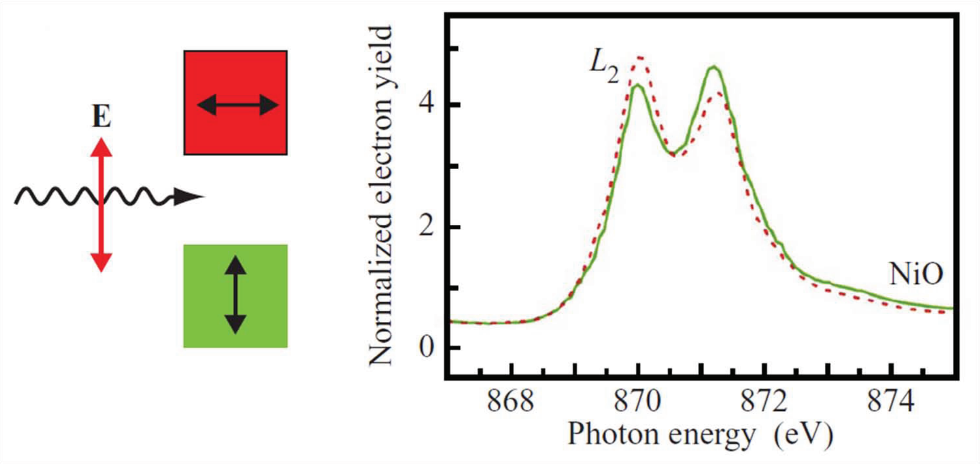

Figure A.7: X-ray absorption spectra when the incident photon spin parallel (in green) and perpendicular (in red) to the magnetic axis of the material. [12]

important to carefully distinguish magnetic order contribution from ligand field effect, which is typically done through temperature dependent measurements, i.e. XMLD measurements above and below Néel temperature.

A.5 Principles and Techniques of NEXAFS

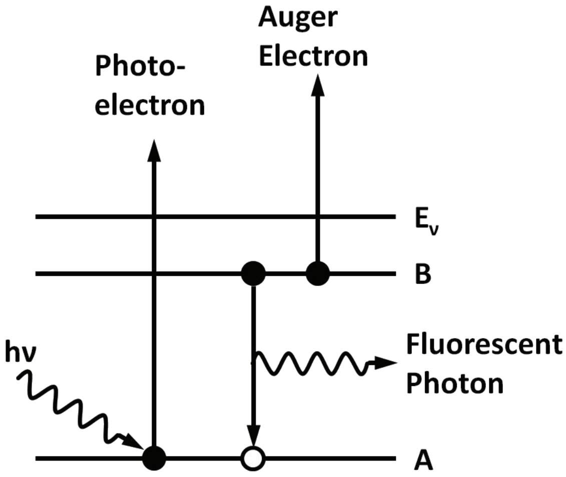

Figure A.8: Schematic a photon absorption process resulting in a photoelectron and a core hole. Then, the deexcitation process follows this absorption process with the generation of either Auger electron or Fluorescent photon. [13]

Instead of directly measuring the absorbed X-ray intensity by gathering the transmitted X-rays, X-ray absorption process is usually detected by observing the secondary deexcitation process. Figure A.7 illustrates the X-ray absorption process followed with the secondary deexcitation process. When a core electron is excited by the photon, a photoelectron and a core hole are generated. Then, the deexcitation process occurs during the decay of the core hole either radiatively, by emission of a fluorescent photon, or nonradiatively, by Auger electron emission. [13] Fluorescent photons can be collected to provide the X-ray absorption spectrum, and this detection mode is named fluorescent yield (FY) mode.

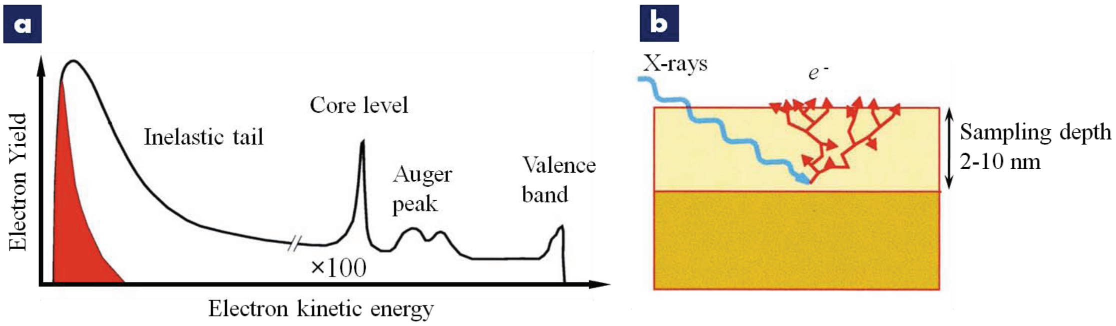

Figure A.9: Electrons with different energies excited off of the sample surface following the X-ray absorption process. (a) The distribution of electron numbers as a function of its kinetic energy, where the secondary electrons can be seen as the largest portion. (b) Schematic of generation of secondary electrons with a sampling depth of 2-10 nm. [11]

Following the primary Auger electron emission, the generated photoelectron and Auger electron can directly be excited over the vacuum level or go through an elastic or inelastic scattering process. The Auger electrons that directly excited off of the sample surface can be detected in the Auger electron yield (AEY) mode, which gives a small portion of all the electrons going out of the sample followed the X-ray absorption process and only probing 1-2 nm from the sample surface. The elastically scattered electrons can be detected in partial electron yield (PEY) mode, which set a lower energy threshold for the electrons to be detected. For the electrons going through the inelastic process, a large number of secondary electrons are created for each photoelectron or Auger electron, which is the largest portion of the electrons go out of the sample surface and illustrated in Figure A.8a in the inelastic tail. The process of generating secondary electrons is illustrated in Figure A.8a, which gives a probing depth of 2-10 nm (five times greater than that of AEY detection). Collecting electrons of all energies from the sample is the simplest detection technique, which is referred to as total electron yield (TEY) and the secondary electrons contribute its largest portion.

A.6 Instrumentation of NEXAFS

In this section, I will introduce two instruments in the study of X-ray absorption spectroscopy: photoemission electron microscopy (PEEM) providing the capability to study materials locally with great spatial resolution and X-ray absorption spectrometry giving an averaged signal from a whole sample with the capability of applying magnetic field during the measurements.

A.6.1 Photoemission Electron Microscopy

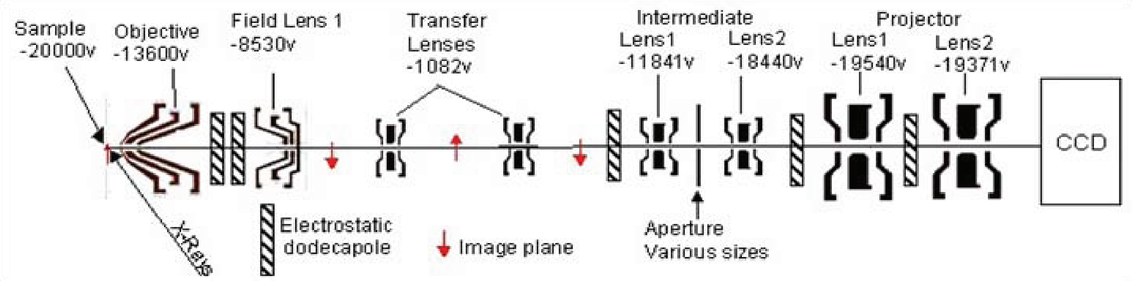

Figure A.10: Electron optics of PEEM3 at beamline 11.0.1 in ALS.

Photoemission electron microscopy is an imaging technique that collects electrons emitted from a sample in response to the absorption of ionizing radiation. These emitted electrons, as discussed in previous section, are mainly secondary electrons generated from the inelastic scattering process of photoelectrons and Auger electrons. The secondary electrons, with low kinetic energy (<20 eV) after escaping from the sample surface, are accelerated by a strong electric field between the sample and the outer electrode of the objective lens, as shown in Figure A.9. As they going through a series magnetic or electrostatic electron lens system, the image is magnified thousand times and recorded by an electron-sensitive detector [11].

Although about 80 years ago the first working PEEM has been built by Bruche, *et al.*, [127], who used ultraviolet light to image photoelectrons emitted from a metal, PEEM has become a practical tool only in recent years due to current technology developments [120]. Today, a spatial resolution of several 10 nm with X-rays can be usually achieved by the PEEM without a aberration correction system attached. However, with the aberration correction system installed, the spatial resolution of PEEM can be brought down to a few nanometers close to the physical limit of the emission microscope (the mean free path of low energy electrons).

The PEEM work presented in this dissertation was completed at two different beamlines. PEEM3 at beamline 11.0.1 in Advanced Light Source (ALS) has X-ray polarization rotation capability from the EPU and a great spatial resolution of

∼20 nm. Part of the study in chapter 3 has been done with the PEEM setup at beamline X11MA in the Swiss Light Source (SLS), which allows both sample and light polarization rotation. Although the spatial resolution of this PEEM setup in SLS (∼150 nm) is not as great as PEEM3, it gives very stable spectra for local spectroscopy measurements.

A.6.2 X-ray Absorption Spectrometry

Although X-ray absorption spectrometry doesn't have any spatial resolution in XAS measurements, it has its own advantages compare to PEEM. PEEM can only run in TEY mode, and because of the requirement of spatial resolution apertures are used to block the electrons with higher kinetic energy, which only allow the low energy electrons (red shaded area in Figure A.8a) to go through the imaging system. However, X-ray absorption spectrometry usually has the capability to record the XAS in different ways, including TEY, FY, and observing transmitted X-rays, which provide the XAS information of the samples with different sampling depth. One of the greatest advantage of studying XAS with X-ray absorption spectrometry is that magnetic field can be applied during the measurements, which is strictly forbidden during PEEM imaging. The application of magnetic field enables researchers to distinguish rotatable spins to pinned spins and gives the opportunity to investigate different types of coupling between different phases in the sample [128].

Appendix B

List of Symbols and Abbreviations

α - First order magnetoelectric coupling coefficient
β - Higher order magnetoelectric coupling coefficient
γ - Higher order magnetoelectric coupling coefficient or interfacial energy
ε - Electric susceptibility
μ - Magnetic susceptibility
μ_0 - Vacuum permeability
μ_B - Bohr magnetron, equal to 9.274096×10^{-24} J/T
χ_e - Electric susceptibility
χ_m - Magnetic susceptibility
(lmn) - Miller indices for specific crystallographic plane
$[lmn]$ - Miller indices for specific crystallographic direction
$\{lmn\}$ - Miller indices for a family of equivalent crystallographic planes
$< lmn >$ - Miller indices for a family of equivalent crystallographic directions
AC - Alternating current
AEY - Auger electron yield
AFM - Atomic force microscopy
ALS - Advanced Light Source
BFO - $BiFeO_3$
C - Subscript, pseudo-cubic indices
c-AFM - Conductive atomic force microscopy
CMR - Colossal magnetoresistance
CoFe - $Co_{0.9}Fe_{0.1}$
D - Down
DC - Direct current
DSO - $DyScO_3$
E - Electric field
e^- - Electron
EB - Exchange bias
EELS - Electron energy loss spectroscopy

EPU - Elliptically polarizing undulator
EXAFS - Extended X-ray absorption fine structure
F - Free energy of a system
Fe - Iron
FE - Ferroelectric
FM - Ferromagnetic, Ferromagnet
H - Magnetic field
HAADF-STEM - High-angle annular dark-field scanning transmission electron microscopy
H_C - Coercive field
H_{EB} - Exchange bias field
HRTEM - High resolution transmission electron microscopy
IP - In-plane
LAO - $LaAlO_3$
LBFO - La-doped $BiFeO_3$
LCP - Left circular polarization or left circularly polarized
LNO - $LaNiO_3$
LSAT - $(LaAlO_3)_{0.3}(SrAl_{0.5}Ta_{0.5}O_3)_{0.7}$
LSCO - $La_{0.5}Sr_{0.5}CoO_3$
LSMO - $La_{0.7}Sr_{0.3}MnO_3$
LSDA - Local spin density approximation
LSDA+U - Local spin density approximation plus a Hubbard U parameter
M - Magnetization
MBE - Molecular-beam epitaxy
ME - Magnetoelectric
MR - Magnetoresistance
NEXAFS - Near-edge X-ray absorption fine structure
O - Subscript, orthorhombic indices
OOP - Out-of-plane
P - Electric polarization
PEEM - Photoemission electron microscopy
PFM - Piezoresponse force microscopy
PLD - Pulsed laser deposition
PMN-PT - $Pb(Mg_{0.33}Nb_{0.67})O_3$-$PbTiO_3$
PZT - $Pb(Zr_xTi_{1-x}O_3)$
PZN-PT - $Pb(Zn_{0.33}Nb_{0.67})O_3$-$PbTiO_3$
R - Rhombohedral
RCP - Right circular polarization or right circularly polarized
RSM - Reciprocal space map
SHG - Second harmonic generation
SMOKE - Surface magneto-optical Kerr effect
SRO - $SrRuO_3$

STEM - Scanning transmission electron microscopy
STM - Scanning tunneling microscopy
STO - $SrTiO_3$
STS - Scanning tunneling spectroscopy
T - Tetragonal
T_C - Ferroelectric or ferromagnetic Curie temperature
TDGL - Time dependent Ginzburg-Landau
TEM - Transmission electron microscopy
TEY - Total electron yield
T_N - Néel temperature of an antiferromagent
U - Up
UHV - Ultra-high vacuum
VRH - Variable range hoping
XANES - X-ray absorption near-edge spectroscopy
XAS - X-ray absorption spectroscopy
XLD - X-ray linear dichroism
XMCD - X-ray magnetic circular dichroism
XMLD - X-ray magnetic linear dichroism
XRD - X-ray diffraction
YAO - $YAlO_3$